ADDITIVE MANUFACTURING OF NOVEL CEMENTED CARBIDES WITH SELF LUBRICATING PROPERTIES

AGYAPONG JOSEPH

A THESIS SUBMITTED TO
THE FACULTY OF GRADUATE STUDIES IN PARTIAL FULFILLMENT
OF THE REQUIREMENTS FOR THE DEGREE OF
MASTER OF APPLIED SCIENCE

GRADUATE PROGRAM IN MECHANICAL ENGINEERING
YORK UNIVERSITY
TORONTO, ONTARIO

December 2019

ABSTRACT

Metal-Additive Manufacturing presents many challenges for different materials even though it is known to shorten processing time. During metal-additive manufacturing processing, various complex mechanisms occur during the processing and thus affect the microstructural integrity of the material being processed. Powder composition, processing parameters and post-processing treatments dictate the microstructural integrity and mechanical properties of the processed parts. Materials such as cemented carbides (WC-Co) which is very common and suitable for products in aerospace, nuclear, manufacturing, mining and military need to be carefully studied to successfully transition from its conventional powder metallurgy processing to this novel manufacturing technique. In this research, WC-17Co and WC-Co-hBN cemented carbides were processed using Selective Laser Sintering (SLS) and heat treated at 400 °C, 600 °C, 800 °C and 1000 °C for 3 hours to understand the effect of processing and post-processing heat treatment on the structure and properties of the cemented carbide. Electron microscopy and X-ray diffraction (XRD) analysis revealed that the microstructure of the as-printed WC-17Co specimen was characterized by relatively large poly-angular WC/W_2C chips, WC-Co dendritic structures, W-C-Co phase and Co-rich regions. WC-Co-hBN also revealed from the microstructure polyangular WC chips which were smaller in size with no W_2C phases present in the sample. During heat treatment between 0 °C to 600 °C, the large poly-angular chips in both WC-17Co and WC-Co-hBN disintegrated to smaller poly-angular chips as a result of the conversion of the unstable W_2C phase to the more stable WC phase and the generation of W-Co-N and Co-W-B phases respectively. Heat treatment above 600 °C resulted in the coalescence and growth of relatively large WC phase chips. There was significant increase in hardness of the WC-17Co samples during heat treatment when compared with the as-printed WC-17Co sample, with the sample heat-treated at 600 °C being 36% harder than the as-printed sample due to the breakdown of poly-angular WC chips and the increase in volume fraction and spatial distribution of the observed W-C-Co phase regions. The increase in hardness at 600 °C was coupled with the highest fracture toughness, representing a 34% increase in fracture toughness, when compared with the as-printed sample. The high fracture toughness is attributed to the evolution of the ductile W_6Co_6C phase in the sample after heat treatment. Nevertheless, the as-printed sample had approximately 15% higher wear resistance than the

sample heat-treated at 600 °C. In the WC-Co-hBN, the heat-treated samples had lower hardness values compared to the as-printed WC-Co-hBN sample. However, the hardness values were 3 times higher than the hardness value of the WC-17Co sample. This was attributed to the lower grain sizes in the WC-Co-hBN as compared to the WC-17Co samples. The wear resistance of the WC-Co-hBN samples were much higher than the WC-17Co samples with the highest being on the WC-Co-hBN sample heat treated at 1000 °C. It is concluded that post-processing heat treatment of SLS printed WC-17Co alloy at 600 °C can be used to improve the structure and mechanical properties of the alloy. And a further improvement of the wear properties and hardness of the material can be done by adding a volume of hBN to the alloy.

DEDICATION

I dedicate this

masters' thesis to the

All-Wise Knowing God

And

To my wonderful sister

Deborah Adjoa Agyapong

ACKNOWLEDGEMENTS

I would like to thank all those who helped, supported and guided me throughout this work. My first appreciation goes to the all-wise God, who in His wisdom, granted me knowledge and understanding. I would not have made it without Him.

I am secondly grateful to my family back home for the immense support, love and prayers they offered on my behalf. Their advice and encouragement gave me inspiration to press on when anytime I felt depressed.

I am also grateful to the family I made here in Canada, which includes the Yiadom-Boakye family, Almey Tse Soriano and my fellow lab members at the Microstructural Tailoring of Advanced Materials Lab (MTAM-Lab). They made my stay in Canada an enjoyable one. I would have felt lonely at this part of the world if it was not their constant check-up and inclusivity.

I also thank my supervisors Professor Solomon Boakye-Yiadom, whom I took as a brother and Professor Alex Czekanski, whom I took as a father, for their persistent support and advice throughout my degree. Their wise counsel and motivation drove me to successfully finish ahead of time. I am glad I had both great professors as my mentors. I hope to grow up and become like them one day.

I am very grateful also for the unparallel expertise of the various lab technicians which includes David Marcinkiewicz and Jim Freemantle, who helped me to conduct safe, standard and successful experiments during my research. Other technicians from other universities who helped me use their machines and analyse my data cannot be left out. I thank you all.

My gratitude also goes to all the graduate students and staff members at the department of mechanical engineering of York University for their advice and support in making this research a success. My sincere gratitude goes to all the committee members who reviewed and accepted my scholarly work.

Lastly, I thank myself for standing tall, not being depressed and with perseverance, pressed on to success. I believe this is the start of something great I promise not to let all of you who inspired me down.

Thank you all once again for seeing me through this phase of my life.

TABLE OF CONTENTS

LIST OF TABLES

LIST OF FIGURES

LIST OF NOMENCLATURE

2D – Two Dimensional

3D – Three Dimensional

AM – Additive Manufacturing

CMT – Conventional manufacturing Technique

Co - Cobalt

DED – Directed Energy Deposition

EBM – Electron Beam Melting

EDS – Energy Dispersive Spectroscopy

FWHM – Full Width at Half Maximum

hBN – hexagonal Boron Nitride

HV – Hardness Vickers

M-AM – Metal additive Manufacturing

PBF – Powder Bed Fusion

PM – Powder Metallurgy

SEM-Scanning Electron Micrograph

SLM – Selective Laser Melting

SLS – Selective Laser Sintering

TaC – Tantalum Carbide

TEM – Transmission Electron Microscopy

TiC – Titanium Carbide

WC – Tungsten Carbide

WC-Co – Tungsten Carbide Cobalt

XRD – X-Ray Diffraction

CHAPTER 1: INTRODUCTION

1.1 Background

The world is developing at a very fast rate and people expect to have their lives as simple as it can be. Consumers expect to get the products they seek for as early as possible. Thus, a necessity is laid on manufacturers and industrial companies to meet the desires of these consumers in order to stay in the game. Specifically, in manufacturing companies, the need to cut down production time of products is a very important improvement segment that is currently being studied. Newly implemented technologies that offer improvements can be greatly appreciated by any process chain. A process chain involves the stepwise sequence of processes that are scheduled to wait in the background for an event. Most at times, these sequences/processes trigger a separate event that can, in turn, start other processes in the sequence. An example may be found in the manufacturing of a cutting insert for lathe machines. Cutting inserts are processed using a manufacturing technology called Powder Metallurgy (PM). PM is the process of producing metallic materials and components from powders rather than through the classical ingot metallurgy route [1]. Typically, A die must be made in the process chain before we can go ahead and compact the product into a green state and sinter it. Sintering of materials describes a process whereby green products coalesce into a solid or porous mass by heating it (and usually also compressing it) without liquefaction [2]. Other classic process chain technologies including casting, forming, welding amongst others are still adopted for making specific parts. Nowadays, we are still used to making machines and parts from solid blocks of raw material, and then machining away material until desired shape is acquired. However, most of these technologies were limited in design and production time. These challenges downgraded the versatility of the technologies. Industries and consumers wanted to apply new design ideas and never get limited by the processing technique. Additionally, consumers requested products to be made against a time but still, the process chain lagged and made them not attractive again to use these technologies. All such techniques shall be grouped together and called Conventional Manufacturing Techniques (CMT). However, since 1980s there were new manufacturing technologies being developed, that used a different approach entirely. Those technologies are commonly named Metal-Additive manufacturing technologies

(hereinafter M-AM). The main underlying principle of all M-AM technologies, that will be listed later, is making part by adding material, instead of removing it.

1.2 Problem Statement and Research Objectives

In this research, WC-Co cemented carbides which are processed using M-AM are to be studied. The aim is to design a suitable process chain for producing WC-Co alloys using M-AM with appropriate mechanical properties. This is challenging because there are currently no approved powders for 3D printing cemented carbides such as WC-Co neither are there any 3D printers licensed to print cemented carbides. Additionally, there are no standards that are available for examining and qualifying printed parts. However, there is the need to evaluate the structure and properties of these processed parts to validate its adoption. This will aid us in correlating the processing technique to the microstructure of the alloy and thus, the mechanical properties of the alloy. Primarily, the main objective of this study is to understand the effects of the processing technique on the microstructure and mechanical properties of the most successfully printed WC-Co part so far. A further development is to adopt a one-step post-processing technique to improve the mechanical properties of the alloy including hardness, fracture toughness and wear properties. This will serve as a guiding framework to successfully produce a part suitable for industrial applications devoid of surface defects or other undesirable characteristics that would hinder successful part production, using a M-AM technology and a tool grade cemented tungsten carbide powder. Furthermore, on this main objective, the following are detailed objectives completed towards fulfilling this main objective:

- Assess the microstructural and mechanical properties of an as-printed WC-Co alloy.
- Perform post processing heat treatments on the as-printed WC-Co alloy and study the microstructural evolution and characterize the mechanical properties (hardness, fracture toughness and wear).
- Fabricate a new cemented carbide with hBN to give optimized properties.
- Assess the microstructural and mechanical properties of the new cemented carbide with self lubricating properties.

- Perform post processing heat treatments on the as-printed new cemented carbide and study the microstructural evolution and characterize the mechanical properties (hardness, fracture toughness and wear).

1.3 Research Methodology

Material powders and processing parameters of a recent study will be adopted for this research [3,4.] Powders will be acquired for processing on the EOS M280. EOS M280 is certified for processing customized powders using selective laser melting/sintering. Fabricated samples will be subjected to material and mechanical characterisation. This can be done by using advanced microscopy including Scanning Electron Microscopy (TESCAN VEGA 3) and mechanical testing techniques (hardness, fracture toughness and wear) to effectively understand the processing technique on the microstructure of the material. Information derived will be used to redevelop the process chain design which will aid in obtaining a better and suitable fabricated part for direct applications. In addition to the microscopy, chemical analysis will be adopted to understand chemical composition and phases distribution in the material. This will be done by adopting X-Ray diffractometer (Philips XRD) and the EDS component of TESCAN VEGA 3. With regards to the mechanical characterisation, hardness will be done by using a digital Vickers hardness testing machine. Fracture toughness test will be done using the indentation method. This method employs indentation cracks emanating from an indent done on the sample to estimate the fracture toughness. Using a macro Vickers testing machine and Carl Zeiss Optical microscope, the indent with cracks can be easily analysed for these samples. Wear tests were done using a Bruker UMT Tribolab. The mass of the sample before and after wear test was measured to determine wear loss using a high precision mechanical weighing balance. Using an alumina ball as counter body, the samples was oscillated on a linear axis terming it as a reciprocating wear test. Post processing heat treatment will be adopted to improve the mechanical properties of the printed sample. The same mechanical and microscopy analysis shall be carried out on the heat-treated samples to easily compare with the as-printed samples. The next goal is to use this manufacturing process along with the details of this present study to produce a new WC-Co material with a percentage of hexagonal Boron Nitride(hBN). This is done to help improve the wear properties of the material since hBN is known to possess great lubricating properties when in service comprising of contact

loading and friction wear. This will be a novel material for cemented carbides to have better properties for same applications that WC-Co is used for. Extensive alloy design and parametric studies would be done to successfully print a sample and a similar characterisation testing plan shall be done. This will include the post-processing heat treatment which is needed to improve the mechanical properties right after printing and the material and mechanical characterisation (hardness, fracture toughness and wear).

1.4 Summary of Findings

The summary was built from the relationship that the processing has on the microstructure and how this microstructure dictates the properties of the material. This section shall point out the important microstructural and mechanical characteristics of both materials and clearly define a conclusion for the scope of research. The summary has been defined below:

1. In the WC-17Co as-printed sample, four distinct microstructural features which included regular and irregular WC polyangular chips, W-C-Co phase dendritic structures, W-C-Co "foggy" (shapeless) regions and cobalt-rich background regions were observed. This was attributed to the repeated thermal cycles, large temperature gradients and relatively high cooling rates during solidification. The X-ray diffraction analysis showed that the as-printed specimen was made up of W_3Co_3C, W_2Co_4C, W_2C and the hexagonal WC phases.
2. After heat treatment of the as-printed WC-17Co sample at 400 °C, there was an increase in the number of regular polyangular chips with reduced size as a result of decomposition of the unstable W_2C phase chips to the more stable WC chips. The X-ray diffraction analysis identified no new phase in addition to the existing phases found in the as-printed sample.
3. After heat treatment of the as-printed WC-17Co sample at 600 °C, the general sizes of the regular and irregular chips had become smaller as a result of continues decomposition of the unstable W_2C phase chips to the more stable WC chips. The XRD diffraction patterns revealed a new W-C-Co (W_6Co_6C) phase which was not observed in the other specimens.
4. After heat treatment of the as-printed WC-17Co sample at 800 °C, the volume fraction of the irregular polyangular WC chips was significantly higher than was observed in the other samples. There were agglomerations of globular precipitates within the darker cobalt-rich regions in

addition to platelet WC chips. The XRD showed higher peak heights for the WC-Co phases and a new $WC_{0.5}$ phase.

5. After heat treatment of the as-printed WC-17Co sample at 1000 °C, the relative sizes of the regular polyangular chips were smaller and well-developed with a higher volume fraction of pores within the W-C-Co phase. The XRD analysis showed a high reduction in the peak heights of some of the W-C phases when compared to the other samples. A new W-C-Co ($W_{10}Co_3C_4$) was identified in addition to a significant reduction in the peak intensity of the $WC_{0.5}$ phase.
6. The heat-treated WC-17Co samples had relatively higher hardness when compared to the as-printed sample with the sample heat treated at 600 °C having the highest hardness. In addition, this sample had the highest fracture toughness (8.37 MPa√m), representing a 34% increase in fracture toughness, when the sample was compared with the as-printed sample (6.23 MPa√m).
7. In the as-printed WC-Co-hBN sample, a similar structure just like the as-printed WC-Co sample was observed. However, the grain sizes of the WC-Co-hBN samples were smaller than the WC-17Co samples. The EDS mapping showed an even distribution of the B and N across the sample. The X-ray diffraction analysis showed that the as-printed specimen was made up of W_3Co_3C, W_3Co_3N, $W_9Co_3C_4$, CoWB, $Co_{5.47}N$ and the hexagonal WC phases.
8. After heat treatment of the as-printed WC-Co-hBN sample at 400 °C, no new structures were observed in the sample however, the already existing structures had undergone a few changes. The sizes of these structures varied as compared to as-printed sample. The X-ray diffraction analysis identified no new phase in addition to the existing phases found in the as-printed sample. But, the peak intensities of the WC phases had reduced.
9. After heat treatment of the as-printed WC-Co-hBN sample at 600 °C, the general sizes of the regular and irregular chips had become smaller and the bigger WC chips were broken down. The XRD diffraction pattern revealed just one W_3Co_3N phase whiles a lot of W_3Co_3C phases which were not there were now present.
10. After heat treatment of the as-printed WC-Co-hBN sample at 800 °C, there was drastic depletion in the Co rich regions, and most WC chips were very big and are coalescing with other WC chips. The XRD showed higher peak heights for the W-C-Co phases including the new W_3Co_3C phases

that had been observed in the previous sample. The intensities of the W-C-Co phases were primarily larger than that of the ones in the as-printed sample.

11. After heat treatment of the as-printed WC-Co-hBN sample at 1000 °C, high temperature W-C and W-C-Co phases evolved in the sample. The relative sizes of the regular polyangular chips were very big with few Co rich regions. The XRD analysis showed a new phase which is the hexagonal BN was identified in addition to a significant reduction in the peak intensity of the WC phase.
12. The heat-treated WC-Co-hBN samples had relatively higher hardness when compared to the as-printed WC-17Co samples. The hardness value of the as-printed WC-Co-hBN was 3 times higher than the WC-17Co as-printed sample. However, the heat treatment process applied to the WC-Co-hBN samples decreased the hardness of the material. It is concluded that post-processing heat treatment of SLS printed WC-Co-hBN alloys provide good mechanical properties and this heat treatment at 1000 °C can be used to improve the structure and mechanical properties of the alloy.
13. The wear properties of the WC-Co-hBN samples were observed to be better as compared to the WC-17Co samples. The sample with the best wear properties was identified in the WC-Co-hBN sample heat treated at 1000°C. This was attributed to the formation of the hexagonal BN phase(hBN) captured on the XRD pattern. hBN is known to possess self lubricative properties and this is what made the sample more resistant to wear than all the samples.

1.5 Thesis Organization

This thesis is structured into six chapters. The following are summaries of the chapters:

- Chapter 1 introduces metal-additive manufacturing for cemented carbides and presents the problem statement and objectives for the research.
- Chapter 2 reviews the metal-additive manufacturing, its benefits and challenges as well as cemented carbides (WC-Co) material is also presented in this chapter.
- Chapter 3 describes the material and processing technique used in this research. A detailed description of the advanced microscopy and mechanical characterisation techniques used are also presented.

- Chapter 4 provides comprehensive observations of the microstructures of the as printed and heat-treated specimens of both WC-Co and WC-Co-hBN alloys as well as the mechanical results extracted from the standard mechanical characterisation tests.
- Chapter 5 discusses the main findings in this research based on the results of the microstructural and mechanical observations of the specimens. The final section of this chapter discusses how the results from this research can be applied in tailoring and designing process chains suitable for additively manufactured cemented carbides.
- Chapter 6 presents a conclusion of the results and future work from this study. In addition, references are presented at the end of this thesis.

CHAPTER 2: LITERATURE REVIEW

2.1 Introduction

This chapter defines and reviews additive manufacturing and cemented carbides. In detail, an introduction to additive manufacturing as fabrication technique is addressed in section 2.2. The relevant types additive manufacturing related to this research are being reported in section 2.3 while section 2.4 is a discussion of the advantages and importance of additive manufacturing to the industrial world. Section 2.5 also presents the challenges of additive manufacturing and 2.6 reviews provides a review on cemented carbides, its applications, material and mechanical properties among others. Finally, the scope and objectives of this research is presented in section 2.7.

2.2 Metal-Additive Manufacturing

Metal-Additive manufacturing (M-AM) is a modern method of fabrication process which is used in producing a functional engineering metallic component [5]. There is the adjunct foundation which comes from the manufacturing known as subtractive manufacturing which is being termed in this study as the conventional manufacturing technique (CMT). During its reign (CMT), products were formed by picking a bulk material, gradually and intentionally shaping out the product. Depending on the intricacies that the part being fabricated has, much time will be spent on delicate sections to get it carved out right. This was very time consuming and placed a limitation on the freedom of design that can be explored for specific structures. However, bringing M-AM tackled most of these problems which included the time consumption and freedom of design along with other benefits. In detail, the manufacturing technique forms a part or product by fabricating 2D layers on top of each other whereas the model or design is acquired from a computer aided design (CAD) model data. The material used during processing are micron-sized powders. These powders are spread on a platform periodically after which a laser is shot on with a precise movement to form the layer print. As a rapidly growing technique, companies and industries are adopting this for their different fabrications. This technology has proven its worth in almost every

sector including the biomedical and aerospace centre. Immense capabilities have not yet been mined. However, it is greatly known to possess diverse benefits.

2.3 Types of Metal-Additive Manufacturing

All metallic materials present a set of physical properties and attractive mechanical properties which makes them useful for many industrial applications. In metal additive manufacturing, processing of such materials may be treated differently under the same conditions. This is because, they possess different physical properties which include melting point. This has given rise to different approaches of processing metallic materials even though they all go through the same additive processing technology. Below are discussed the four established Metal-Additive Manufacturing processes that can be used to process different metallic materials including ceramics and cermet.

2.3.1 Powder Bed Fusion (PBF)

Powder Bed Fusion (PBF) is considered one of the growing techniques under Metal-Additive Manufacturing. The process involves a focused energy system which may be a laser or electron beam [6]. This beam provides heat energy that would be used to selectively melt or sinter a layer of powder bed. The powder bed is made up of tiny metallic particles which the beam focused on to melt. Based on the laser beam source, two kinds of powder bed fusion systems have been identified by the ASTM F42 Committee on Additive Manufacturing. The are namely Selective laser Sintering/Melting (SLS/SLM) and Electron Beam Melting (EBM) [7]. Both are known to use the same powder bed principles however, because of their specific laser sources, there is a little difference in their hardware set-up. The setup for the EBM is essentially a high-powered scanning electron microscope which is coupled with a collimator, filament and magnetic coils to effectively collimate and deflect the beam spatially. However, the SLM/SLS typically displays a system of lenses with a scanning mirror (galvanometer) to maneuver the beam's position. Also, the powders are also distributed differently for each system. EBM system use a powder hopper and a metal rake whiles the SLS/SLM system uses a powder hopper or different feeding system

and a soft distribution plate that drags powder across the build surface. We shall pay close attention to the SLS/SLM and its processes in the next sub-headings.

2.3.1.1 Selective Laser Sintering/Melting (SLS/SLM)

In this process, which are found under the PBF, they all share the same printing procedure where powder particles are selectively fused by a local thermal process generated from a laser in a layer by layer manner. However, they differ in the way the materials experience fusion and melting. 3D printed parts processed using SLS/SLM are done by applying a beam of laser energy to the powder bed by following the 3-D CAD descriptive data of the part which has been sliced into stacks of 2D figures. This 2D layer is formed by the laser beam which scans over the required cross-sectional area. This laser provides specific heat capacity used to melt, sinter and bond powder particles together. Subsequent layers are created by spreading a layer of powder on top of the previously processed powder and bonded at the same time by repeating the same scanning process. A schematic diagram of the process is shown in Figure 2-1. Though SLS and SLM follow the same processing principle described early on, it is important to distinguish them to note the difference between the two techniques. The main difference between SLS and SLM is that the SLM achieve a full melt of each powder particle found in the mixture during processing of the material in the chamber. However, sintering of powder particles is only prevalent in the SLS technique. Additionally, special cases whereby not all the elements found in the powder mixture gets melted since the laser power could reach only the melting point of one of the elements involved can be also placed under SLS [6]. This difference however does not deter many published reviews and articles to consider them as one process.

Most researchers who are interested in SLM are also interested in SLS. This is also the reason why this thesis also identifies both technologies as one. The technology has been tried for different metal alloys including aluminium alloys [8–12], titanium alloys [13–17], steel alloys [18–22], ceramic alloys [23] as well as high entropy alloys [24]. In this thesis, importance has been placed on the contribution and efforts of researchers to paint a general picture of materials processed in this field, its impacts and general properties. Automotive, military, rapid tooling, and space technology are considered as areas where application of SLS/SLM is promising with combination of the materials currently being researched. The feasibility of fabricating components for military

applications using SLS with HIP was demonstrated by Das et al [25, 26]. The medical field has seen much improvement from this technology too. Different researchers employed SLS/SLM to successfully create implants biocompatible for medical purposes [27-30]. Other outstanding ecological performing indicators of SLS/SLM process include reduction in emissions because fewer raw materials need to be produced, design for light-weight structuring with a weight reduction and design for performance and indirect usage of toxic chemicals like lubricant or coolant in any measurable amount [31]. The rapid development and improvement of the SLS/SLM technology creates an expectation in manufacturing in the next few decades. In due time, SLS/SLM will remain as the future of manufacturing as human lives continue to depend upon the quality and ease of use of its products in the manufacturing, transportation, medicine, sports and electronics sectors.

2.3.1.2 Electron Beam Melting (EBM)

This method of processing is very similar to SLS/SLM. Therefore, metal powder is laid on the printing stage. For EBM, instead of a laser discharging the energy, it is rather an electron gun that will be discharging an electron beam on the powder. A schematic diagram of the EBM setup has been shown in Figure 2-2. Consequently, it follows the same procedure that the SLS/SLM process follows. Pioneers of this method state that EBM produces less thermal stress in parts and therefore requires less support structure. Furthermore, it builds parts faster [32]. The capabilities of the EBM technique are unique making it very beneficial to the aerospace industry especially (prototyping and low volume fractions). The difficulties of machining including time and cost among different procedures are wiped out, which makes the parts promptly accessible for utilitarian testing or installation on a framework. Moreover, the manufacturing technique opens a way to new plan arrangements (e.g., cell structures) and weight-decrease choices. The energy density; a value calculated from a formula which combines the processing parameters that can be changed during processing; is known to be sufficiently high to liquefy a wide variety of metal alloys and composites. There has been an extensive research using this technique on materials such as aluminum alloys [33], tool steels (H13) [7], cobalt-based superalloys [8] and Titanium alloys, in particular, Ti-6Al-4V.

2.3.2 Directed Energy Deposition (DED)

This technique involves a pointed source of energy which has been established in previous techniques as a laser, electron beam, plasma or arc. Using this source of energy, metallic powders are melted from a wire being injected or fed from a nozzle [34]. In Figure 2-3, a schematic diagram illustrating the set-up of a typical DED system has been shown. The laser power is always controlled by a controller where the CAD drawing is also fed into. The controller also gives the options of setting printing parameters which may include beam diameter and scanning power during processing.

Despite of a better manufacturing flexibility in PBF technologies, products produced with the DED technology have greater overall benefits like higher density, defect-free structure, greater reliability, and superior mechanical property. This technique is stemming from the process used for welding where a material is deposited outside a build environment by flowing a shield gas over the melt pool. In the DED, the most successful type of mechanism has been by using a laser source and a feedstock which is powder fed. The first setup was done at Sandia National Laboratories and originally patented as the LENS process [35, 36]. Currently, multipass welding processing are being explored for DED process. This is because it has the potential to create and fabricate parts with large geometries. It utilises lower heat input values. However, this induces a high-volume fraction of porosity in the sample [37]. The nozzle is coupled with powder feeder and a gas supply system. These work together to gradually deposit the metallic powders at controlled rate on the workpiece. The laser head is outsourced by a high-power laser which is connected to a controller which controls the laser energy output as well as the CNC platform on which the part being fabricated sits on. As in PBF, powder hoppers must be filled, and a build substrate positioned. The substrate can be positioned in a stationary position (3-axis systems) or on a rotating stage (5+ axis systems) to increase the ability of the machine to process more complex geometries. The chamber where the substrate is located is enclosed so that the laser or energy source is isolated from the environment when in use.

Additionally, inert gases are not necessarily needed as in PBF techniques. However, for some nonreactive metals, a shield gas directed at the melt pool may provide adequate safety and resistance to oxidation. For reactive metals, including titanium and niobium, the chamber is flooded with an inert gas (argon or nitrogen). Just like in a PBF, the printed part is attached to the

substrate and must be removed through post processing techniques. These post processing techniques will also help relieve residual stresses and improve the mechanical properties of the material.

Research on DED techniques for materials include titanium alloys and steels [38–40] analyzed the fatigue fracture surfaces of DED titanium alloy and found that the failure modes of DED titanium alloy can be divided into three types: (1) cracks initiated from internal pore defects, (2) cracks initiated from internal lack-of-fusion defects, and (3) cracks initiated from the surface/subsurface of the specimen. With the improvement of DED process conditions and the development of hot isostatic pressing (HIP), the proportion of lack-of-fusion decreases significantly, but internal pores are almost inevitable and thus become the main factor affecting fatigue performance [41–43].

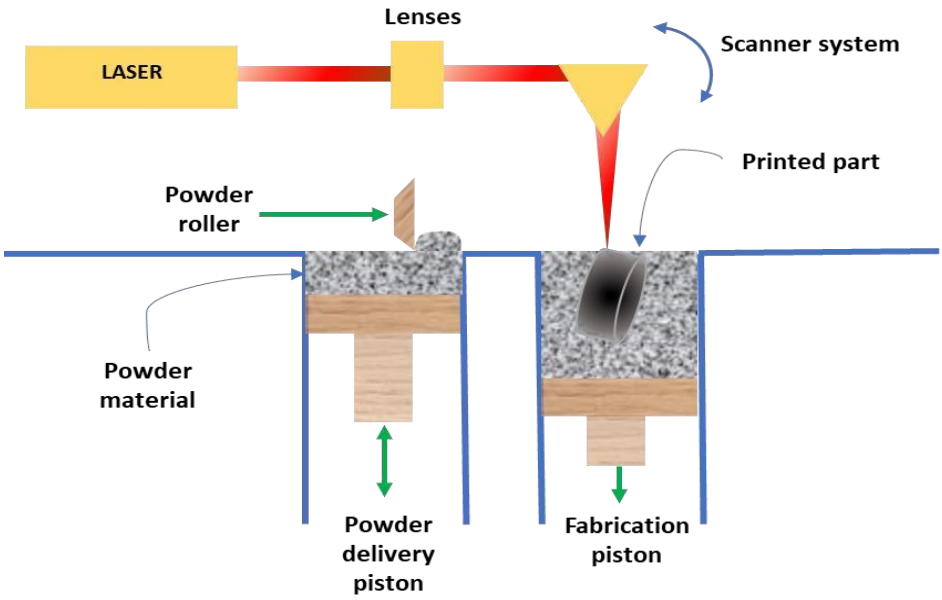

Figure 2-1 : Schematic diagram of the SLS/SLM as a Powder Bed Fusion system/manufacturing setup.

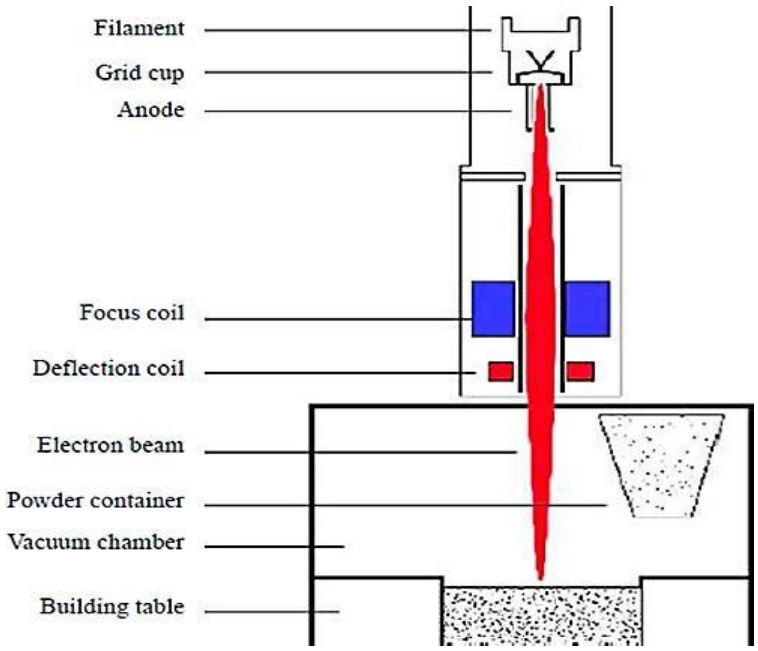

Figure 2-2 : A labelled schematic diagram of the Electron Beam Melting as an additive manufacturing technique. [33]

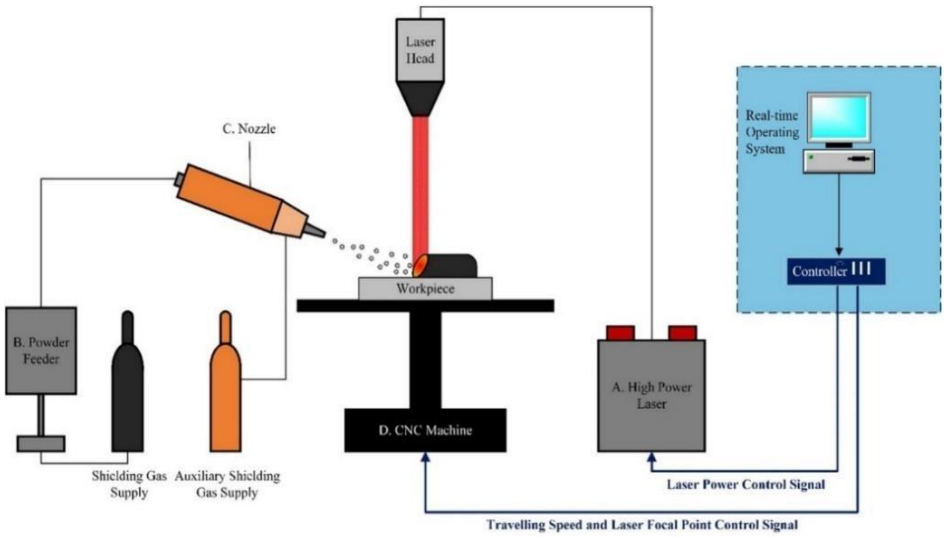

Figure 2-3 : Schematic and Process diagram of the Directed Energy Deposition Technique. [39]

2.3.3 Binder Jetting

The above technique follows a process just as the name explains. It basically deposits a binder on a sample of metal powder, cures the binder which holds the powder together. Consequently, the mixture is sintered or consolidated and sometimes infiltrated with a second metal. The infiltration process is done using a metal alloy of lower melting point as the infiltrate and it is done to densify the material. The consolidation process also in turn helps the material achieve uniform composition of a single alloy. Since this technique is essentially considered as a powder metallurgy method, porosity is a major concern of the parts printed using this method.

Extensive research on powder metallurgy and ceramics will pave greater strides for advances in binder jetting method for manufacturing [44]. The hardware setup is discussed using a known manufacturer of Binder Jetting systems: ExOne. ExOne is currently the major manufacturer of the printers for more than a decade now. These printers use bronze as the infiltration for most iron fabricated parts made with their system. Binder Jetting printers selectively deposit liquid binder on top of metal powder using an inkjet print head. When the binder dries, a delicate binder–metal mix (also alluded to as a 'green body') can be expelled from the powder-bed system. The green body can at that point be cured to provide mechanical strength, which can take 6–12 hours. After curing, the part is then going through a post-processing treatment at ∼1100°C for 24–36 hours to sinter the loose powder and to burn off binder, taking off 40% thick sintered metal portion. Infiltration set in when the partially sintered material is set in contact with a molten pool of a second material with a lower melting temperature than that of the sintered material. This permits infiltration of the liquid metal into the pre-sintered structure by capillary activity to create a denser part. Bronze infiltration of stainless steel can accomplish at least a thickness of 95%. Heat furnaces are also adopted for post processing heat treatments to anneal the part and increase ductility [35]. This infiltration process which seems to be one of the main important things in binder jetting did not stem form the technique. Long before binder jetting, infiltration was a technique used for commercial production of materials. However, with the metal alloys, binder jetting introduced the consolidation which was an alternate process to infiltration that can be used to produce solid alloys. In detail, it works by designing in distortion of the part geometry to accommodate uniform shrinkage during sintering. Inconel has been recently developed for Binder Jetting by ExOne and is likely just the start of the development of additional consolidated metals for the platform. The

material properties of the consolidated parts have not been published, so the quality cannot be currently compared to other AM methods. Surface finish is in line with many PBF processes. The surface finish of parts after annealing is quoted at 15 μm, and postprocessing is quoted to reduce roughness to 1·25 μm [35]. It is interesting to note that there are only limited published works with reference to Binder Jetting than for PBF and DED. Therefore, a detailed description of processing details is not addressed in this review. However, many research topics need to be addressed in the future, including binder burn off, geometrical accuracy during consolidation and unique infiltration materials.

2.3.4 Sheet Lamination

This technique involves the stacking of metal sheets that have been cut with precision which end up forming the 3D object [45]. The stacks are joined together by an adhesive or using a metallurgical bond like brazing, diffusion bonding, laser welding, resistance welding or ultrasonic solidification [46, 47]. How the metal sheets are cut is very important for every sheet laminating printer. Sheets may be either cut to the specified geometry prior to adhesion or machined post adhesion. In doing that, sheet lamination has the advantage of low geometric distortion (the original metal sheets retain their properties), ease of making large-scale (0·5 m × 0·8 m × 0·5 m) parts, relatively good surface finish and low costs. However, most of the products formed using sheet lamination cannot be used for applications which need to withstand shear and tensile loading. Geometric accuracy in the Z-direction is difficult to obtain due to swelling effects. Anisotropy is very prevalent due to the binding process and agents. Steps involved in a brazing sheet lamination process are shown in Figure 2-4. The sheets in this example are coated with flux (or low melting alloy), which acts as a brazing alloy for joining these sheets.

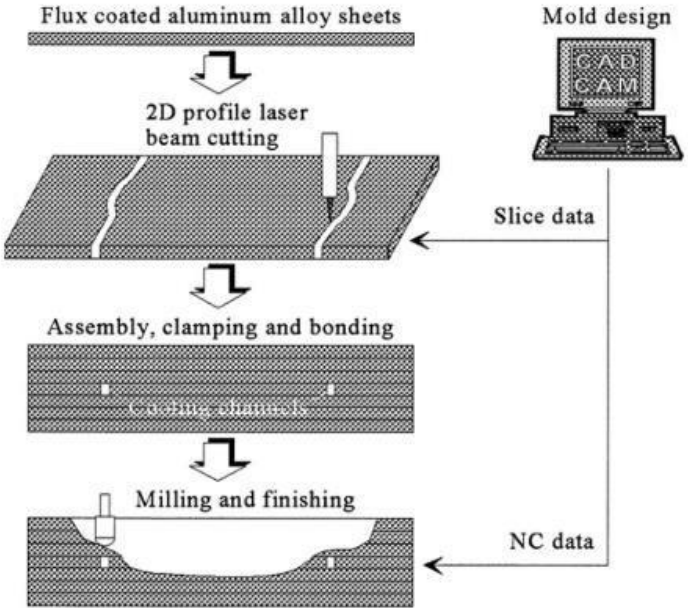

Figure 2-4 : Schematic illustration of sheet lamination process to make injection or metal forming moulds [48]

2.4 Advantages of Metal-Additive Manufacturing

One important advantage this manufacturing technology can boast of is the reduction in lead times of a process chain for any product starting from design to final fabrication step. In other words, it is considered as a faster transition from the design stage to the production of the final part. The cut off time is coming from the mold creation part of the process chain as well as instrumentation. A 3D printed part does not require any specific tool or machining devices to process the part because there is no need to mill or tool the part in order to adjust its shape or create holes or even add any connecting elements. The only part now is just removal of supporting structures created during printing and surface smoothening of printed parts. Thus, using metal additive manufacturing translates into shortening lead times to days instead of weeks and months. For example, for producing parts on a large-scale basis, using injection molding seems financially reasonable. However, the molds need to be manufactured and then the speed of production line and the whole factory must be optimized. As a result, getting the first part may happen after 15 to 60 days, whereas in case of 3D printing, we can easily print the mold and use it for the injection molding translating the lead time to just 2 or 3 days.

Secondly, there is a huge reduction in material used for the production as well as material wastage. In conventional manufacturing, a bulk solid figure has material subtracted in order to carve out the product whereas in 3D printing, raw material is added and formed layer by layer. Some of these layers can be as slim as 5microns being built up. Therefore, limited resources are used reducing cost of material for production and making the manufacturing technology very resource efficient. Additionally, the world currently seeks to reduce carbon waste released into the environment and thus it is encouraging the research of lightweight materials to be adopted. This is very important for automotive and aerospace industries who are the major culprits of this problem. In 3D printing, parts can achieve as low as 25% of final mass of products produced using conventional manufacturing techniques. This makes it attractive for the industries who can now create lighter products for the applications and hence reduce the emission of carbon into the atmosphere. Figure 2-5 shows image taken at European Space Agency Conference which was used to describe the minimizing of weight of a product by redesigning the product geometry. Making better products with seemingly higher mechanical properties yet still a lower density or weight is just an innovation this M-AM offers without limits.

Another advantage goes for the engineers who sit down to creatively design the products and parts. Looking at the products from their perspective, this technology is allowing them to create complex and unique structures without fearing limitation of manufacturing technique. A designer just must think of an idea, draw it and just feed it to the 3D printing machine and within a short while gets what he thought of (Figure. 2-6). Traditionally, you would have to consider how easy it is to manufacture your product and thus you would have to expel some design ideas on your product. Also, complexity of the part does not generate additional costs. Where it was previously necessary to use several separate parts within a twisted or welded structure, now just one part is required, and it can be manufactured as a single piece. Effective and well-advanced structures including nanostructures which are being available today for nano-engineering and technology can be realised just by adopting this manufacturing technique for such products.

Lastly, repair and maintenance of complex structures can become very explosive using this manufacturing technology considering for example space structures and machines which stay in space for a long time. Spare parts can be printed just out in space and can be used to replace defunct

parts without sending someone to space. The cost of organising a trip as such is very costly and this technology can just slash that with just its innovation. Manufacturing industries here on land can also be able to repair parts which are difficult to reach unless you dismantle the whole part or just replace the whole part with a new one.

The manufacturing technology has more interesting advantages in store and who knows the immense opportunities we can mine from this technology for years to come. The global value of M-AM products and services (all materials) is expected to grow considerably as stipulated by different reports. Whether as a replacement for existing production methods on economic grounds, or because of the ability to produce components that have up until now been impossible, M-AM will certainly have an impact on the future of manufacturing. The growth in the M-AM industry is predicted by many to be rapid and substantial, as more companies develop production equipment, more materials become available and more end-user industries adopt the technology. The global value of the industry will reach over $10 billion by 2021. Governments throughout the world have identified AM as a growth industry and are funding research projects to further develop the technology.

Figure 2-5 : A image taken at European Space Agency Conference which was used to describe the minimizing of weight of a product by redesigning the product geometry [49]

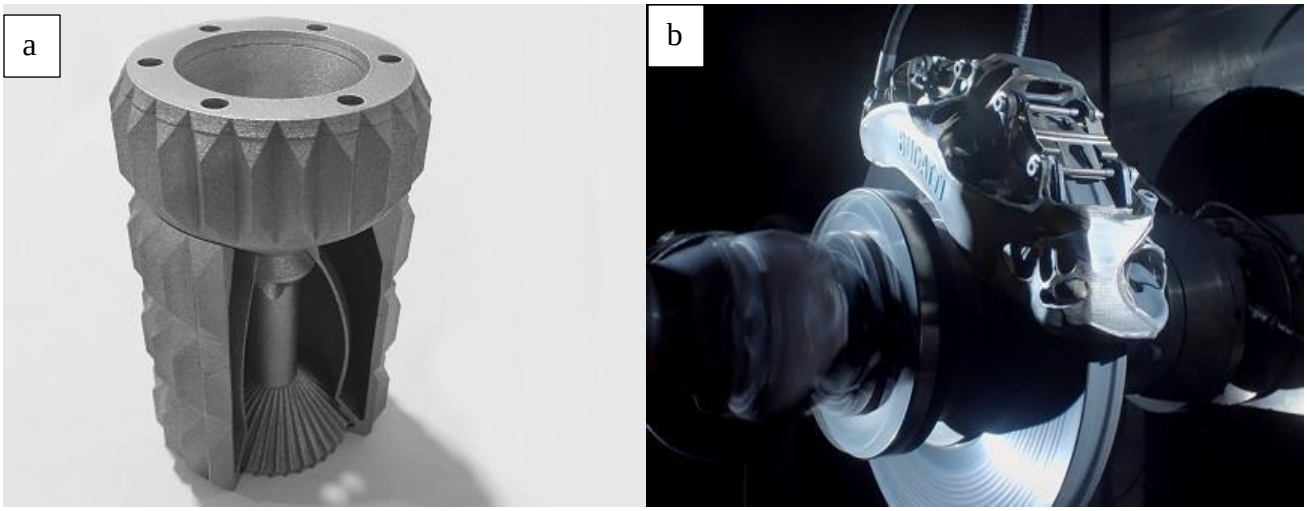

Figure 2-6 : (a) Designers of the Farinia group have limitless design for machine parts because additive manufacturing [50] (b) The titanium brake caliper under test conditions showing no limitation to freedom of design and performance. (Courtesy VW Group)

2.5 Challenges with Metal-Additive Manufacturing

As discussed early on, M-AM deems a characteristic fit for many industrial companies around the globe. It added advantage and approach to making complex and lightweight, yet solid structures make it very appealing. Be that as it may, in its present state, M-AM faces some key difficulties that must be tended to before it will be broadly received by the industries. Additionally, it has made a lot of buzz in businesses over the world promising an adaptable and financially savvy option in contrast to traditional manufacturing. Be that as it may, most organizations are still in the beginning period of adoption because of different financial and technical difficulties with M-AM. An examination from USP showed that M-AM right now speaks to an insignificant 0.04 percent of the worldwide manufacturing market. That being stated, the adoption of M-AM could push ahead quickly if researchers can address the present issues related with the printed parts. Some of the present issues, limitations and challenges related to M-AM are described as follows:

2.5.1 Residual Stresses

During printing, irregular and heating of the chamber which is directly affected by the melting and solidification of the material in the chamber end up generating residual stresses in the material right after processing. These stresses are basically known as the stresses that remain the sample even after the material after printing has reached equilibrium with its environment. According to Withers and Bhadeshia [51], residual stresses are grouped according to the scale at which they occur. They therefore classify them under Type I, Type II and Type III stresses. Type I is described as stresses that emerge due to the shape of the material which includes the dimensions and orientation. Type II and II relates to the microstructural part of the material. This includes phase transformations and dislocations that occur at atomic scale level. All these types lead to undesirable cracks which propagate upon loading of the part, delamination of the printed layers, and warpage of the whole part against the substrate during processing. This in turn stops the spreading process of the powder particles and affects the build causing it to fail even before it is used for application. This problem affects the length of production of part which we wanted to escape with the conventional manufacturing technique. Not only does it affect time but also leads to waste of the material, energy and requiring extra efforts for designers to change the design.

Figure 2-7 illustrates such issue, in which the cracked and deformed component stops the powder deposition, leading to a failure build. The other challenge is exhibited in the separation of the part built from the substrate on which it was built. The deformation results in limited load resistance, dimensional inaccuracy, and reduction of fatigue performance of the component to more than 10 times compared with the conventional bulk material. For example, an implant was successfully printed out in Ti6Al4V using laser powder bed M-AM, but once it was cut from the build tray, the inherent residual stresses lead to undesirable deformation. In other cases, residual stresses are desired for the part being produced. An example is glass plates that are rapidly cooled to introduced compressive stresses in the surface area of the plate. This increases the load the glass plate can bear and thus prevent crack growth. However, in M-AM, these residual stresses are mostly undesired and therefore a challenge. Because they cause deformations from the intended shape or irrelevant phase transformations which can make it very difficult to identify mechanical properties of the material itself. Thus, reducing the strength of the material and help incite crack propagation in the material. It becomes even weaker and a failure when external loads are applied to the part. In the M-AM process, these residual stresses as explained earlier are caused by the large and irregular thermal gradients during processing which are inherently present during processing.
The first mechanism that induces the stresses is called the temperature-gradient mechanism.

Figure 2-7 : An optical image of a part produced using SLM having distortion in the build of the part due to cracks developing from residual stresses at the edges of the part[49].

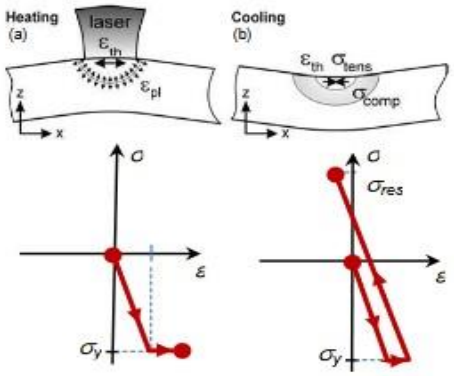

Figure 2-8 : A schematic diagram that illustrates the temperature-gradient mechanism that happened in the processing of materials during AM[50]

This was borrowed from the stresses that come up in laser bending of sheets. Owing to rapid heat of the surface, the laser does not present a slow heating rate and a steep temperature gradient develops at the surrounding of the beam on the sample (Figure. 2-8). The strength of the powders or material reduces simultaneously. Since the layer is being built on another layer, it is restricted in the amount of expansion that can occur and therefore induced elastic compressive strains, Then the yield strength is reached, plastic compression will occur.

The second mechanism is observed during the cooling session of the melt. Almost every researcher who has handled metal additive manufacturing has encountered residual stresses. It is a challenge that seems to have come and stayed with the manufacturing technique. However, current researches are being done to practically reduce the amount that be generated to a value that will not cause for alarm. Kruth [52] developed models that can be used to test for the residual tresses which included theoretical and experimental models. In his conclusion, he suggested that one step heat treatment procedure should be employed to relieve these residual stresses to the barest minimum before application or we incessantly heat up the chamber to a higher temperature than room temperature to reduce the thermal gradient during the processing. On the other hand, support structures are required in metal M-AM to support overhangs of the component to ensure manufacturability. These support structures are fabricated simultaneously with the component to anchor the parts and dissipate heat to the build tray in order to prevent distortion/delamination caused by residual stresses.

There are several published works in the past in the areas of reducing or relieving the residual stresses. support structure design for M-AM techniques. Both finite element models, experimental

models have been proposed to quantify and reduce them completely. Some them tried to change the printing parameters of the machine to affect the laser energy and perhaps reduce the stresses. Wu et al. studied the surface-level residual stress of SLM processed stainless steel 316 L-shaped bar (off substrate) in as -build state by digital image correlation method and neutron diffraction [22]. Residual stress near the center of part tends to be compressive and tensile near surfaces as shown in Figure 2-9.

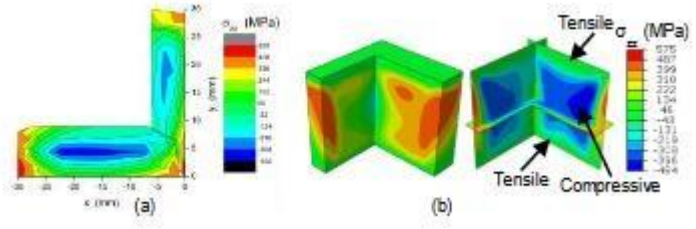

Figure 2-9 : A diagram which shows the compressive stresses within the material and tensile stresses at the surface of the material during material processing using AM techniques[50]

The effects of parameters including scanning strategy, laser power, scanning speed, and build orientation on residual stresses of different materials has been systematically investigated. A smaller scan island size and increased length energy density would result in a reduced residual stress field. Kruth et al. studied the effects of scanning strategies on distortion and concluded that the island scanning strategy (material deposited in a “chessboard” pattern) would cause less distortion than other scanning strategy [53]. X-ray diffraction residual stress measurement of SLM processed stainless steel and Ti6Al4V small-sized samples conducted by Yadroitsev et al. [54] has shown that residual stress in scanning direction is more tensile than in the perpendicular direction and reaches its maximum at the build-substrate interface. Kruth et al. [53] assessed the residual stress of the SLM processed part using the bridge curvature method. The method has also been adapted by other researchers [55, 56] to fast evaluate residual stress of SLM processed part.

2.5.2 Feature Size, Surface Finish and Geometry Scaling

In the fabrication of metal parts using AM, it is very important to consider surface roughness, geometrical accuracy and the minimum feature size. However, these parameters have not been considered greatly because parts fabricated using M-AM must go through post processing treatment which in turn change the parameters mentioned earlier. The smallest feature size that a design can make has been dependent on the diameter of the laser source or energy in the case of powder bed fusion methods and directed energy deposition. Table 1 below summarises the data discussed previously which talks about the typical layer thickness and minimum feature sizes of PBF and DED processes.

Table 1: Characteristic layer thickness and minimum feature sizes of the PBF manufacturing techniques

Process	**Layer thickness(um)**	**Minimum feature size/beam diameter(um)**
SLM	10-50	75-100
EBM	50	100-200
DED (powder-fed)	250	380
DED (wire-fed)	3000	16000

PBF techniques have an upper hand of creating smaller feature sizes than the other techniques. Additionally, SLM has a better resolution than the DED systems because of the powder feed systems related to each other. However, the powder fed DED has better resolution than wire fed DED, which can be attributed to the use of finer feedstock (powder vs. wire). The feature size of DED systems is so large that parts made with these techniques are limited to more simple geometries than PBF techniques. It is therefore very sad to take one design and using different additive manufacturing techniques, successfully print your object to look the same way. Also, researchers who are working from the mechatronics point of view realised that, the movement of the lasers and powder feed systems are not necessarily the same in the different systems. This affects the feature sizes and surface roughness of your material even though you may have an idea of the surface roughness using SLM technique, it may be different when you apply DED technique

to print the same object. Below in Figure 2-10 is an image that describes level of roughness that can be attained using post-processing techniques (right of image) as compared to the as-printed part (left of image).

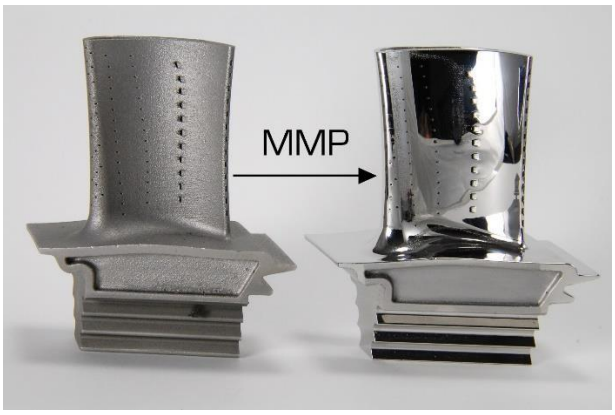

Figure 2-10 : A part produced using Selective Laser Melting which has been polished using micro machining process [57]

2.5.3 Build Chamber Atmosphere

The operating conditions of the chamber which includes the temperature, pressure and gas present have been known to affect the chemistry, processability and heat transfer of the material powders. Inert gases or vacuum have been used typically for printing objects in these systems. Using a specific inert gas requires specific processing conditions making the process a complex one to look at. Most of the metal powders tend to oxidise or collect moisture when exposed to air and even at higher temperatures, this is seen to increase exponentially [8]. This application was adopted from welding where inert gases are used to create an atmosphere where oxidation cannot occur. AM processes also have the same need [58]. However, with this, different parameters which worked for inert gas A does not work for inert gas B or parameters that worked for Powder A does not work for Powder B using the same inert gas. Paying close attention to small scale feature, the chamber conditions can gravely affect or cause a localised oxidation also. It is high time we concluded on which chamber conditions can work for which materials. It becomes even difficult when you would want to create a new material and process it using 3D printing. Thus, with no literature available on that, the processing of this new material becomes inundate and complex to understand and undertake.

2.5.4 Powder Customization and Acceptable Powders

One of the main challenges in AM is with the powders which are used in printing the objects. These powders are fed though the feedstock of the machine. The quality of the powders that goes through this feedstock also play an important role and the quality of print that will be made. The quality has been known to be determined by the size, shape and surface morphology of the powder, composition and amount of internal porosities. Therefore, using the required powders creates the physical quality especially the flowability and apparent density of the printed part. There are very different issues even regarding the way the powders are made (atomisation). By understanding, these powder conditions, a quality and acceptable object can be printed. A variety of techniques the techniques include gas atomisation (GA), rotary atomisation (RA), plasma atomisation (PA), plasma rotation electrode atomisation (PREP) [1]. Figure 2-11 shows the powder morphologies and of the different powder creation techniques and the internal sections of the powders showing the other porosities of the powders. Porosity in the powders are very common issues even with powders used in convention powder metallurgy methods. An example like gas atomisation end up entrapping gasses during the production of powders. These entrapped gases are transferred to the part during processing of the material in 3D printing. Porosity as a challenge would be discussed lately however, it is very important to note that, the conditions of the powders also create another challenge in the processing which is porosity. The need for cheaper powders ends up giving us low quality powders to use for the processing. In EBM, lower cost or quality powders that are produced using a hydride dihydride (HdH) process has demonstrated that it can lead to immense porosity on the part produced. However, these are all related to materials which have powders that have accepted for use in M-AM. Most of the materials have not been transitioned to M-AM even for studies because, there aren't powders readily available for the system to use. Additionally, every printing machine has a set of acceptable powders that can be printed on them. Thus, there is a limitation o the powders than be used to create a part as well as no option for creation of new powders to be done. Legal measures have also been set up so that powders have specific machines that they can only be used on. Additionally, the chemical composition of the powders must remain within the alloy specific specifications. It is therefore very important that we measure the elemental composition of the powders which includes recycled powders so that we can address evaporative

losses, contamination and reaction with the building chamber. The powders have become one major challenge for additive manufacturing. Many researchers are just working specifically on finding the right powders to use on the 3D printer before we can even start printing. A recent study on powder recycling in EBM of Ti–6Al–4V showed that oxygen content increased from 0·08 to 0·19% by weight, aluminium content decreased from 6·47 to 6·37% and vanadium content decreased [59].

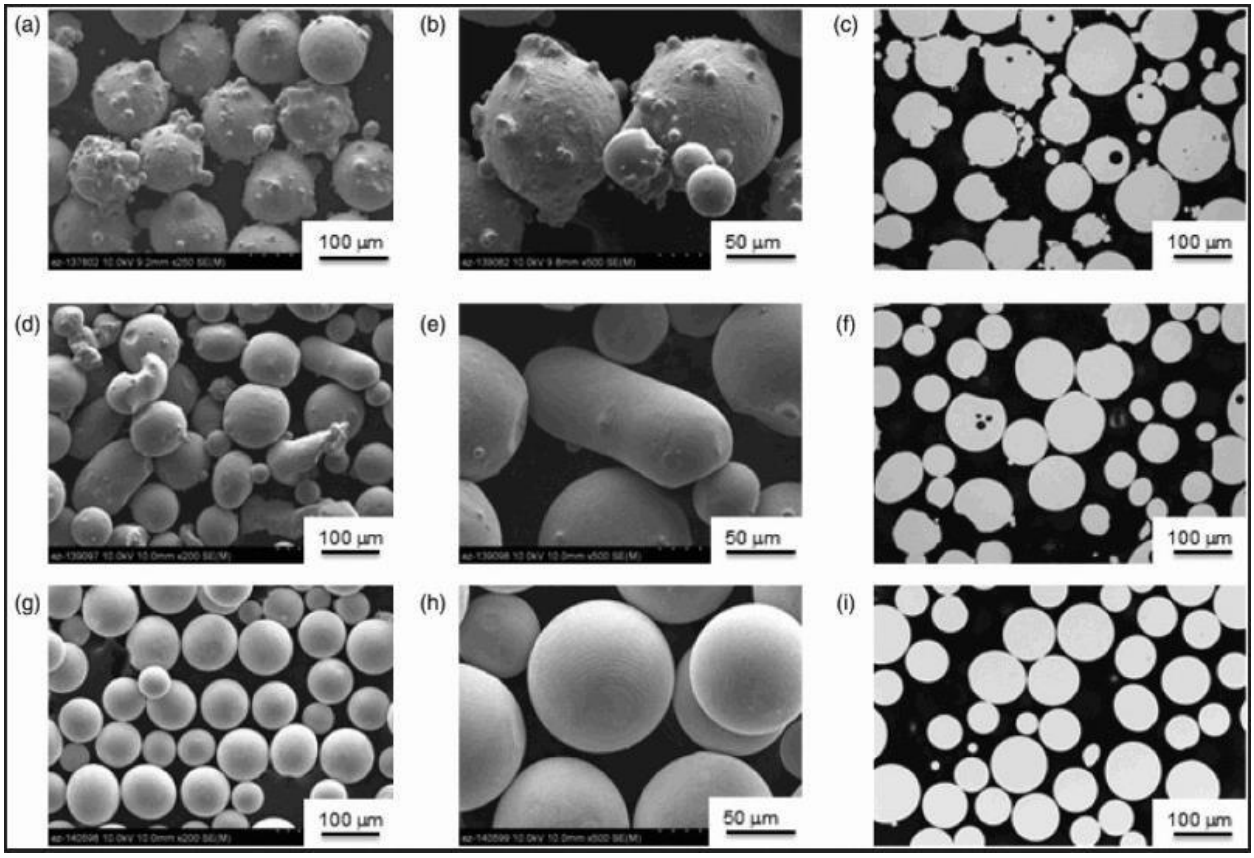

Figure 2-11 : : SEM micrographs of the powder morphologies and of the different powder creation techniques and the internal sections of the powders showing the porosities of the powders. (a) SEM 250× of GA, (b) SEM 500× of GA, (c) LOM of GA, (d) SEM 200× of RA, (e)

2.5.5 Void Formation/Porosity

The void development between consequent layers of M-AM parts is one of the significant downsides. Voids/Porosity is a common defect in metal AM parts and can negatively affect mechanical properties. This sort of issue happens because of diminished bonding between layers, subsequently causing sub-par mechanical performance [60, 61]. Porosity can be cause by the condition of powder used, the processing parameters, the chamber conditions and the melting and cooling characteristics which are material specific. Figure 2-12 shows a light microscopy of a samples that show porosity on sample due to the process parameters used and attributes it to lack of fusion and gas entrapment.

As previously discussed, gas pores may form inside the powder feedstock during powder atomisation. These spherical, gas pores can translate directly to the as fabricated parts. For most of the studies out there, porosity have been induced mainly by the processing parameters. You can evidently reduce or decrease the volume fraction of porosity in a material by simply tweaking the laser speed or laser power of the machine during printing. Pores formed by processing technique, known as process-induced porosity Process induced porosity is formed when the applied energy is not enough for complete melting or spatter ejection occurs. These pores are typically non-spherical and come in a variety of sizes (sub-micron to macroscopic). Other issues during processing have also been identified to contributed massively to porosity; like when enough powder is not supplied during processing or enough power is not supplied to a spot when processing, lack of fusion is said to occur. Lack of fusion regions may be identifiable by un-melted powder particles visible in or near the pore. When the applied power is too high, spatter ejection may occur in a process known as keyhole formation. In SLM, operating within this keyhole mode can create trails of voids and pores in the samples [62]. To limit spatter ejection, an operator will typically watch the process and tune parameters, while developing a new material processing strategy.

Process-induced porosity has other contributors, including the effect of powder consolidation from a loosely packed powder bed to a fully dense part [62]. Powder is distributed onto the processing surface and includes particles larger in diameter than the layer thickness, which upon melting are intended to consolidate into a layer of the correct height.

Shrinkage porosity (sometimes termed ‘hot tearing’) is the incomplete flow of metal into the desired melt region. Spatter ejection may also lead to regions of porosity. With optimised melting parameters, process-induced porosity can be reduced to very low levels in DED, SLM and EBM (less than 1% porous) [63, 64]. The relationships among lack of fusion, shrinkage regions and cracks have not been fully studied in AM material. However, work has been done to explore the effect of process parameters (beam speed and beam power) on the formation of process-induced and powder-induced porosity [65].

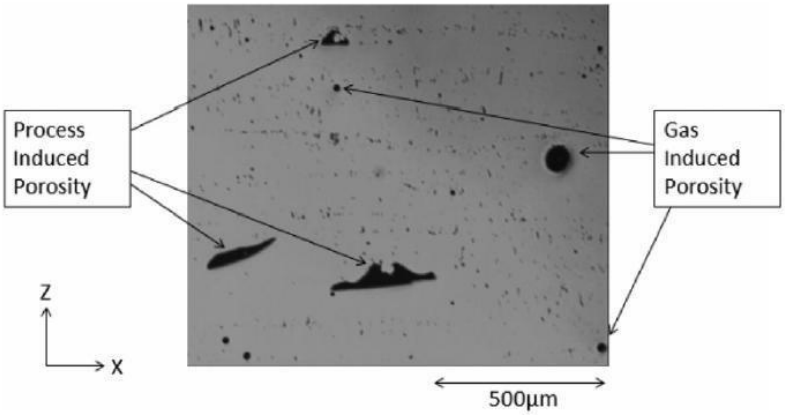

Figure 2-12 : Light microscopy of a 3D printed sample that shows porosity on sample due to the process parameters used and causes of porosities have been attributed to lack of fusion and also gas entrapment [35]

2.5.6 Cracking/Delamination and Swelling

Defects are formed from the processing temperature. Especially, cracking of the microstructure of printed materials may occur during solidification or subsequent heating. Macro cracks can also be attributed to porosity that have joined up together to form a crack. Delamination which causes cracking in the 2D layer is also a common defect. Delamination is the separation of adjacent layers within parts due to incomplete melting between layers. This may occur due to incomplete melting of powder or insufficient re-melting of the underlying solid. A high processing temperature may lead to the swelling or melt balling of the melt pool which happens because of the melt pool size and surface tension of the melt pool/These are avoidable defects which can be controlled using the processing parameters. However, some cracks can also be dependent on the material being used

for processing and these can be unavoidable cracks. There are different material-dependent mechanisms for which cracks form in AM material [66]. There is a crack type called solidification crack which arises if too much energy is applied, and stresses are induced between solidified melt pool areas against areas yet to solidify. This type of cracking is dependent upon the solidification nature of the material (dendritic, cellular, planar) and is typically caused by high strain on the melt pool or insufficient flow of liquid to inadequate supply or flow obstruction by solidified grains [67].

Thus, it is known that higher energies which lead to higher thermal gradients in the material during processing lead to high thermal stresses which end up inducing cracks within the material. This is what is needed for solidification cracking to occur. Grain boundary cracking is cracking that nucleates or occurs along grain boundaries of the material. The origins of this type of cracking are material dependent and depend on the formation or dissolution of precipitate phases and the grain boundary morphology. Using process parameter to minimise have become very challenging.

Solidification cracking and grain boundary cracking are both phenomena that occur within the microstructure. Thus, cracking is sometimes generally used to describe macroscopic cracks in the material which was discussed earlier to emanate from delamination and swelling. Lack of fusion has been clearly taken off by applying post processing treatments. However, the effects of delamination are macroscopic and cannot be repaired by postprocessing.

Swelling is the rise of solid material above the plane of powder distribution and melting. This is like the humping phenomenon in welding and occurs due to surface tension effects related to the melt pool geometry [68].

Melt ball formation is the solidification of melted material into spheres instead of solid layers, wetted onto the underlying part. Surface tension is the physical phenomenon that drives melt balling, which is directly related to melt pool dimensions. Figure 2-13 depicts an image of both the metal ball formation and delamination of EBM processed steel alloys.

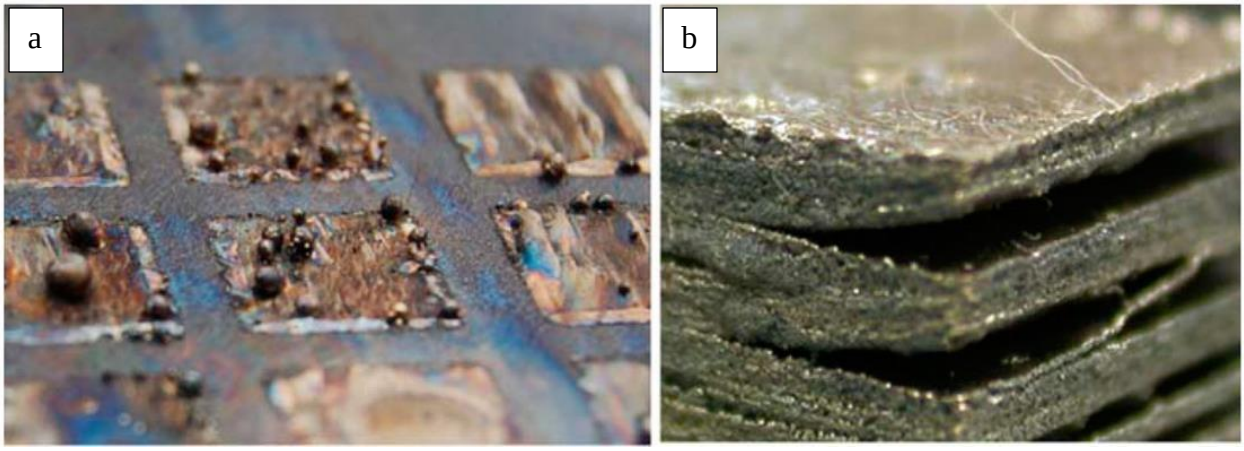

Figure 2-13 : Optical images of (a) metal ball formation and (b) delamination in stainless steel alloys fabricated by EBM.:[35]

2.5.7 Substrate Adherence and Warping

In M-AM processing, a substrate is needed for it acts as base on which the part is built upon. The use of the substrate is a standard procedure in M-AM. However, it adds additional work during post-processing. Metal parts are printed on this substrate because of mechanical adherence of the first layers of the part being built. The substrate can be left at room temperature or heated to a peculiar temperature to ensure effective fusion of the layers [68]. Most metal deposits form ductile interfaces and must be cut off the substrate during post-processing. Ti–6Al–4V deposited on stainless steel 304 substrate forms a more brittle interface that can be removed by application of force, without cutting [31]. This kind of interface is desirable for decreasing the number of postprocessing steps. Due to that, substrates tend to warp during and after the processing of the materials. This can be due to the operating temperature of the AM process, the heat treatment of the substrate prior to use or due to differential coefficients of thermal expansion. Some processes use a substrate of the same material as the build, like stainless steel, to reduce this effect. The ultimate result of substrate warping is distortion of part geometry within the affected layers and possible lack-of- fusion or delamination at the transition region back to unaffected material. Substrate warping is a form of stress relief that results in permanent plastic deformation. Recent work to model substrate distortion has rationalised the progression of stresses with thermal history in EBM. The same mechanisms that cause substrate warping can also lead to major issues with residual stress [68]. Researchers also wanted a way to quantify the warping effect. In that test

objects were printed and analysed (Figure 14) and used to obtain warp index values for different processing conditions [77].

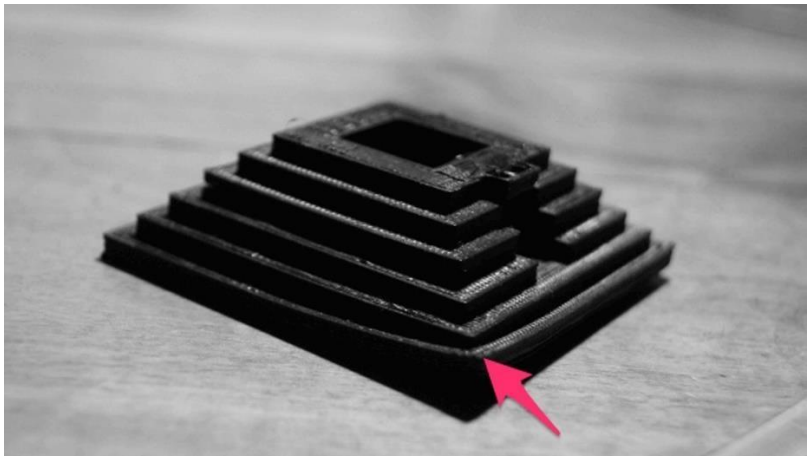

Figure 2-14 : A curtain test object printed to analyse warp index.[69]

2.5.8 Limited Number of Standards

Producers are being bottlenecked by costumers, government and competitors nowadays. The reason being that, they have the desire to produce products using this new M-AM method available. However, it seems that they do not have the readiness to delve into the technology very soon. This has become a very practical problem to the manufacturing, automotive and aerospace industries. Most of the functional parts need to meet a technical standard for it to be used. In detail, they require producers to certify the quality, adaptability and consistency of the parts they produce. But these manufacturers do not have the necessary standard available for their revision and reference for additively manufactured parts. Even the necessary parameters that you need for a specific material and the specific printer that is feasible for it are not available. Currently, Since the melting and cooling is so rampant, designers and producers discover it troublesome to quantitatively decided the right process chain to follow for different metal alloys. Without predictive simulation, it is hard to control the material's quality. High-temperature materials used for jet engines are usually critical components, requiring ultra-high mechanical performance. Therefore, it is important to perform reliable simulation to optimize processing parameters for the best quality of the 3D-printed components. However, these are not readily available to the

manufacturers. Enough research has not been one to actively use for making a for example a standardised bolt from steel. Recently, new standards were set up for additively manufactured parts which is being currently filled up with data [7]. Testing procedures which look aa little different from the conventional manufactured parts' testing procedures are also been document for references. The start of this standards has proven a steppingstone for researches to quickly delve into additive manufacturing and sufficiently provide the necessary data for documentation and values for modelling applications.

2.5.9 Inhomogeneous Mechanical Properties and Microstructure

Another challenge that can be observed with AM is the existence of anisotropy in microstructure and mechanical properties. Because of the layer by layer processing, there is a thermal gradient formed during processing and this is where all the challenges related to the mechanical properties come in as discussed earlier. The AM parts often results in different microstructural and mechanical properties along build direction and the other directions. In detail, during the processing, these different powders go through irregular heat and cooling cycles with different cooling rates.

Every material has independent phase diagrams which portrays the temperature and time dependent effect of developed phases in a material on the material and mechanical properties of the material. These phases are stable at different temperatures. The size, volume fraction and spatial distribution of these phases builds up the microstructure of the material which in turn dictates the mechanical properties of the material. These phases obtain equilibrium thermodynamically which makes it stable and easy to identify on the microstructure and through X-Ray diffraction and Electron Microscopy techniques. However, when the material processes undergo irregular heating and cooling transitions and rates, this can cause nonequilibrium phases to appear. These phases are known to be unstable at room temperature. This means that, it can change its phase just by the product sitting on a table somewhere. Imagine this as a structural material which has phases that change with regards to small change in temperature. This affects the bulk mechanical properties of the material. Thus, the part can fail anytime, and this cannot be predicted. Most of the M-AM samples experience non-equilibrium phases developing after processing. Figure 2-15 shows some materials that were processed using metal additive

manufacturing methods which exhibited non-equilibrium phases such as high temperatures phases and unstable room temperature at service conditions phases. The unpredictability of the material also called for a better understanding on the necessary measures that can be made to reduce the instability or fully remove these phases from the material completely. Most researchers proposed post-processing heat treatments which will either reduce residual stresses as well as change the microstructure or help dissipate the non-equilibrium phase.

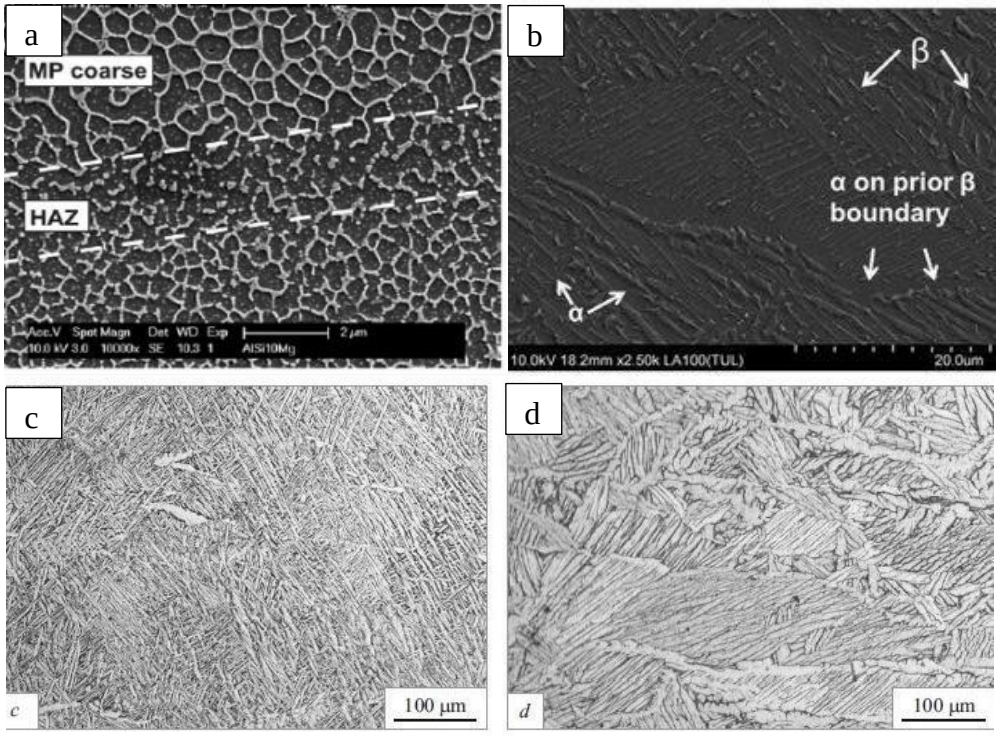

Figure 2-15 : SEM depicting non-equilibrium phases and confirmed by their corresponding XRD analysis from each of these research studies. (a) aluminium alloy processed using SLM [70], (b) BSE image of Ti-6Al-4V alloy fabricated using EBM [71], (c)Microstructure of alloy VT6 after SLM and 2-h annealing at 950°C (d) and 1050°C (d) [72]

2.6 Cemented Carbides

2.6.1 Introduction

The onset of cemented carbides (WC-Co) emerging to the public started with the idea of supplanting drawing dies made from diamond wires with tungsten filament wires. The name was derived from the constituents present in the material. It is basically composed of a ceramic and metal. Together, they combine to form a 'cermet'. The ceramic part is a combination of a metal and non-metal which is in this case tungsten and carbon. The ceramic is known to provide the hardness of the material which the metal is added to impart some level of ductility to the material. This material (WC-Co) became one peculiar one which had extraordinary properties (high levels of hardness and wear resistance). The first alloy was made in Germany by [73]. From then, the material has been widely accepted as an appropriate material for cutting tools, molds, drill bits, inserts as well as consumer products such as belt hooks and rings. In detail, cemented carbides possess high hardness and elastic modulus, low coefficient of thermal expansion, high wear and corrosion resistance, chemical and thermal stability during high temperature operations [74]. Lately, the material is being adopted in nuclear generation setups because of its ability to retain its mechanical properties even at elevated temperatures. The blending of the hard-ceramic WC particles with a soft metallic binder delivers a composite with ideal mechanical properties for such purposes. The most common binder element(metal) used is usually cobalt (Co). Based on the weight percent of the binder, the material can be applied for different applications. Figure 2-16 shows a graph of how the different combinations of WC grain size and cobalt content in cemented carbides, are used for different ranges of applications. The lines are all indicating hardness values (HV). However, other metals like nickel (Ni), chromium (Cr), iron (Fe) among others have been tried as alternatives. For example, Ni was introduced to help reduce wear rate in dry sliding wear applications because of the softening effect it gives to the microstructure [75]. Also, the addition could also improve the material's resistance to corrosion just like adding molybdenum (Mo), and chromium (Cr) [75]. Even though the blending of the ceramic and metal provide very attractive mechanical properties, it has strongly depended on the microstructure that the manufacturing process gives to the product. Some of the important factors that influence the properties from the

microstructure include the WC grain size, the binder phase content, the mean -free path of the binding phase, and contiguity of WC grains [76].

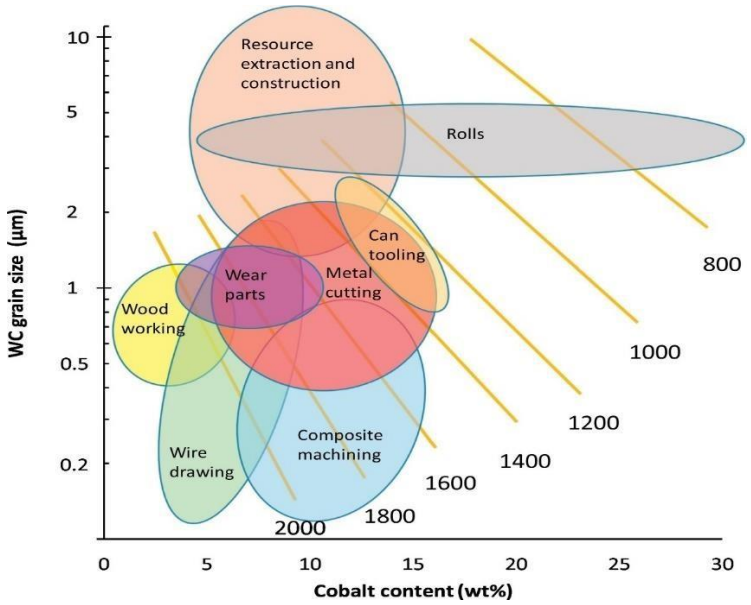

Figure 2-16 : Combinations of WC grain size and cobalt content in cemented carbides, showing a wide range of applications. The lines indicate values of iso-hardness (Vickers HV). Data from AB Sandvik [77].

2.6.2 WC-Co Structure

The structure of the WC-Co material comprises of a WC phase and compounds of W-C-Co, CoW and Co-C. These W-C-Co compounds come together to form the binder phases. The carbon content corresponds to the theoretical value of the stoichiometric composition, 50 at. %C (~6.13 wt%C). The WC phase also known as δ-WC which tends to be a conspicuous phase in all the common cemented carbides. It is identified as a non-oxide ceramic which has hexagonal closely packed layers of W particles isolated by closely stuffed layers of C filling one-half of the interstices, giving rise to a six-fold trigonal prismatic coordination for the atomic structures. The lattice shape is hexagonal, with grid parameters a = 0.2906 nm and c = 0.2837 nm (Figure 2-17) [78, 79]. However, two other types of WC phases also exist including $WC_{0.5}$(normally named β-W_2C) and γ-WC_{1-x} which are stable at specific elevated temperature ranges. Their associated structures of WC were confirmed by electron diffraction studies [80, 81]. β-W_2C is also a hexagonal compact (hcp) metal sublattice with the C atoms partly filling the octahedral interstices;

the second form(γ-WC_{1-x}), stable in a rather small temperature range at high temperatures, is a cubic NaCl type phase composition where x≈0.4, in which the face centered cubic (fcc) interstitial sublattice is partly occupied by C. β-W_2C crystallizes in three structure types: PbO2, Fe2N and CdI2 types, denoted by β, β′ and β″, respectively. These polymorphs are stable at different temperatures and compositional ranges [80, 81].

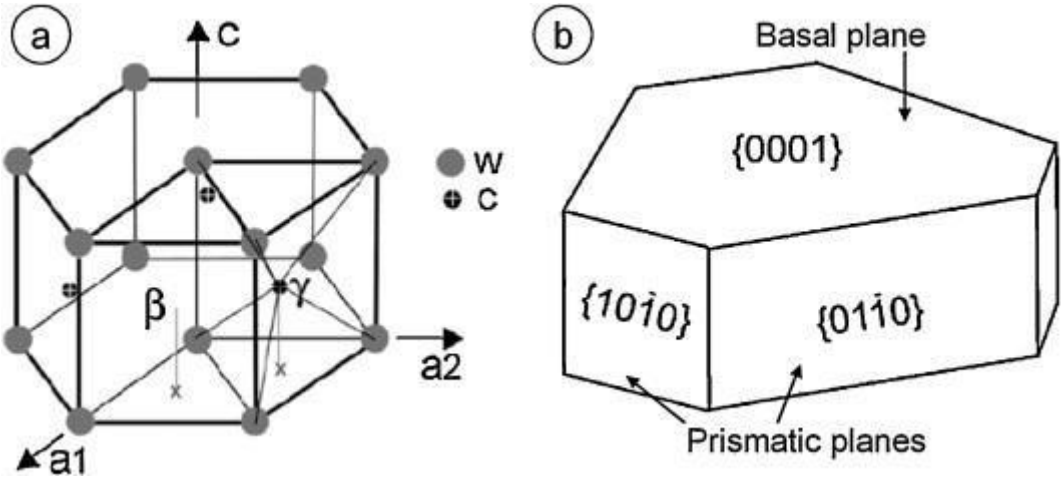

Figure 2-17 : Schematic diagram of the crystal structure of the δ-WC phase [76]

Recently, a phase diagram in the W–C system was proposed in order to assess more accurately this system (Figure 18). It can therefore be seen that W_2C forms between 1250°C and 2516C whiles WC_{x-1} forms at temperatures above 2516C. The W_2C phase forms from an eutectoidal reaction between elemental W and δ-WC at 1250 °C, melts congruently at approximately 2758 °C and forms eutectic melts with the W solid solution at 2215 °C and with γ-WC_{1-x} at near 2715±5 °C [80]. Phases of WC stoichiometry are obtained as intermediate products during WC production. The γ phase results from a eutectoidal reaction between β-W2C and δ-WC at 2516 °C and melts at approximately 2785 °C. δ-WC is the only binary phase stable at room temperature and has almost no compositional range up to 2384 °C but may become slightly carbon deficient between this temperature and its incongruent melting point.

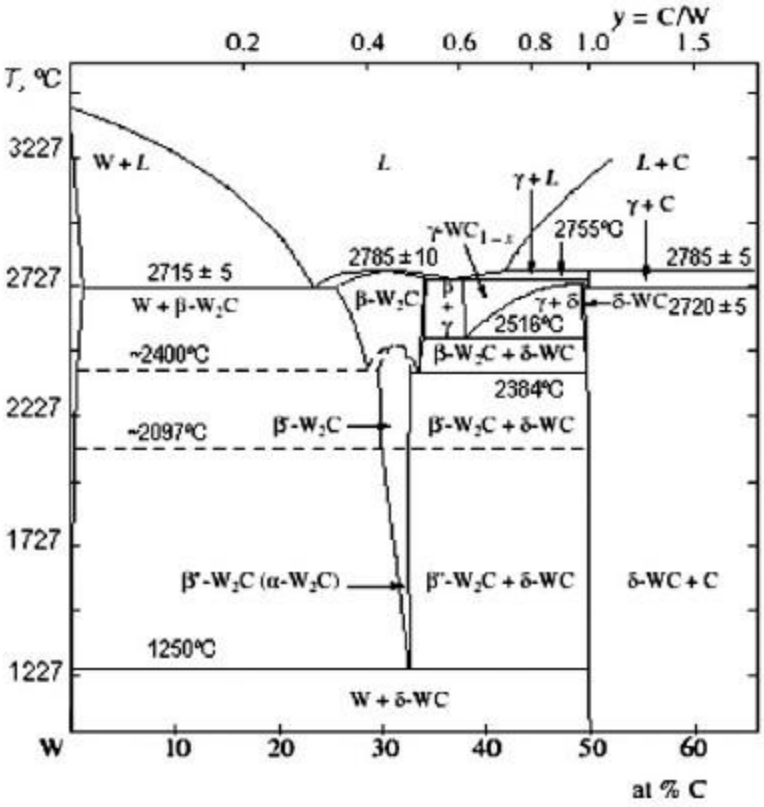

Figure 2-18 : The phase diagram of the W-C system [80]

These days over 90% of all WC-hard metals prefer to use Co as binder metal with weight percent somewhere in the range of 3 and 30 wt.%. The obvious prevalence of cobalt, generally to different binder metals, is identified with its best comminution qualities in processing, prevalent wettability for WC, higher dissolvability of WC in cobalt at sintering temperatures and attractive properties [80]. At room temperature, it possesses an hcp structure even as a ferromagnetic metal. However, at 450°C, it changes from hcp to fcc structure. For cemented carbide, W-C-Co compounds are formed with different crystal structures which also possess peculiar properties. Thus, several investigations have been made over the last century to shift from only using classical metallography and X-Ray Diffraction toward combining experimental information with thermochemical descriptions in defining the ternary and equilibrium phase diagrams. In 1931, the first W-C-Co phase diagram was presented [80] as shown in Figure 19. 21 years later, two new carbide phases namely θ and κ, having compositions $Co_3W_6C_2$ and $Co_3W_{10}C_4$, respectively were added on the diagram [82, 83]. A new carbide was also identified in the subsequent years but could not be explained. Almost thirty years later Pollok and Stadelmaier calculated an isothermal section

through the W–C–Co system at 1400 °C, which represents a usual sintering temperature. They identified an eta-carbide of composition Co_2W_4C and a carbide CoW_3C, which was reported early on. The figure also shows that liquid cobalt is also stable with WC in a very narrow region. The solubility of tungsten carbide in cobalt at the sintering temperature is high but decreases during cooling with reprecipitation on existing carbide grains. This preliminary work was followed by an exhaustive review of the thermodynamic properties of alloys and phase equilibria in the W–C–Co system by Guillermet [84], who calculated several isothermal sections of the system through thermodynamic methods. However, tradition and experience are strong tools too and most cemented carbide producers can make high quality cemented carbides without a detailed knowledge of the phase diagrams. This is particularly true for the W–C–Co system which is a very straightforward ideal system for cemented carbides, with a eutectic at 1280 °C which is well below cobalt's melting point of 1490 °C.

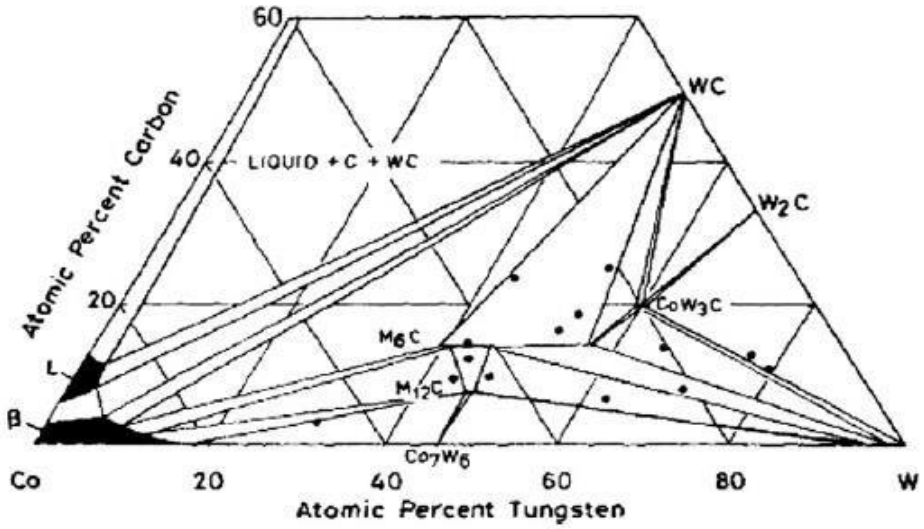

Figure 2-19 : Ternary Phase diagram of the W-C-Co system[80]

2.6.3 Microstructure of WC-Co

The microstructure of materials is noted to have great significance on studying and understanding the properties and engineering performance of the material. Below is a schematic image that describes the different microstructures that have currently been identified with the cemented carbides (Figure 2-20). The different binders that have been used and how the affect the microstructure have also been illustrated. Based on this, a basis for microstructural analysis is done

contingent on the type on microstructure that is present in the sample. Some important factors observed on the microstructure of a cemented carbide are discussed below. These factors hold a direct link to the mechanical properties of the material. They are:

1. *Carbide grain size distributions and mean carbide size*: In determining the carbide grain size, several parameters are used as measures of carbide grain size in planar sections through the material, e.g. grain area or the corresponding equivalent circle diameter (Figure 2-21). The parameters are specific to structures observed on the sample therefore in evaluating the grains, every single observed grain must be measured. A poor sample preparation would make this very difficult to undertake, from electron microscopy and image analysis point of view, especially for materials with both WC and W-C-Co phases. There is always the problem of fully identifying the complete grain boundary network of the grains making it difficult to use some of these advanced and automated image analysis systems confidently. Researchers end up sticking to the basic line intercept method and a semi-automatic image analysis software to determine carbide grain sizes. Even though, intercept length is object specific parameter, manual marking of intercept length will not depend of complete visible network map. Small gaps in the network could be accepted.

2. *Carbide contiguity*: Carbide contiguity is defined as the ratio of carbide/carbide interface area to the total phase boundary area carbide/carbide and carbide/binder in the specimen volume [85], i.e.

$$\mathbf{C} = \frac{Scarb/carb}{Scarb/carb + Scarb/bind} \quad \textbf{(1)}$$

The term gives us an idea of the degree of contact between the carbide grains. On a 2D scale, we can measure this contiguity using:

$$\mathbf{C} = \frac{2Ncarb/carb}{2Ncarb/carb + Ncarb/bind} \quad \textbf{(2)}$$

where $N_{carb/carb}$ and $N_{carb/bind}$ are the number of carbide/carbide and carbide/binder boundaries per unit length of reference line, respectively. In semi-automatic analysis the different types of boundaries are marked during tracking of a reference line grid projected on the structure image.

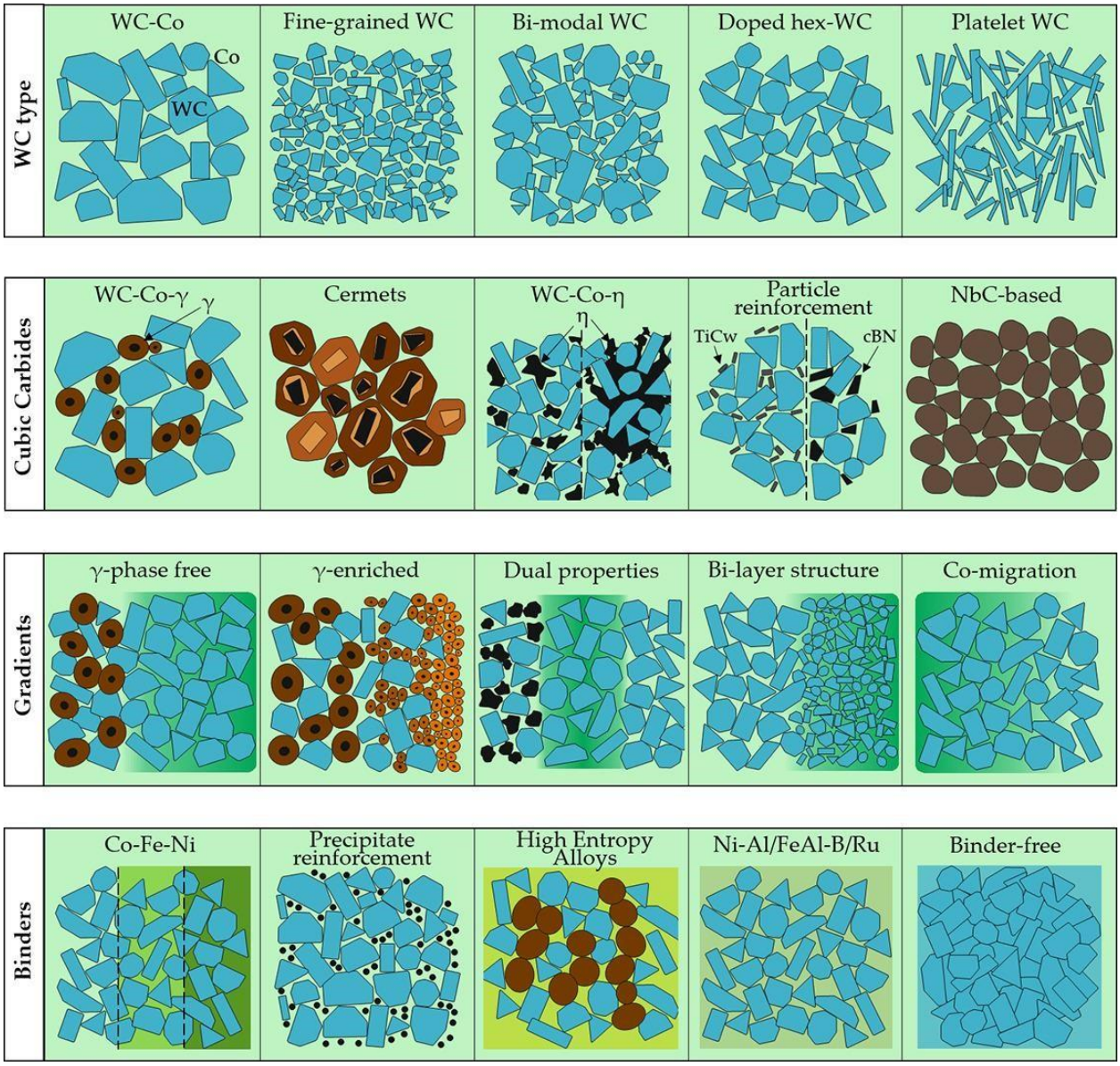

Figure 2-20 : Categorisation of cemented carbide microstructures selected in this work [77]

3. *Binder width distributions and binder mean free path*: For low binder fractions it is conceivable to identify binder pools as individual objects on cleaned cross sections and hence to assess object specific parameters, e.g. binder pool zones. In any case, at high binder fractions the binder shows up as a continuous phase with few individual binder pools.

4. *Volume fractions of various structures identified*: Optical microscopy could be used to ascertain the microstructure in scientific studies for such hard metals with different grain sizes [85]. However, modern grades of cemented carbides have carbide grain sizes that are less than 1um pushing the studies to be done using advanced microscopy. Additionally, industrial grades are known to contain pores, impurities, binder phase regions, and carbide grains that cannot be adequately studied using optical microscopy due to insufficient resolution. This has led to the introduction of the secondary and transmission electron microscopy techniques being used extensively for studying all the above regions as well as an added advantage studying the deformation, fracture behaviour and the nature of precipitates in the binder phase of WC-Co alloys [86, 87].

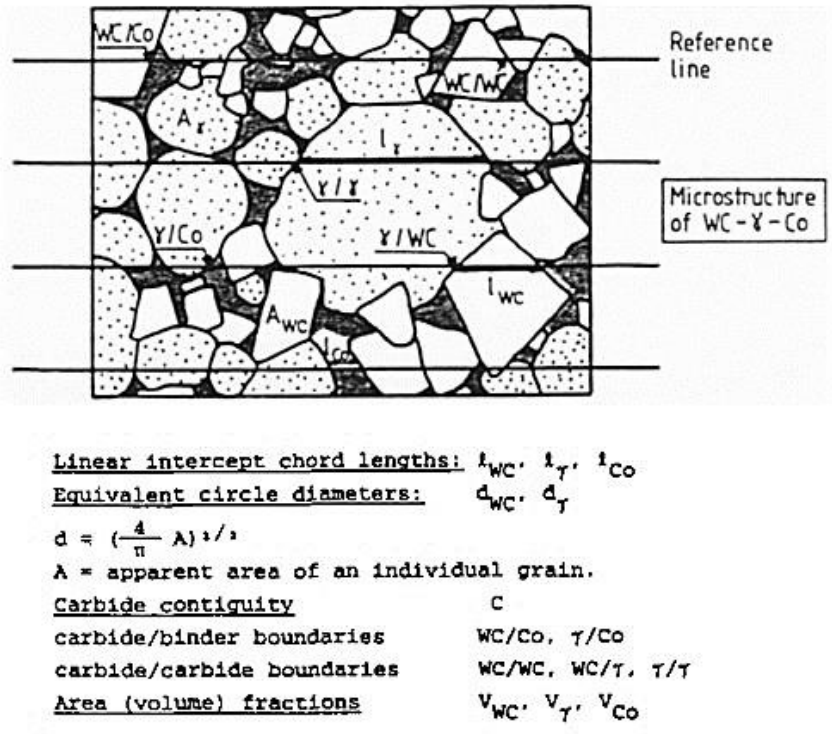

Linear intercept chord lengths: l_{WC}, l_{γ}, l_{Co}
Equivalent circle diameters: d_{WC}, d_{γ}

$d = (\frac{4}{\pi} A)^{1/2}$

A = apparent area of an individual grain.

Carbide contiguity	C
carbide/binder boundaries	WC/Co, γ/Co
carbide/carbide boundaries	WC/WC, WC/γ, γ/γ
Area (volume) fractions	V_{WC}, V_{γ}, V_{Co}

Figure 2-21 : Structural parameters for cemented carbides[80]

2.6.4 Binder Phase

In most cemented carbides, the Co-W-C binder is present as a mixture of fcc and hcp structures. This is because the binder phase is a dilute cobalt alloy containing tungsten and carbon as solutes and can exist in either of two allotropic forms—hcp or fcc. The ratio of the two is determined in bulk alloys by prior processing treatment and composition. The relative ease of interchangeability of the two forms is related to the low stacking fault energy of dilute cobalt alloys. For example, a small parallel array of stacking faults in the fee structure represents a finite amount of hep phase in the form of thin lamella [88]. Zhengi [89], after quenching just after sintering the WC-Co cemented carbide, found the retention of fcc cobalt in contrast to the as sintered structure, which had both fcc and hcp forms. Mixing during milling has significant influence on the distribution of cobalt. Insufficient milling results in a large cobalt pool in the microstructure and may cause porosity. Cobalt distribution is also strongly dependent on carbon content, which seems to control its redistribution during heating to the sintering temperature.

2.6.5 Eta(η) Phase

A third phase which is classified as the name above is also identified in most microstructures. The cause has been attributed to the carbon deficiency in WC-Co alloys during processing. 'Eta' phase is a ternary compound of tungsten, cobalt and carbon. It can exist in two forms, either M_6C carbide ranging from $Co_{32}W_{28}C$ to Co_2W_4C, [90] or $M_{12}C$ carbide of fixed composition Co_6W_6C [91]. Both M_6C and $M_{12}C$ are indistinguishable physically and M_6C may represent a metastable form which can undergo in-situ decomposition (M_6C —> (3 + $M_{12}C$ + WC) by a sluggish reaction [91]. However, in commercial tungsten carbide alloys with a relatively fast cooling rate, presence of M_6C is more probable than that of $M_{12}C$ With minor carbon deficiency levels, η phase is not produced at the sintering temperature but forms on subsequent cooling (i.e., WC + liq. —» WC + T| + liq.), and in doing so occurs as isolated concentrated areas in which considerable volumes of WC and cobalt binder phase are locally consumed during its growth. Rounded partially dissolved WC grains are often associated with such η phase areas. Further cooling into the solidus range can produce peritectic decomposition of this η phase and the final quantity of η phase retained at room temperature is determined by cooling rate and carbon content. The morphologies of the η phase

range from finely dispersed particles at low carbon deficiency to large areas of massive η in highly carbon deficient alloy. If, on the contrary, a cemented carbide with high carbon is produced, free carbon may precipitate as graphite and lower the mechanical properties of the material (Figure 2-22).

2.6.6 Precipitates

Precipitates generally observed in the binder phase of cemented carbides are non-metallic impurities, graphite, carbides, and intermetallic compounds precipitated during cooling or heat treatment in the solid state. According to Gruter [92], in technical WC-Co hard metals, a three-phase region (**η** + WC + liquid) exists, even if the carbon content corresponds to stoichiometric WC. In quenched alloys, this phase retains and lowers the magnetic saturation. But if the alloy is cooled slowly, the **η** phase reacts with the carbon supersaturated in the binder to form WC and Co_3W. Grewe et al. [93] suggest that the eta-carbide W_6Co_6C precipitates from the supersaturated solution after cooling from the sintering temperature initially as Co_2W_4C, which changes composition to the more cobalt rich variations, Co_3W_3C and Co_4W_2C, and finally decays into Co_3W.

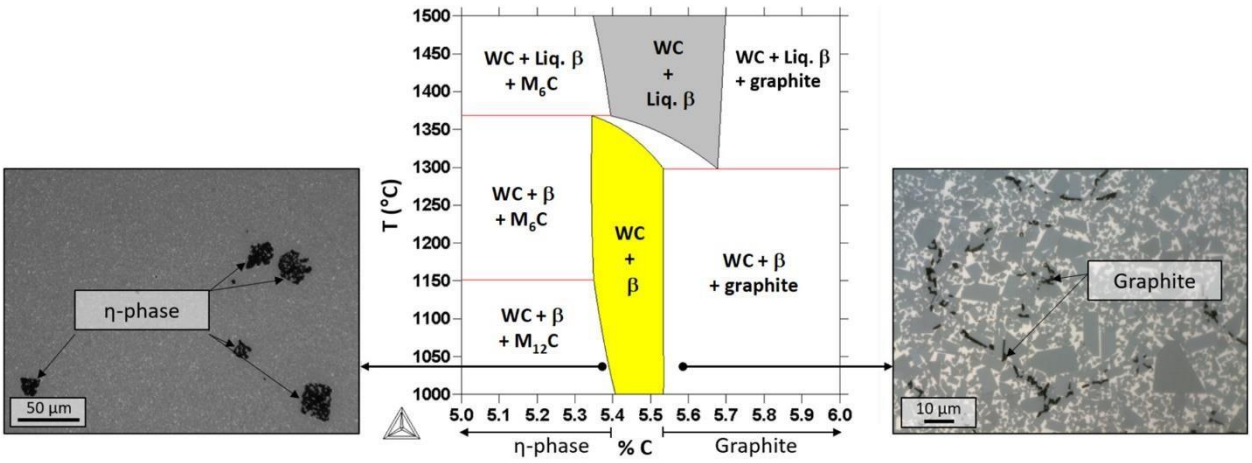

Figure 2-22 : Light optical microscopy pictures showing η-phase (left) and graphite (right) formation on a WC-10%Co cemented carbide. The phase diagram in the centre shows the possible phases. The defect free two-phase region (WC: tungsten carbide, β: Co binder) is highlighted in yellow. Adapted from Ref. [77]

From the phase diagram of W-C-Co system, this intermetallic should not be present at any temperature. Local concentration gradient, however, can arise due to slow diffusion of tungsten in cobalt. It is more likely that the transformation of the cubic into the hexagonal phase is the reason for the formation of the intermetallic due to the sudden decrease of tungsten solubility in the binder phase [93]. Literature [93] is available on the effect of heat treatment on the structure and properties of cemented carbides. The presence of Co_3W simultaneously with hexagonal cobalt modification in heat treated WC-Co alloys has been reported [93]. After heat treatment, hardness increases, but T.R.S. decreases due to the precipitation hardening and the decrease in ductility of the Co_3W containing binder phase [94]. A study of Nishigaki et al. [95] on WC based cemented carbides with Co/Ni/Cr/Al binder suggests that both hardness and toughness of hard metals can be increased by strengthening the binder phase through ɣ precipitation.

2.6.7 Mechanical Properties of WC-Co

Mechanical properties of WC-Co grades have been based on the volume fraction and sizes of individual phases that are present in the material. The major phase which is the WC phase are relatively hard and brittle particles whereas the Co compounds that form with the WC provide a ductile or relatively soft grade. Whereas it is by and large acknowledged that the binder phase is continuous, there's a discussion around the degree of continuity of the carbide phase. One speculation considers that the structure of the sintered WC-Co alloys comprises of scattered carbide particles implanted in a continuous binder phase, with thin binder film isolating the individual carbide particles. Using this speculation, it can be said that, the nature of the binder phase would consequently change the mechanical properties (plastic deformation) of WC-Co alloys. Different authors [95] have attributed the determination of the strength of the alloys to the binder mean free path. However, another speculation rises from looking at the carbide’s matrix. In their case, the plastic deformation of the alloy would require considerable plasticity in the carbide, since the carbide skeleton would have to deform in compatibility with the binder phase.

2.6.7.1 Hardness Behaviour of WC-Co

WC-Co alloys are mainly known for their wear applications because of the high wear resistance they portray. Generally, the characteristic hardness behaviour of a material can be related to it wear performance based on the microstructure. The hardness of the WC-Co is mostly dependent on its average grain size and cobalt contents with minimum variation on the chosen processing route. The smaller the WC grain sizes and cobalt content, the higher the hardness of WC-Co. Figure 2-23 displays the effect of WC grain size and cobalt contents on the hardness of WC-Co material. The microstructural effect on hardness property of WC-Co has widely been studied [96, 97]. The hardness of WC-Co exhibits linear relation with mean carbide grains [98]. Lee and Gurland in their study attributed that carbides particles form partially connected structures with range continuity through direct carbide-carbide contacts within the microstructure of WC-Co which plays significant role on its hardness [98]. Mean while Altmmeyer and Jung in their study reported that hardness of WC-Co, however, exhibit non- linear variation with temperature within a range of (620-700). This effect is attributed to recovery and recrystallisation of Co phases resulting from allotropic transformations. Miyoshi et al. [98] reported a rapid decrease in hardness over the temperature range 300-800 K, whereas, hardness of WC-Co is virtually independent of temperature up to 800 K, and then falls with temperature [98]. It is reported that the high temperature hardness of polycrystalline tungsten carbide is significantly higher than the hardness of single crystal WC in its hardest orientation [99, 100]. Cemented tungsten carbides of fine grain size behave similarly to polycrystalline WC but increasing the amount of binder phase proportionally decreases the hardness [100]. The high hardness of fine-grained WC in the temperature range from 300-1100 K has been attributed to the Hall-Petch effect [109]. On the other hand, some cemented carbides with large WC grains lose hardness very rapidly with increasing temperature, behaving very similarly to the hardness of single crystal WC [108]. Additionally, TaC and TiC and tungsten is added to the binder phase of WC-Co to form a composite to increase resistance of WC-Co to plastic deformation and the rate of strength loss with increasing temperature. This increases ultrafine grain cemented carbides and gives the composite its ability to resist cutting edge deformation [102]. Therefore, the wear resistance and hardness of tool materials are improved.

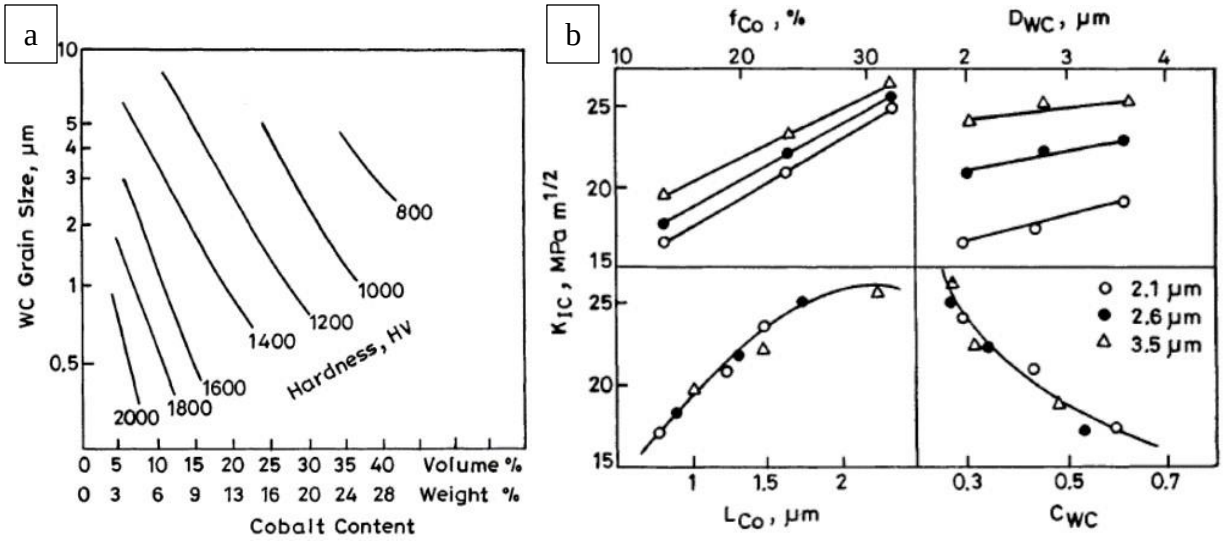

Figure 2-23 : a) A graph of WC grain size against the cobalt content showing the increase in hardness with increasing grain sizes b) Fracture toughness (KIC) as the function of microstructural parameters and volume fraction of cobalt binder for WC-Co cemented carbide prepared from different size WC powders [101].

2.6.7.2 Fracture Toughness

Fracture toughness behaviour of WC-Co materials is an important tool that guides the development of new carbide grades and offers the understanding of the mechanisms of the effect of cubic carbide phase additions on the properties of cemented carbides. Fracture toughness gives a measure of materials resistance crack propagation with respect to it maximum energy absorption before failure. In WC-Co materials, fracture toughness increases with increase in the above-mentioned parameters except for the carbide contiguity parameters which reduces toughness as it increases. The toughness also relies strongly on carbon stoichiometry. The WC-Co becomes detrimental with reduced fracture toughness when the carbon content is deficient or in excess. The influence by the latter is somewhat lesser than the former due to improvements in carbide grain size and binder phase distribution which is brought about by increased binder phase fluidity due to excess carbon [101]. For hard metals such as WC-Co, fracture toughness measurement becomes difficult to compute due to difficulty in creating a pre-crack. Due to this, the fracture toughness of WC-Co hard metals is carried out at elevated temperatures [102, 103]. However, it is reported that the material exhibits not much significant change in toughness up to 600 ^{o}C [102, 103]. For mixed carbide grades of TiC and (Ta, Nb) C, the fracture toughness maybe improved at about 700 ^{o}C.

This is attributed to increase local plastic zone size at the crack tip resulting from the hexagonal to cubic phase transformation in the cobalt phase. Also, rapid decrease in hot hardness of WC [108], crack healing and blunting increases the plasticity of WC materials [112].

2.6.7.3 Wear Behaviour of Cemented Carbides

For cemented carbides several different mechanisms account for the wear behaviour. These underlining mechanisms may vary with service conditions and with the composition and microstructure of the alloy. The main mechanisms are not limited to brittle fracture, fatigue, and plastic deformation as a result of corrosion and diffusion from the materials microstructure and phases compositions [104]. Generally, the wear mechanism includes abrasive, attrition and diffusional wear.

Abrasive wear, prevalent wear mode generally occurs when hard particles rub across contacting surfaces mostly during metal cutting. This kind mechanism occurs when the hardness of the tool material and the workpiece is comparatively similar with regards to compositions and structural features that controls hardness. For cemented carbides, it is generally known that the precise mechanism of abrasive wear depends on the hardness of the abrasive particles relative to the bulk hardness [104-106]. Material loss by either plastic deformation or brittle spall formation has the tendency to cause carbides grains fragmentation on extruded WC surfaces when the abrasive particles are harder than the WC. On the other hand, carbide grains are slightly displaced with gradual cobalt binder extrusions when soft counter abrasive particles slide over with substantial frictional forces. This results into carbide fragmentation as a result of carbide and binder contraction during cooling process. Nonetheless, regardless of the nature of the counter abrasive particles, the binder phases between WC grains maybe extruded under the actions of high local stresses. Peters et al. [107] reported that abrasive wear of WC-increases as the fracture toughness of the hard metal increases. Abrasion resistance decreases with increasing cobalt content. However, although hardness decreases with increasing cobalt content of WC materials, the finer the carbide at a given cobalt content, the harder the WC-Co grade. Reznik [108] proposed that wear rate of cemented carbide is proportional to the ratio between crack extension force and critical density of potential energy of elastic deformation. In order to increase the abrasive wear resistance,

carbide inclusions such as tantalum, titanium and niobium carbides can be added to the alloys composition to inhibit grain growths, increase high temperature resistance to deformation and decrease the coefficient of friction respectively between the WC-Co and tool. This practice improves the abrasion resistance within substantial limits as shown in Figure 2-24 [109].

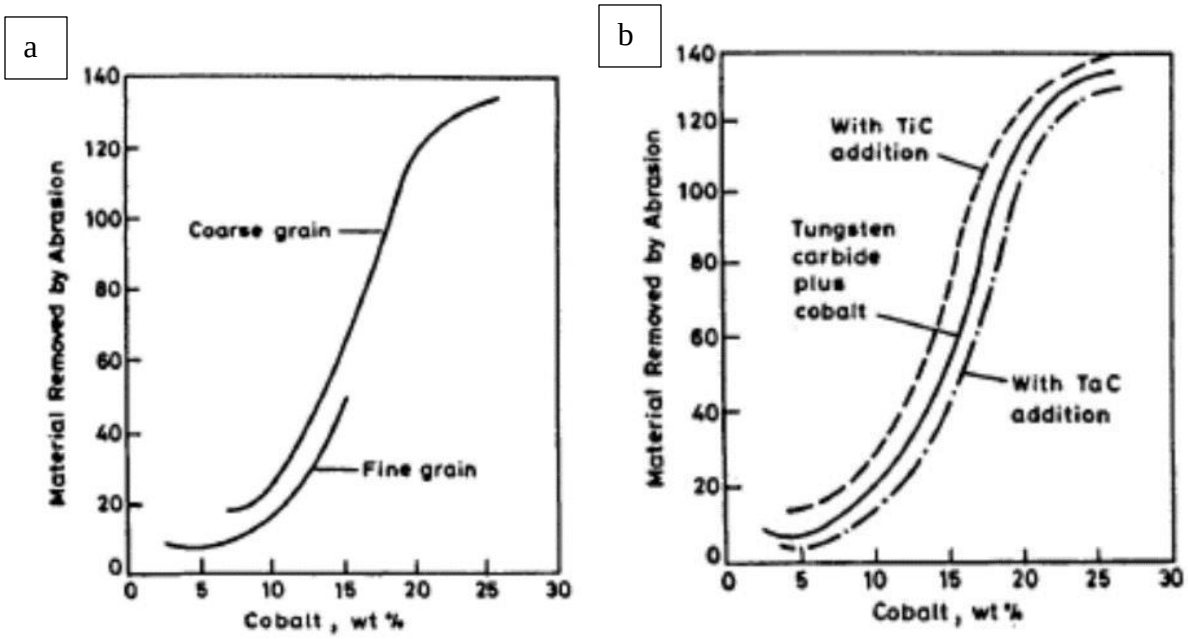

Figure 2-24 : a) Abrasion resistance of WC-Co hard metals as a function of cobalt content .b) Effect of titanium carbide and tantalum carbide additions on abrasion resistance of WC-Co hard metals.

Attrition wear is an adhesive wear mechanism that result from cold welding effect in metal cutting, especially at low surface speeds. The wear rate is associated with grain size rather than hardness. In WC-Co, complete WC grains are plucked away with this kind of wear. Figure 2-25 shows the grain size dependence on the wear behaviour. Usually, grain growth inhibitors such as TaC, TiC, NbC, VC etc. are used to control the wear effect but the amount of additions leaves much to be desired of as they could have adverse effect on the strength of the material.

Diffusion wear is a wear mechanism occurring due to diffusion of carbon from the cemented carbide to the steel chip sliding over the rake face of the insert [109]. This process is referred to as cratering. This depends upon the solubility of tool material in the work material and the interface temperature obtained during cutting. Similarly, TiC addition to WC-Co cemented carbides is made to minimize this wear effect. TiC's produce TiC-WC solid solution which are of high hardness

and chemical and temperatures stability imparts an excellent resistance to crater wear. It also increases crater resistance by reducing carbon diffusion from carbide tool to the steel chip.

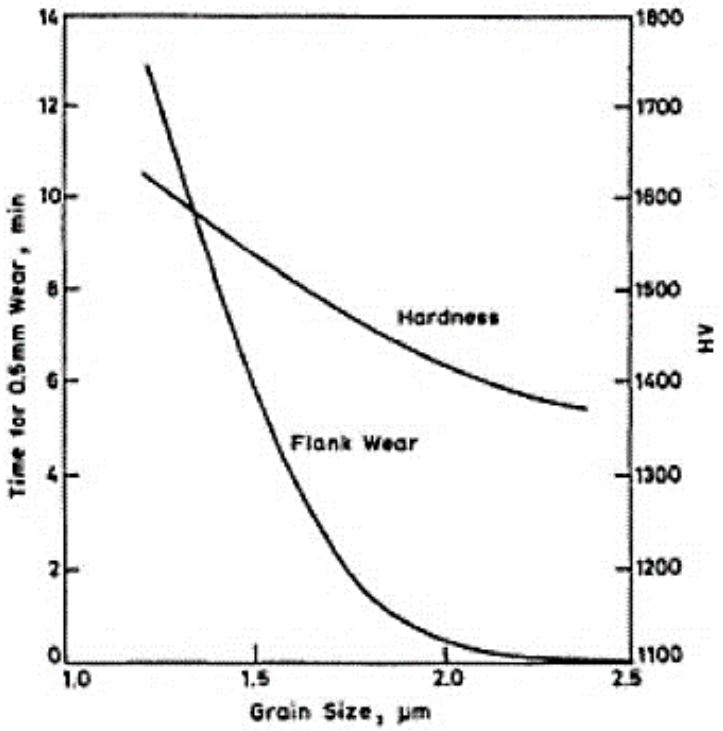

Figure 2-25 : Effect of grain size and hardness on flank wear rate for WC-6% Co when machining cast iron at 0.5 m/s.

2.7 Scope and Objectives for Study

Using the PBF process such as Direct metal laser sintering (DMLS), Electron beam melting (EBM), Selective heat sintering (SHS), Selective laser melting (SLM) and Selective laser sintering (SLS) require specially prepared powders, printing parameters (process control) and postprocessing treatments that will optimize the microstructural integrity and mechanical properties of printed parts [110]. Cemented carbides such as tungsten carbide (WC), Titanium Carbide (TiC) or Tantalum Carbide (TaC), which are generally processed using the conventional powder metallurgy route, have not benefited much from the PBF process due to the lack of commercially available powders as well as myriad of defects in printed parts [111]. Considering this, efforts have been made in printing cemented carbides using ink jet printing or binder jet-based

printing techniques [112, 113]. However, these processes require extensive post-processing (oven treatment) to remove the binder and subsequently to infiltrate porous parts for increasing densification. These processes compromise the strength, size and design of manufactured parts. Currently, there are studies aimed at understanding the relationship between microstructural integrity/properties and powder compositions and printing parameters (process control) of cemented carbides such as WC-Co [114–121]. For example, Kumar processed tungsten-carbide cobalt (WC–9 wt.% Co) by combining the material properties of a composite with the flexibility of the SLS process and infiltrated the laser sintered parts with bronze to improve their mechanical properties [121]. Additionally, Gu et al fabricated WC-Co parts using various composition of powders comprising 18 wt. % to 45 wt. % WC using Cu as a binder in order to understand the effect of the different powder compositions on the production process and integrity of printed parts [117–120]. Gu and Meiners used SLM to process W–Ni–graphite elemental powder mixture to prepare bulk-form in situ WC-based hard metals and characterized the microstructure and mechanical properties of the produced parts including the mechanisms that resulted in the evolved structures [116].

In all these studies, it has been demonstrated that PBF processes such as SLS and SLM have complex mechanisms that occur during manufacturing of parts including multiple modes of heat, mass, and momentum transfers induced by localized laser scanning. This results in processing defects such as gas entrapment, aggregation of constituent phases, microcracks and nonequilibrium phases that affect the integrity of the microstructure and properties of processed parts [115]. For example, Khymrov et al demonstrated that crack-free WC-Co cemented carbides can be processed by using small volumes of WC during 3D printing of WC-Co cemented carbides [114]. They processed crack-free WC-Co parts by using a lower percentage of the WC powder (25%) which in turn affected the mechanical properties of the processed cemented carbides. When they increased the amount of WC to 50%, the processed structure had significant quantities of both micro and macro cracks [114]. Uhlmann et al processed 83%WC-17%Co parts comprising of cooling channels but observed that the produced parts were riddled with fine micro-cracks [122]. Kumar and Czekanski processed complex WC-Co parts consisting of various micro-features such as thin walls tilted at various angles, cylindrical pins and holes of various diameters [3, 123]. However, these parts were not free from cracks and pores which was attributed to the percentage of WC used.

For most applications, Tungsten mono-carbide (WC) is the desired phase; however, due to the irregular thermal cycles involved in both conventional powder metallurgy route and metal additive manufacturing processes, WC phases are usually converted to other secondary phases (W_2C, WC-Co phases). It has been shown that W_4Co_2C, W_3Co_3C and W_6Co_6C are the most important inevitable phases when processing WC-Co cemented carbides [124]. It has been reported in several studies that post-processing heat treatment could beneficially modify the properties of PBF processed materials as well as relieve residual stresses created by processing conditions. Zhou et al characterized the microstructure and mechanical properties of an SLM printed Maraging steel and asserted from their findings that heat treatment does not induce strengthening alone but also significantly relieve residual stresses and eliminate mechanical anisotropy [124]. Maraging steel has been a close competitor for the WC-Co alloys on the commercial market even though there are application-specific demands for the two different materials. There has not been much work done to understand how post-processing affects the microstructure and properties of PBF processed WC-Co alloys. It is reported that at the eutectic temperature, about 12% of tungsten carbide is dissolved in cobalt of cemented carbides. As temperature decreases, the solubility drops substantially and at 800-600 °C, amounts up to 1% [125]. This fact that solubility of the tungsten carbide decreases with decreasing temperature provides another basis for changing the properties of WC-Co alloys by annealing heat treatment in order to form more of the desired Tungsten monocarbide (WC). Tumanov et al studied the effect of rate of cooling of Tungsten Carbide-Cobalt alloys on the composition of the cementing phases [126]. The composition of the cementing phase is practically independent of the rate of cooling [126]. WC-Co alloys are used as coating more often because of their wear properties and some studies using heat treatment have been done to optimize these properties. Asl et al studied a WC-Co coating deposited onto ST37mild steel substrate using HVOF spray technique and then heat treated at different temperatures in a vacuum chamber [127]. They revealed that some brittle eta (η) phases were produced at high-temperature heat treatments. Generation of these brittle eta (η) phases increased the coating's hardness and decreased fracture toughness of the coating [127]. Stewart et al also used WC–17 wt.% Co powders to form coatings on steel substrates and heat treated at a range of temperatures between 250 °C and 1100 °C [128]. They demonstrated that there was an improvement in the abrasive wear properties of the coating. Also, heat treatment above 600 °C resulted in significant phase changes within the coating. However, heat treatment at all the temperatures examined resulted in changes

in the microstructural integrity and residual stress state of the coating [128]. Other studies performed these heat treatments at temperatures below 1000 °C and reported drastic changes in the mechanical and microstructural properties of the cemented carbides [129, 130]. Thus, postprocessing heat treatment of WC-Co can increase the effective carbide content (with higher hardness and wear resistance) and improve the structure and properties of the alloy.

Hexagonal Boron Nitride(hBN) is known to possess a crystal structure like that of graphite and therefore has a low thermal expansion coefficient, a high thermal conductivity and a high resistance to thermal shock and corrosion. It is sometimes known as a high temperature material. It is even more attractive as an additive for machining tools because of its lubricative properties. The hBN exists as one of several crystalline varieties having the two sp2-bonded layered configurations in AB stacking among the BN allotropes including cubic BN (c-BN) analogous to diamond, wurtzite BN (w-BN) similar to the lonsdaleite, and rhombohedral BN (r-BN) in ABC stacking corresponding to r-graphite whiles hBN corresponds to h-graphite [131].

There exist studies on alloy design of WC-Co with cBN inclusions using conventional manufacturing techniques. This was to help improve bonding or mechanical properties of the material. Yaman and Hasan [132] compared the wear performance of a WC-6Co, WC-6Co-(25%vol)cBN. They processed both materials using novel spark plasma sintering. They concluded that the addition of cBN enhanced the wear properties of the material as compared a WC-6Co. Additionally, the revealed that there is a possibility to study the potential of adding BN material to WC-Co for enhanced wear and other mechanical properties. Rong et al fabricated using spark plasma sintering a cBN/WC-Co composite [133]. His new composite exhibited higher hardness and fracture toughness. Martinez and Echeberria [134] also achieved an increase in higher hardness and fracture toughness by processing a WC-Co with 50%vol of cBN. They used hot isostatic pressing to fabricate it. The also added that there was no phase transformation from cBN to hBN.] However, they had inhomogeneous and rapid grain growth which was degrading for the microstructure of the sample. In additive manufacturing, irregular heat and cooling creates an unstable microstructure after printing. Thus, the need to adopt a post processing treatment to relieve the built-up residual stresses and unstable phases. There is no attempt to process WC-Co-cBN using additive manufacturing because of the brittle nature and high melting point of its constituents. However, the properties of hBN can be implored to help fabricate a cemented carbide whereby a reduction in thermal shock can occur thereby fabricating a material with very few

microcracks. A further one step heat treatment process can be employed to help reduce residual stresses in the material and improve its mechanical properties. Yet still, there is also the need to reduce the rate of microcracks by introducing the hBN which will reduce the effect of thermal shock on the sample during printing. Thus, the need to study effect of post-processing heat treatment on the microstructure and properties of SLS printed WC-Co-hBN alloy is very understandable in order to determine the conditions for optimizing the structural integrity and properties of the 3D printed alloy.

The goal of this study is to understand the effect of post-processing heat treatment on the microstructure and properties of SLS printed WC-Co alloy in order to determine the conditions for optimizing the structural integrity and properties of the 3D printed alloy. Further to this main objective, the following are detailed objectives completed towards fulfilling this main objective:

1. Assess the microstructural and mechanical properties of an as-printed WC-Co alloy.
2. Perform post processing heat treatments on the as-printed WC-Co alloy and study the microstructural evolution and characterize the mechanical properties (hardness, fracture toughness and wear).
3. Successfully fabricate a new cemented carbide with self lubricating properties
4. Assess the microstructural and mechanical properties of the new cemented carbide with self lubricating properties.
5. Perform post processing heat treatments on the as-printed cemented carbide with self lubricating properties and study the microstructural evolution and characterize the mechanical properties (hardness, fracture toughness and wear).

CHAPTER 3: MATERIAL AND EXPERIMENTAL PROCEDURE

3.1 Introduction

In this research, it is proposed that due to the challenges present in the as-printed material, a systematic study of the microstructure of the as-printed sample and the as-printed samples after post processing can be used to track the microstructural changes that occur during the post processing process. Additionally, the analysis of the mechanical properties can also be tracked likewise, and data can be used to design a self lubricative alloy with better mechanical properties for wear applications be adopted. Thus, the objectives of this research are to study the microstructure and assess mechanical properties of the as printed and post-processed WC-Co samples as well as the as-printed and post processed WC-Co-hBN samples to determine the effect of post processing heat treatment on 3D printed materials and improve the wear properties of the cemented carbide by addition of a self lubricating material. The process to achieve the objectives of this study is grouped into three major parts:

- First, an initial assessment of the as-printed WC-Co material followed by a comprehensive microstructural characterization and mechanical property measurements of heat-treated samples as compared to the as-printed sample.

- Secondly, a comprehensive redesign of an alloy comprising of WC-Co and hBN and a successful 3D print of a consolidated sample for analysis will be done.

- Thirdly, the printed WC-Co-hBN sample is assessed and post processed using heat treatment to track the microstructural evolution and mechanical properties of the heat-treated samples in comparison to the as printed sample. Additionally, it shall be compared with the WC-Co material to assert its advantages with the hBN inclusions.

3.2 Material Processing and Sample Preparation

WC-Co powder which is already pre-alloyed was acquired from Buffalo Tungsten Inc., USA. The powder was composed of 83wt.% WC and 17 wt.% Co. For the WC-Co-hBN sample, a mixture of hBN powder and WC-17%Co was prepared. In processing, an EOS M280 which has been approved for processing customized powders was adopted for processing the materials. A precautionary measure was taken by performing the printing in a nitrogen environment in the build chamber of the machine. This was done to avoid unwanted burning and oxidation during the printing. A substrate made of 1045 cold rolled steel was used. This was adopted because it would help to effectively fuse the printed part unto a suitable substrate. Using optimized printed parameters stated in a previous study, WC-Co samples were processed and used for the research study. Table 2 lists the parameters used and adopted for the processing of the cemented powders [3]. For the WC-Co-hBN samples, a parametric study using the same EOS M280 machine was done to ascertain the volume of hBN and appropriate printing parameters that would print a consolidated WC-Co-hBN sample. A successful print was made at 3% volume of hBN powder mixed with the WC-Co. In both processes, the AM system was equipped with a heater which heated the processing environment and the substrate up to 200 °C before processing the powders began. These conditions were used to print samples of 5 mm thickness and a size of 20 mm x 50mm. The fabricated blocks were sectioned using wire EDM prior to heat treatment.

Table 2 : Printing parameters adopted for processing WC-17Co and WC-Co-hBN on the EOS M280 machine.

Parameter Value	**Value**
Laser Power	270W
Scan Speed	500mm/s
Beam diameter	0.1mm
Hatching Distance	0.4mm
Layer thickness	0.04mm
Preheating	200 °C

Table 3: Chemical Composition of Materials for study (WC-17Co & WC-Co-hBN)

Product Name	WCT-17Co (Conventional WC)
Description	Agglomerated and Sintered
Chemical Composition (WC-17Co)	Co = 15 – 18% C = 4.8 – 5.6% W = Balance
Chemical Composition (WC-Co-hBN)	Co = 15 – 18%
	C = 4.8 – 5.6% hBN = 3% vol W = Balance
Particle Size	-53 +20 micron -45 +15 micron -30 +5 micron
Apparent Density	4.3g/cc minimum

3.3 Heat Treatment and Microstructural Characterization of Both WC-17Co & WC-Co-hBN Alloys

Four sectioned samples of each printed alloy were heated-treated in a furnace at 400 °C, 600 °C, 800 °C and 1000 °C for 3 hours respectively. The furnace was set at a constant heating for all the samples. After the 3 hours hold time, the samples were then cooled to room temperature in the furnace. This was done by setting the furnace to 250°C after the 3 hours hold time. One of the sectioned samples of each alloy did not undergo this heat treatment process in order to serve as the baseline for comparison to their corresponding heat-treated samples. The samples were then named as A400 °C, A600 °C, A800 °C and A1000 °C for the WC-Co alloy and B400 °C, B600 °C, B800 °C and B1000 °C for the WC-Co-hBN alloy respectively. The samples without heat treatment is referred to as the as-printed WC-Co and the as-printed WC-Co-hBN samples. A schematic diagram of the heat treatment process for all the samples have been shown in Figure 3-1. After heat treatment, all the samples were then cold mounted using epoxy resin. This was done

without compromising the structure and composition of the samples. The mounted samples were prepared using piano flexible diamond disks with 5 different grades (80, 120, 240, 600 and 1200). During grinding, a maximum of 10 minutes was spent on each flexible diamond disk to obtain a smooth surface. This was followed by polishing of the samples using monocrystalline diamond suspension (1 um, 0.5 um and 0.25 um) to obtain a mirror surface finish. An optical photograph of both the WC-Co samples and the WC-Co-hBN samples have been shown in Figure as A: and B: The samples used in this study were not etched.

The microstructure of these polished samples was characterized using a scanning electron microscope (TESCAN VEGA 3) equipped with an energy dispersive spectroscopy (EDS) detector which was used to assess the chemical elements present in the samples.

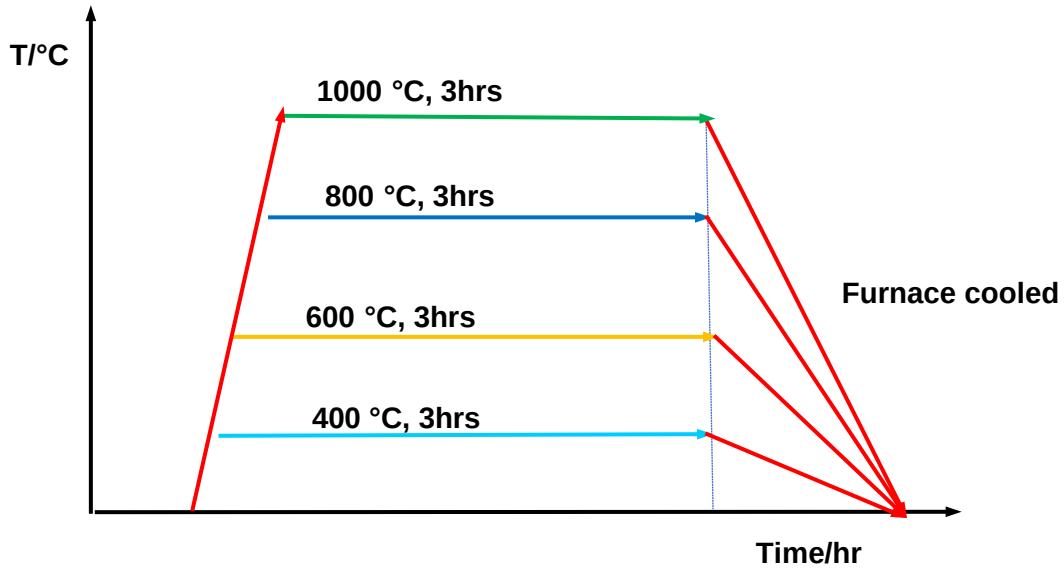

Figure 3-1 : Schematic diagram of heat treatment procedure used for the WC-17Co and WC-Co-hBN materials after processing using SLS.

3.4 X-Ray Diffraction (XRD)

In order to determine phase evolution and crystallographic characteristics after processing and heat treatment, X-Ray Diffraction was carried out using the Philips XRD system. The XRD was operated at 35 kV and 20 mA with a scanning rate of 3° 2θ/min. The analysis was done using MDI Jade software which involved the identification of the phases. Two scans for the same sample were

analysed together and the noise was removed on each pattern as a common practice for X-Ray diffraction analyses.

3.5 Wear Experiments

Wear tests were done using a Bruker UMT Tribolab. The mass of the sample before and after wear test was measures to determine wear loss using a high precision mechanical weighing balance. Using an alumina ball as counter body, the samples was oscillated on a linear axis terming it as a reciprocating wear test (Figure 3-3). In order to maintain elastic constant conditions at the interface, Hertzian pressure (P) was calculated for the applied load (20 N) as per equation (2) given below:

$$\mathbf{P} = \frac{\mathbf{F}}{\pi \mathbf{a}^2} \qquad \mathbf{a} = \left(\frac{3\mathbf{FR}}{4\mathbf{E}}\right)^{\frac{1}{3}} \qquad \frac{\mathbf{1}}{\mathbf{E}} = \frac{\mathbf{1}-(\upsilon_1)^2}{\mathbf{E_1}} + \frac{\mathbf{1}-(\upsilon_2)^2}{\mathbf{E_2}} \qquad \mathbf{P_0} = \frac{\mathbf{3}}{\mathbf{2}}\mathbf{P} \qquad \mathbf{(3)}$$

Where F is the applied load in Newtons, R is the diameter of the alumina ball in meters. E1, E2, ν1, ν2 are Young's modulus and Poisson's ratio of ball and sample (WC-Co) respectively. P0 is the maximum Hertzian pressure at the centre of the interface. The values used for E1, E2, ν1, ν2, minimum values found in the literature for WC-Co processed by conventional means were taken. This was done to ensure that the Hertzian pressure calculated would be far below the estimated yield strength of the samples [135, 136]. Equations gave P_0 as 1268 MPa which is far below the yield strength 2000 MPa. This validated the tests conditions not to change to plastic contact conditions. A commercial 3D printed Maraging steel (MS1) supplied by EOS was adopted as a comparison for the wear properties [137].

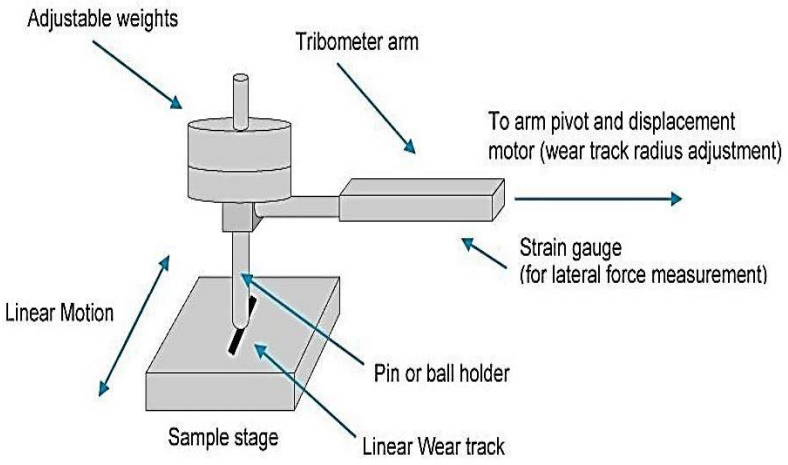

Figure 3-2 : Schematic diagram of the wear experiment

3.6 Microhardness

Microhardness measurements were performed on the polished samples with a digital microhardness machine by applying a 300 gram-force (2.942N) for 15 seconds. A total of 25 hardness values (VHN) were recorded and their average values calculated as the hardness value of the sample (Figure 3-4).

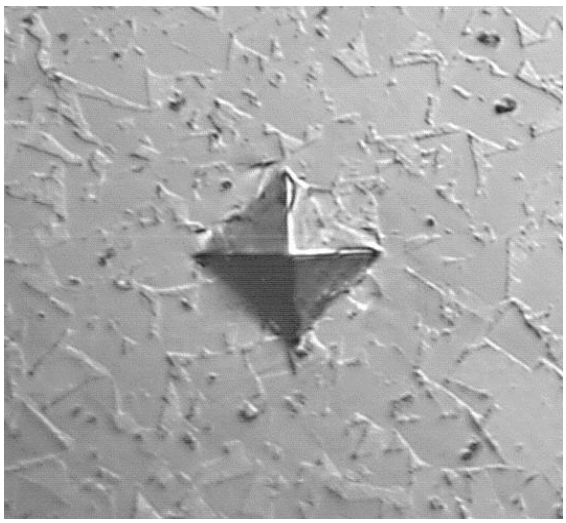

Figure 3-3 : Optical image of a WC-Co material indented using a Micro Vickers Indenter.

3.7 Fracture Toughness

Fracture toughness tests were also performed on the samples using the indentation approach. Using increasing loads method, 30 Kgf was selected to perform tests at selected areas where there were no pre-existing cracks on the surface of samples. Tests that produced either no cracks or more than four cracks were discarded. Fracture toughness was determined using the following equation proposed by Shetty et al for WC-Co materials [138, 139].

$$\mathbf{K_{IC} = 0.00889 \times \sqrt{\times H \times g^2 \times \frac{M}{L_{Tot}}}}$$

$$\mathbf{L_{Tot} = L_1 + L_2 + L_3 + L_4} \qquad \textbf{(4)}$$

Where Kic is the fracture toughness in MPa√m, H is the hardness (HV30/HV50), L_{Tot} is the sum of crack lengths in mm, M is the applied load in newtons g is the acceleration due to the gravity (9.81 m/s^2).

4: RESULTS

4.1 Microstructural Evolution After 3d Printing and Heat Treatment Of WC-Co Alloys

4.1.1 Microstructural Evolution of The As-Printed WC-Co Sample

Figure 4-1 shows scanning electron micrographs describing the microstructural features and structure of the as-printed sample. Generally, four distinct microstructural features were observed within the as-printed sample. This includes irregular and regular polyangular chips, dendritic structures,

"foggy" (shapeless) regions and dark background regions. Figure 4-1(a) shows the regular and irregular polyangular chips observed on the as-printed sample. Typically, the sizes of the regular polyangular chips were relatively small when compared to the irregular polyangular chips. In addition, the surfaces of the regular polyangular chips appeared to be relatively smooth with no strips or stringers while the irregular polyangular chips had thin dark stringers on them as shown in Fig 4-1(b). In Figure 4-1(c), regions occupied by well-developed dendritic structures were observed on top of the dark background regions. Also, well-defined and distinct chips were observed in some regions in addition to regions with non-distinct chips as shown in Figure 4-1(d). Furthermore, some regions of the sample had agglomerations of tiny chips as shown in Figure 4-1(e). These agglomerations of tiny chips were usually observed around the "foggy" regions. The observed "foggy" regions were located at different areas of the sample occupying about 40% of the volume fraction after image processing and calculations (Figure 4-1(a, b, g)). Clusters of dark spots (micro pores) were usually observed on the "foggy" regions as shown in Figure 29(h). Besides the pores, micro-cracks were also observed in the as-printed sample (Figure 4-1(g, h)). These micro-cracks had branches of cracks with clusters of pores around them as shown in Figure 4-1(h).

Figure 4-2 shows results from EDS analysis and X-Ray diffraction for the as-printed sample. This was done to ascertain the chemical elements of the various structures and regions observed in the sample as well as the phases present. The chemical mapping analysis done on the regular and irregular chips revealed W and C as the dominant elements as shown in Figure 4-2(a-e). Thus, the observed regular and irregular polyangular chips are WC chips. The observed tiny stringers on the irregular polyangular chips were identified as Co stringers (Figure 4-2(d)). Additionally, the

“foggy” regions had W, C and Co, thus, a WC-Co structure while the dark background regions were rich in cobalt as shown in Figure 4-2(d). The X-ray Diffraction (XRD) analysis, as shown in Figure 4-2 (f), showed that the as-printed specimen was made up of W_3Co_3C, W_2Co_4C, W_2C and the hexagonal WC phases.

4.1.2 Microstructural Evolution of the Heat-Treated Sample (A400 °C)

Figure 4-3 depicts scanning electron micrographs that describe the evolution of the microstructure of the printed WC-Co sample after heat-treatment at 400 °C for 3 hrs. Generally, the same microstructural features observed in the as-printed sample, namely irregular and regular polyangular WC chips, dendritic structures, “foggy” (shapeless) regions and dark background regions, were observed in this sample with slight variations in the morphology and distribution of these structures. The regular and irregular polyangular WC chips appeared to be well-developed and distinct when compared with those observed in the as printed. However, they were smaller with evidently more regular polyangular chips as shown in Figure 4-3(a). The agglomerated WC chips around the W-C-Co phase also became well-developed and distinct as shown in Figure 4-3(b). The relative size and distribution of most of the W-C-Co phase were reduced when compared to those found in the as-printed sample as shown in Figure 4-3(c). Also, fewer stringers were observed on the irregular polyangular WC chips as shown in Figure 4-3(d). The observed dendritic structures appeared thicker and more distinct (Figure 4-3(e)) on the cobalt-rich backgrounds. Precipitates were observed in some cobalt-rich regions as shown in Figure 4-3(f) which was not observed in the as-printed sample.

Pores were observed on the relatively large W-C-Co phase (Figure 4-3 ((b), (d) and (g)). Thicker and more straight micro-cracks stem and fewer micro-crack branches were observed as shown in Figure 4-3(h).

The EDS maps from the sample showed that the distinct polyangular chips were rich in W and C while the dendritic structures were rich in both W, C and Co (Figure 4-4(a)-(e)). The dark background was predominantly Co. From Figure 4-4(f), which depicts the X-ray diffraction patterns of the heat-treated sample at 400 °C, there is no new phase seen in the sample with respect to the as-printed sample. However, no W_2Co_4C was identified in this sample even though it was present in the as printed sample. In addition, there were significant reductions in the peak heights

of the WC and W_2C as compared to the as-printed sample. Nevertheless, the observed peak heights of the W_3Co_3C phase increased when compared to the as-printed sample.

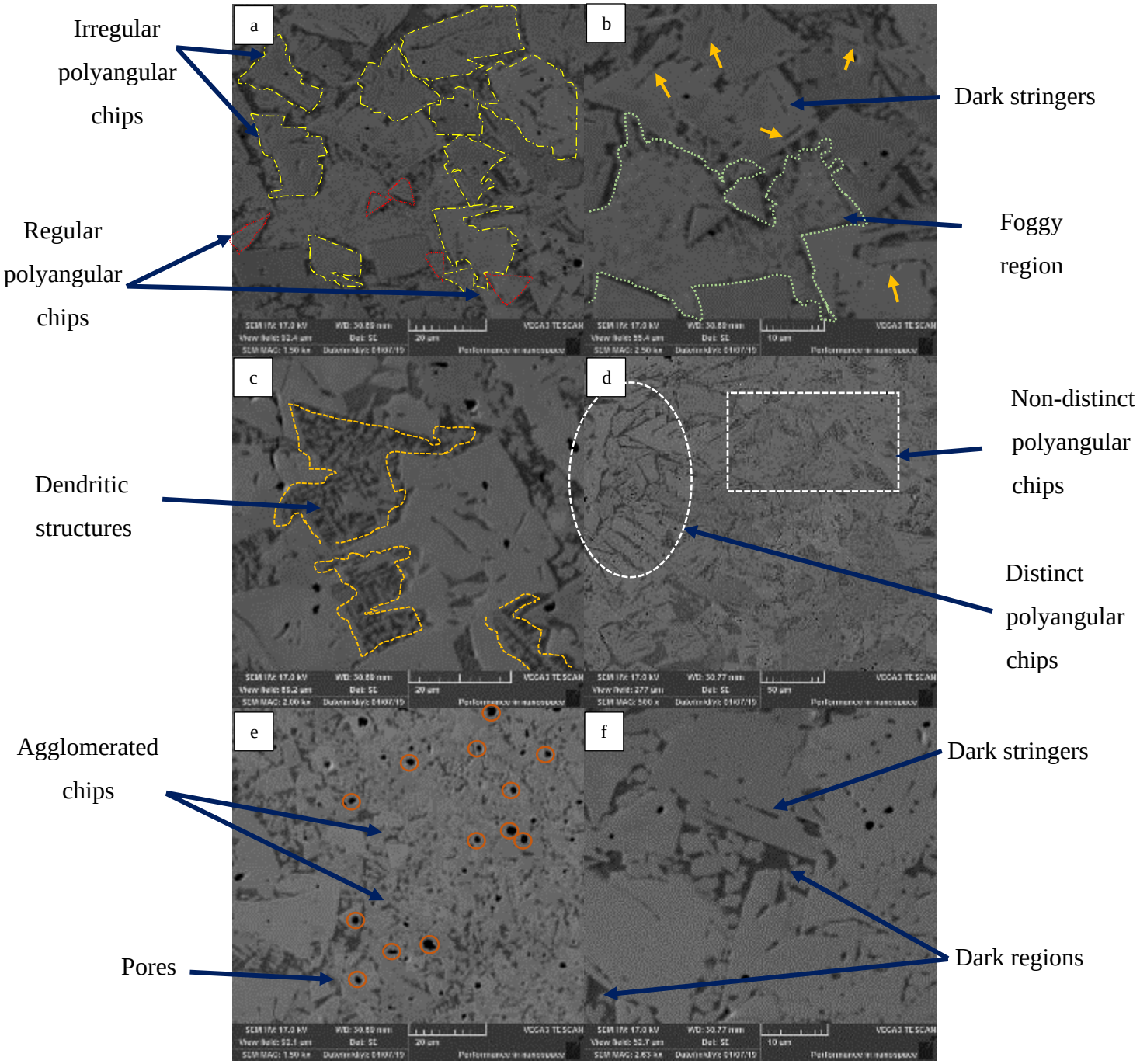

Figure 4-1 : Scanning Electron micrographs for as-printed sample describing the microstructural features and discontinuities identified as a result of processing technique.

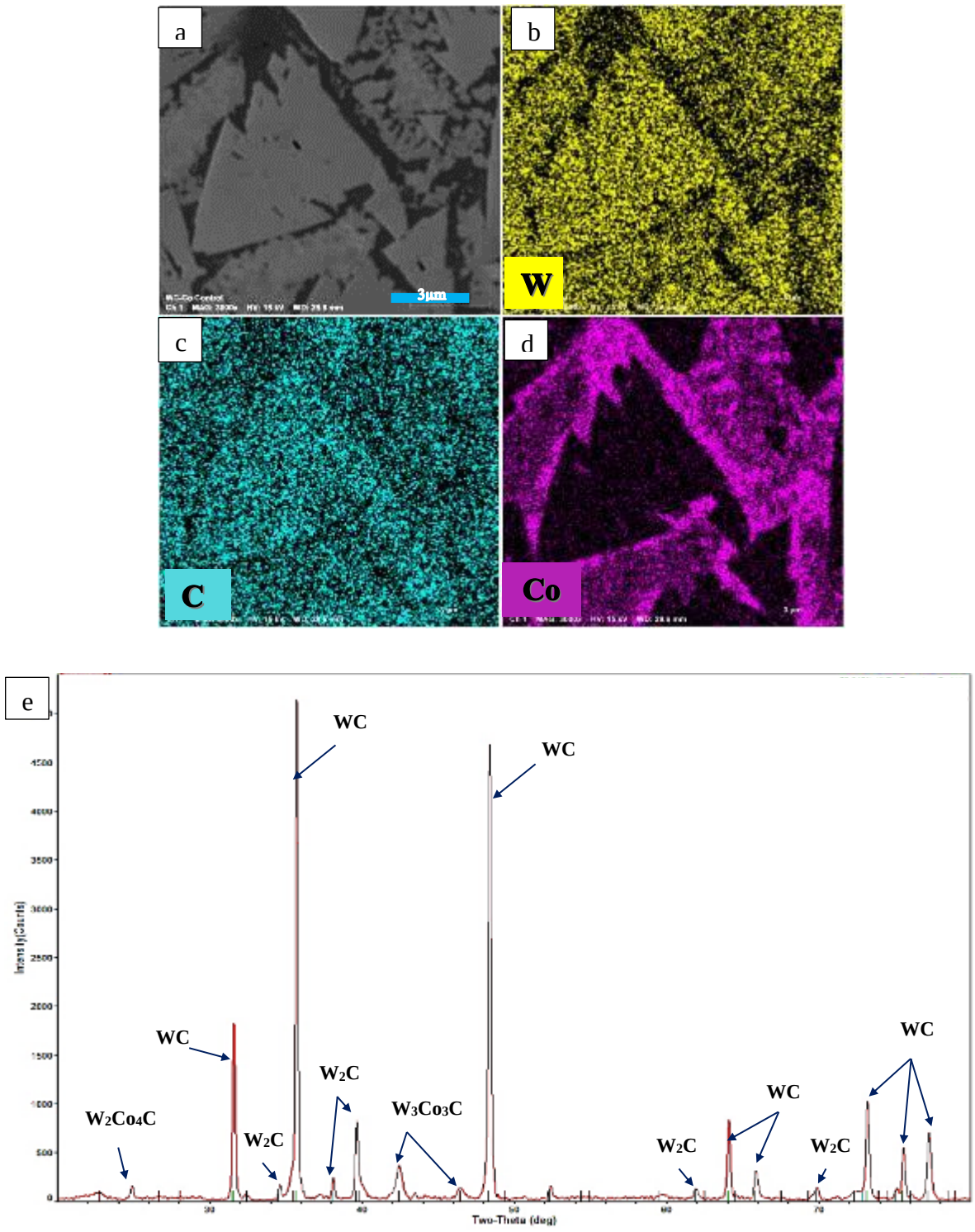

Figure 4-2 : EDS mapping (a to e) and X-ray diffraction pattern (f) of WC-Co as-sintered sample showing the WC, W_2C and W-C-Co phases.

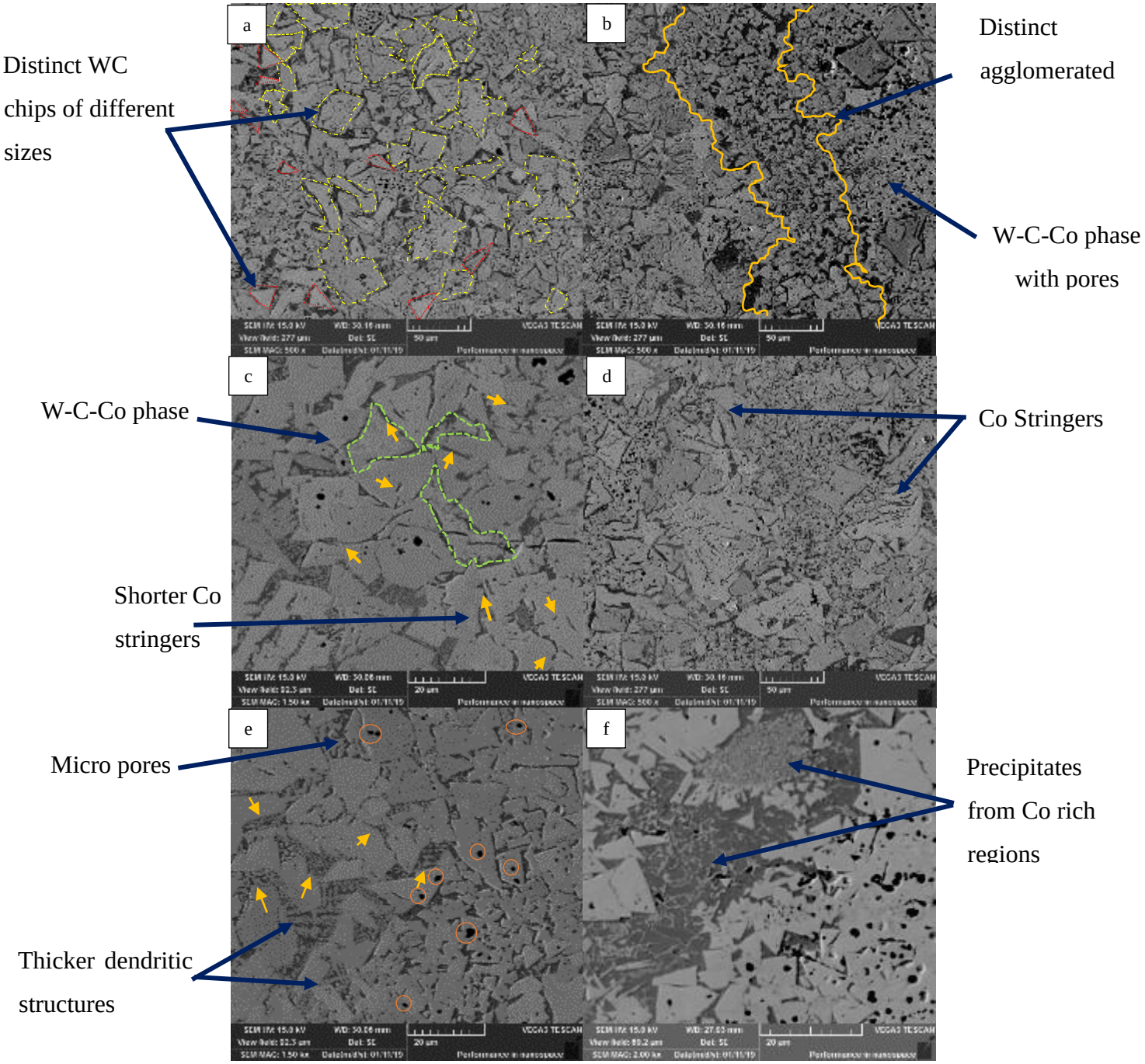

Figure 4-3 : Scanning Electron micrographs for 400°C sample describing the microstructural features and discontinuities identified as a result of heat treatment and processing technique.

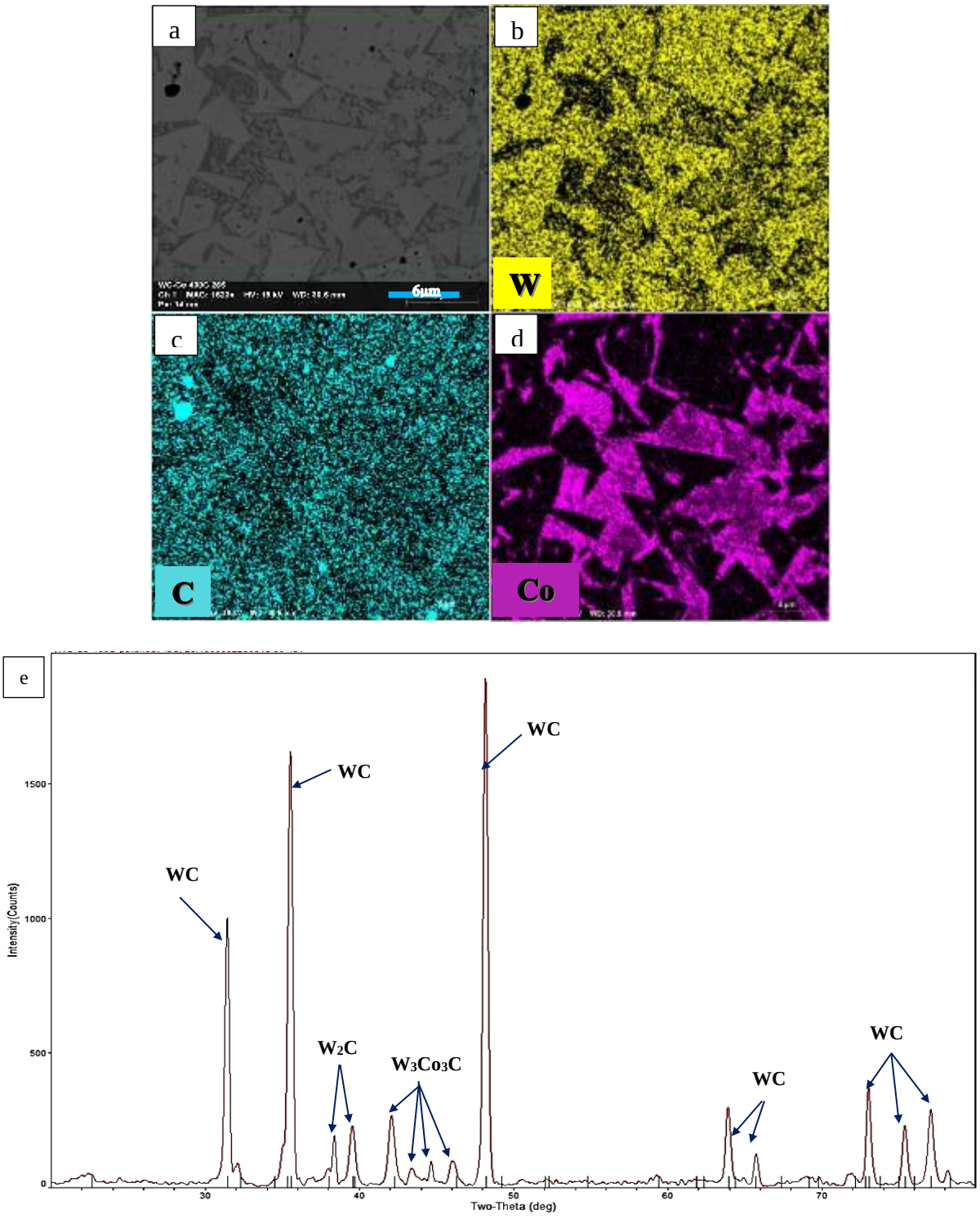

Figure 4-4 :EDS mapping (a to e) and X-ray diffraction pattern (f) of WC-Co sample heat treated at 400°C showing the WC, W_2C and W-C-Co phases.

4.1.3 Microstructural Evolution of the Heat-Treated Sample (A600 °C)

Figure 4-5 shows the microstructure of the as-printed WC-Co sample after heat treatment at 600 °C for 3 hrs. Again, the same microstructural features were observed in this specimen with some variations in the morphology, size and spatial distribution of these structures. The general sizes of the regular and irregular chips have become small. Some of the regular polyangular WC chips were embedded in the irregular polyangular chips (Figure 4-5(a & b)). Well-developed thicker and round dendritic structures were observed in this specimen with a significant reduction in the volume fraction of the dark background and W-C-Co phase as shown in Figure 4-5(c). Tiny agglomerations of the WC chips were also observed (Figure 4-5(d & e)) while some of the polyangular chips appeared to be elongated and twirled up together making it look like a bigger WC chip as can be seen in Figure 4-5(f). There were fewer stringers observed on the WC chips as well as fewer pores in the sample. Thus, fewer W-C-Co phase with fewer pores were observed in the sample when compared to the other samples. A few regions had micro-cracks which were not close to the crack stems as was observed in the other samples (Figure 4-5(g) and (h)).
The reduced dark background regions (Co-rich regions), globular WC-Co dendritic structures and twirled-up WC polyangular chips were evident on the EDS maps as shown in Figure 4-6 (a) – (e). In Figure 4-6(f), the diffraction pattern reveals a new W-C-Co (W_6Co_6C) phase and a drastic decrease in the peak height of the WC phase.

4.1.4 Microstructural Evolution of the Heat-Treated Sample (A800 °C)

Figure 4-7 shows the microstructures of the as-printed WC-Co sample after heat treatment at 800 °C for 3 hrs. Besides the regular and irregular polyangular chips, there were agglomerations of globular precipitates within the darker cobalt-rich regions in addition to platelet WC chips as shown in Figure 4-7(a) and (b). In addition, coarser dendritic structures were observed in this sample (Figure 4-7(c)). The volume fraction of the darker cobalt-rich regions was significantly reduced as a result of the precipitation of the coarser dendritic structures and spheroids in addition to the evolved platelet WC chips as shown in Figure 4-7(a) – (d). In this sample, the volume fraction of the irregular polyangular WC chips was significantly higher than was observed in the other samples. It was observed that the W-C-Co phase were identical to the WC chips in terms of

topography with embedded WC chips as shown in Figure 4-7(f). Nevertheless, these W-C-Co phase still had higher numbers of pores. Also, tiny agglomerations of WC chips were observed (Figure 4-7(g)). Few but wider micro-cracks with no branches were observed in Figure 4-7(h).
As shown in Figure 4-8, the EDS maps confirmed that the globular structures and W-C-Co phase were rich in W, C and Co with the dark background being the Co-rich region. The XRD showed higher peak heights for the W-C-Co phases as shown in Figure 4-8(f) including a new $WC_{0.5}$ phase that had lower peak heights. It was identified that the evolution of this $WC_{0.5}$ phase was as a result of the decomposition of W_2C phase.

4.1.5 Microstructural Evolution of the Heat-Treated Sample (A1000 °C)

The microstructure of the as-printed sample heat-treated at 1000 °C for 3 hours is shown in Figure 4-9. The relative sizes of the regular WC chips were smaller in this sample even though they appeared to be well-developed and distinct. The sample also had higher volume of pores within the W-C-Co phase with smaller volume fraction of dark Co-rich background regions as shown in Figure 4-9. In addition, coarser dendritic structures were observed in this sample as shown in Figure 4-9(a) and (f). The agglomerated tiny WC chips were identical to the regular polyangular WC chips.
Smaller numbers of thinner micro-cracks were observed in this sample as shown in Figure 4-9(h). The well-developed and distinct WC chips are apparent in the EDS maps shown in Figure 4-10. The
W-C-Co phase were rich in W, C and Co while the dark background was rich in Co. The XRD analysis showed an increase in the peak heights of some of the WC planes when compared to the WC planes in the 800 °C sample except for 102 planes as shown in Figure 4-10(f). A new W-C-Co ($W_{10}Co_3C_4$) was identified and a high reduction in the peak intensity of the $WC_{0.5}$ was observed.

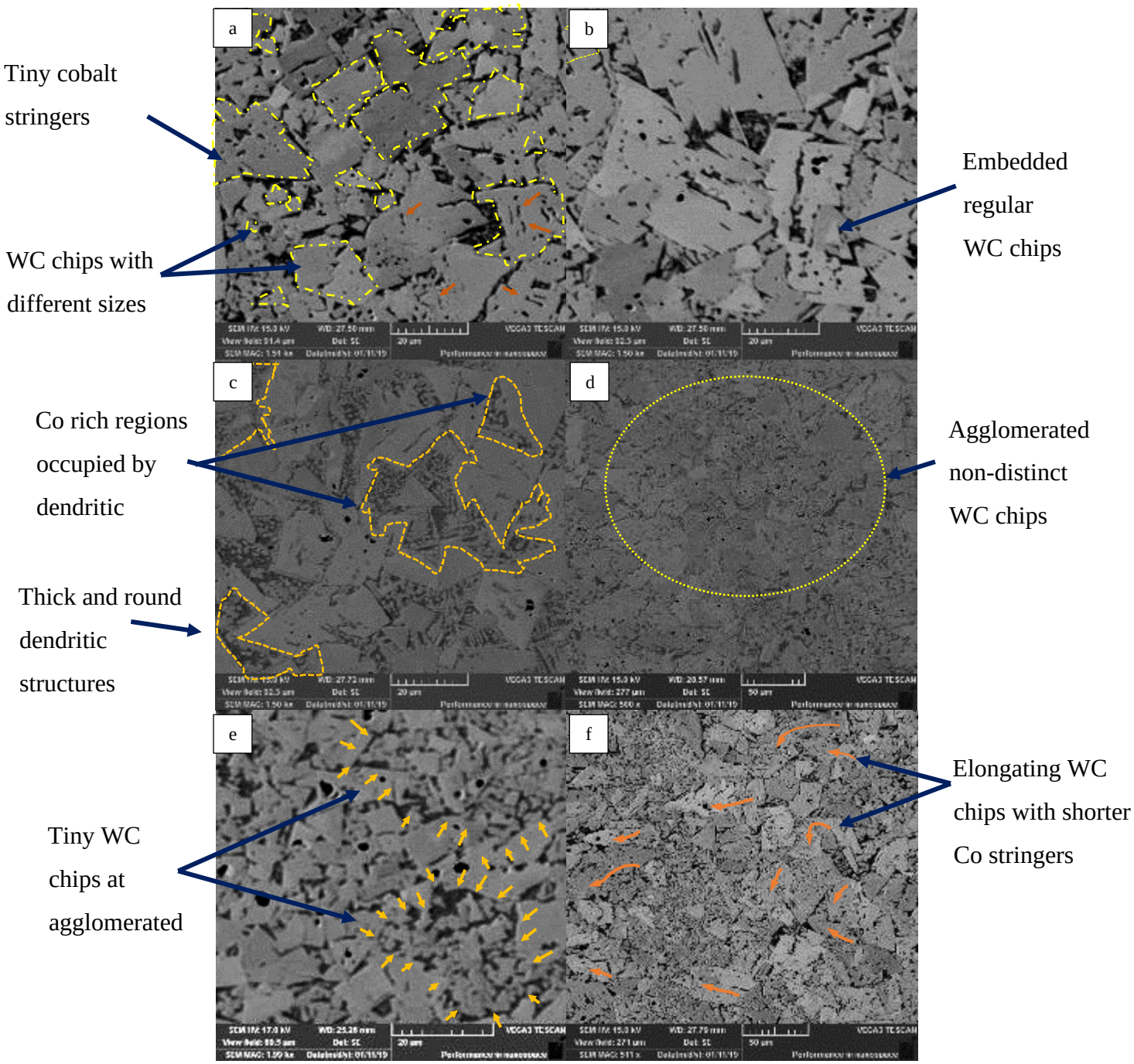

Figure 4-5 : Scanning Electron micrographs for 600°C sample describing the microstructural features and discontinuities identified as a result of heat treatment and processing technique.

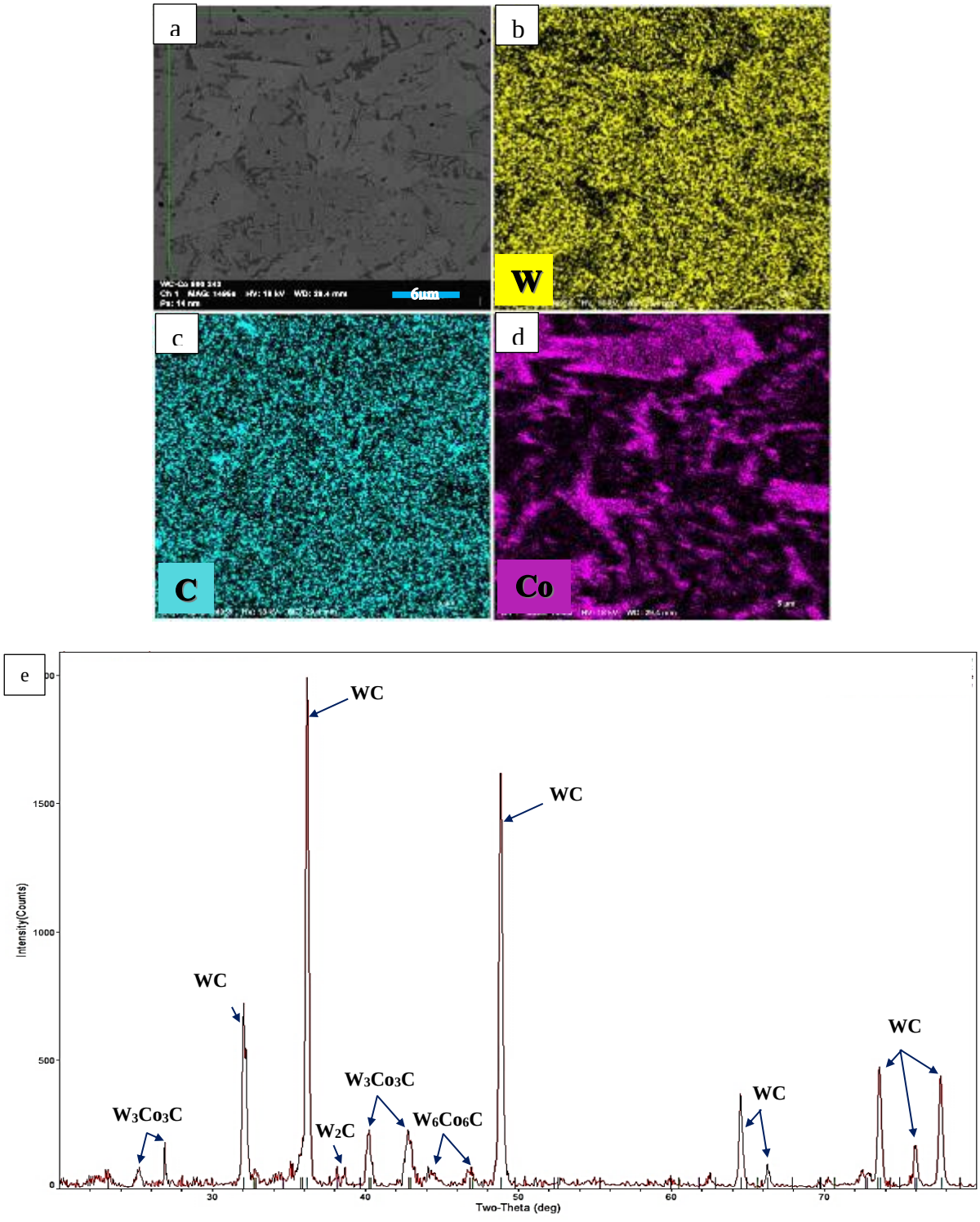

Figure 4-6 : EDS mapping (a to e) and X-ray diffraction pattern (f) of WC-Co sample heat-treated at 600°C showing the WC, W_2C and W-C-Co phases.

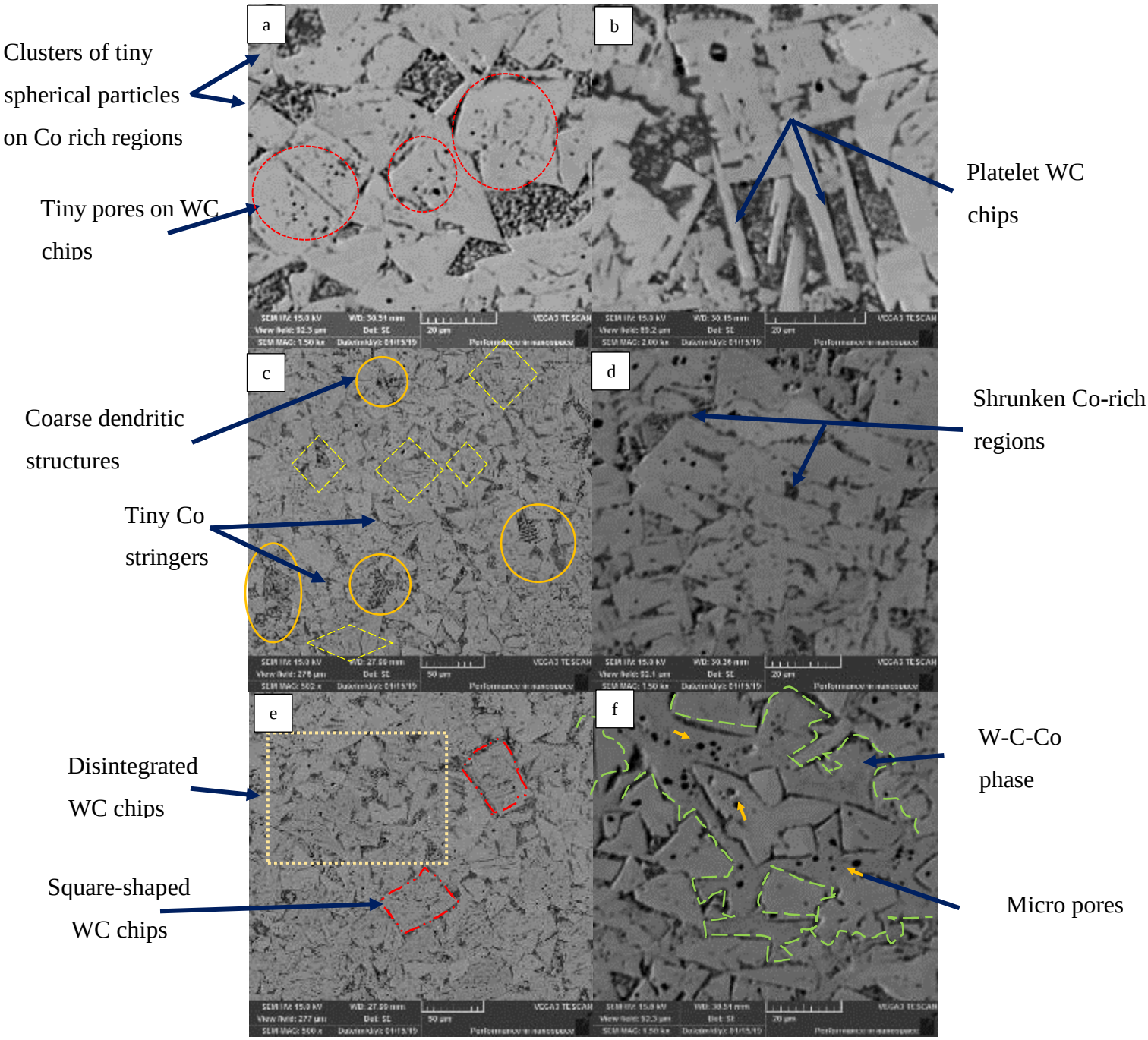

Figure 4-7 : Scanning Electron micrographs for 800°C sample describing the microstructural features and discontinuities identified as a result of heat treatment and processing technique

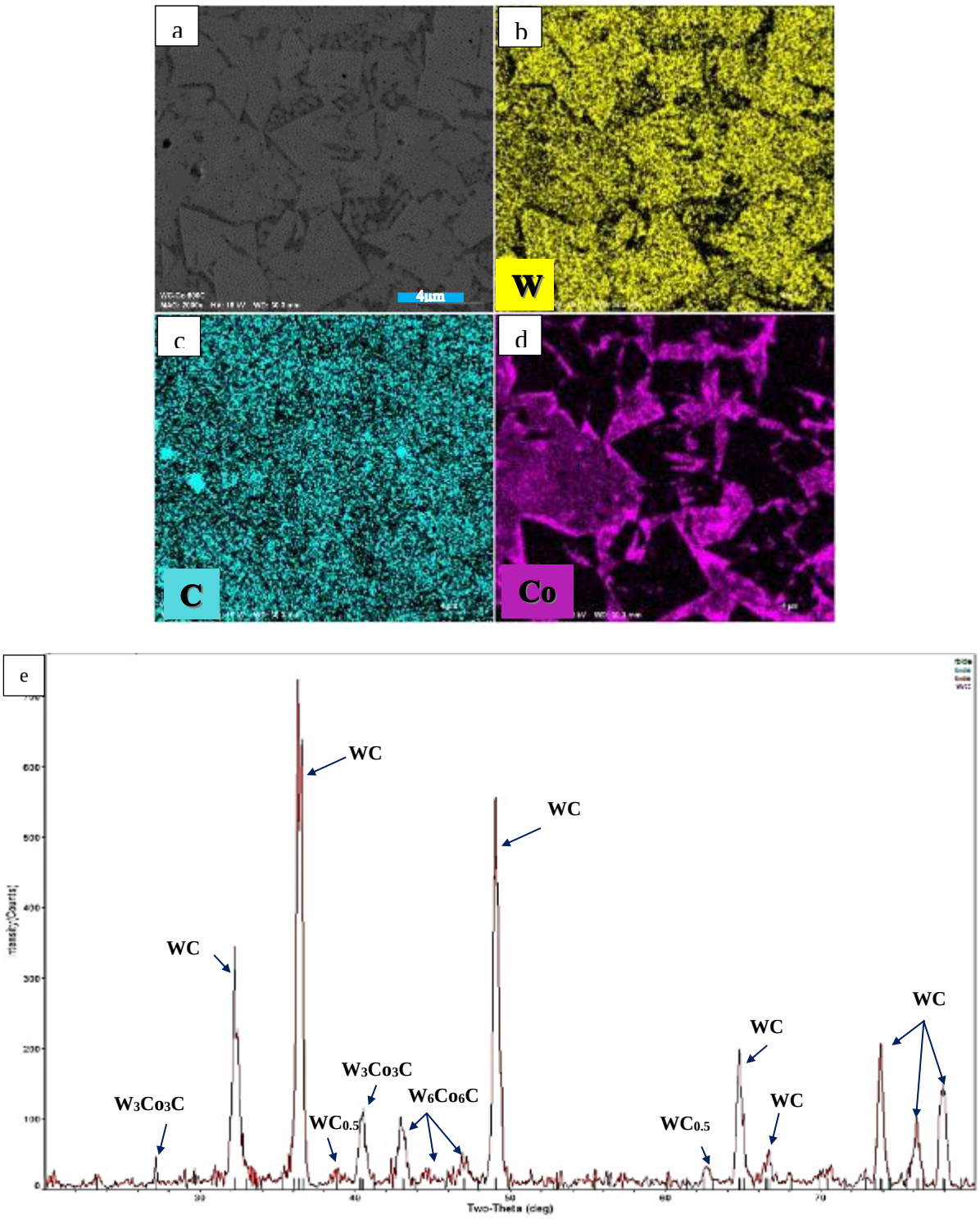

Figure 4-8 : EDS mapping (a to e) and X-ray diffraction pattern (bf) of WC-Co sample heat treated at 800 °C showing the WC, $WC_{0.5}$ and W-C-Co phases.

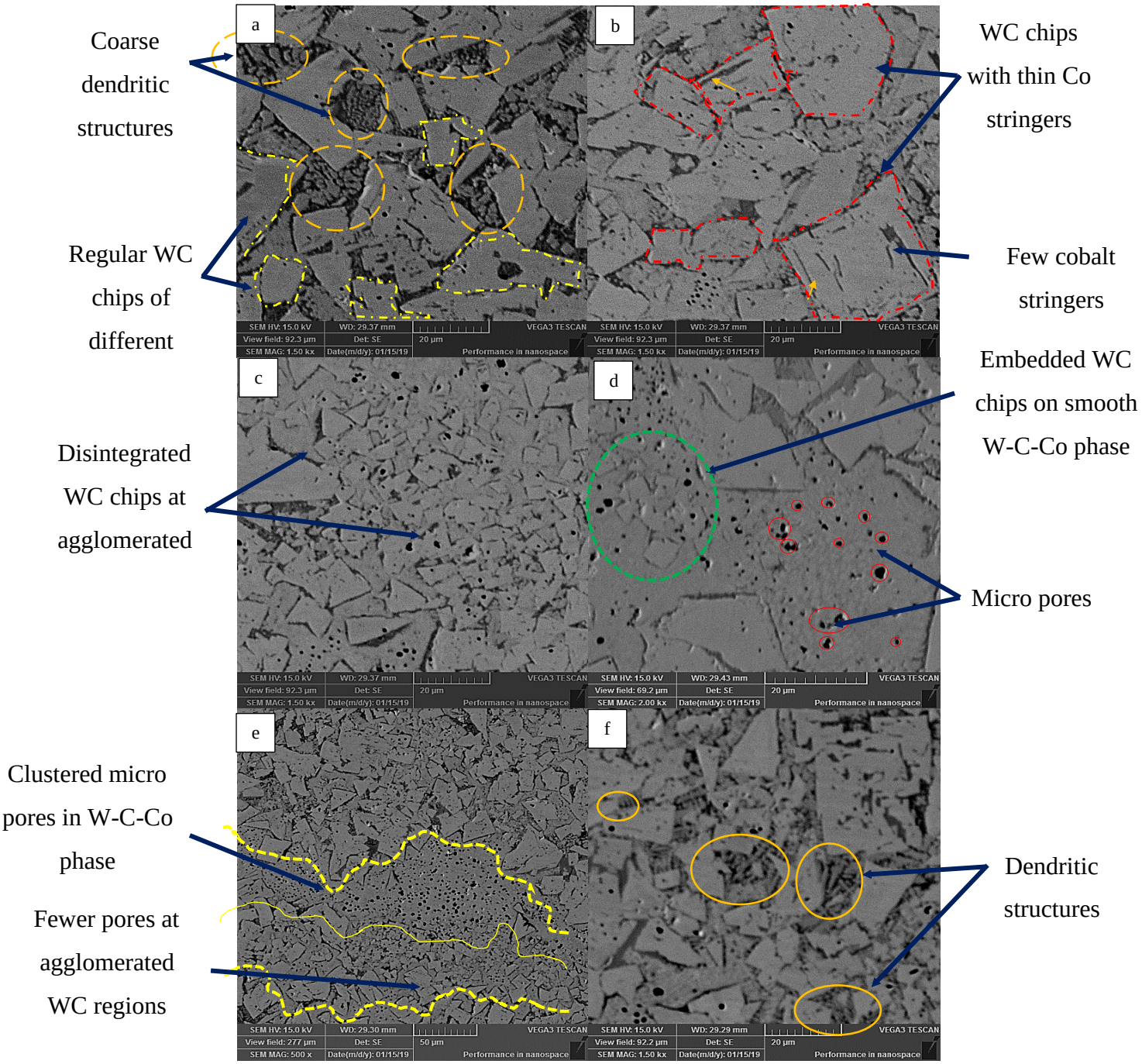

Figure 4-9 : Scanning Electron micrographs for 1000°C sample describing the microstructural features and discontinuities identified as a result of heat treatment and processing technique

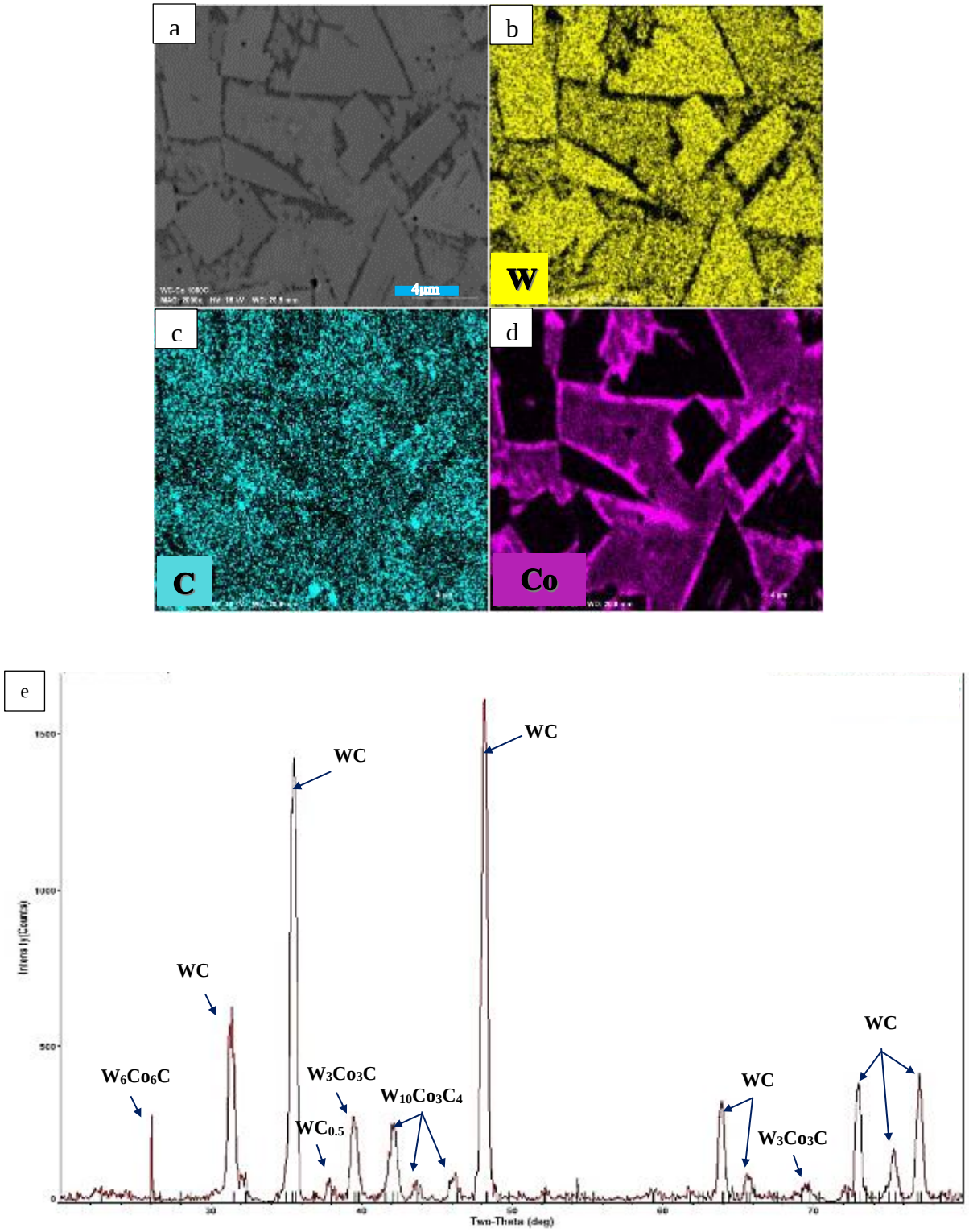

Figure 4-10 : EDS mapping (a to e) and X-ray diffraction pattern (f) of WC-Co sample heat treated at 1000°C showing the WC, $WC_{0.5}$, W-C-Co phases.

4.1.6 Effect of Heat Treatment on X-ray Diffraction Patterns of WC-Co alloy

Since the predominant phase with high intensities in all the samples was the WC phase, the peak heights and the Full Width at Half Maximum (FWHM) of the WC phases in all the samples were compared to understand the effect of heat treatment on this phase as shown in Figure 4-11 (a) and (b). Two patterns were observed in the peak heights as temperature increased as shown in Figure 4-11(a). In the first pattern (3 different planes), there were significant reductions in the peak heights as temperature increased from 0 °C (as-printed sample) to 800 °C with the peak height increasing again from 800 °C to 1000 °C. In the second pattern (3 different planes), the peak height decreased from 0 °C (as-printed sample) to 400 °C, increased from 400 °C to 600 °C, decreased from 600 °C to 800 °C and increased from 800 °C to 1000 °C. What was consistent in the peak heights was that the as-printed sample always had the highest peak height while the 800 °C sample had the lowest peak heights irrespective of the WC planes as shown in Figure 4-11(a). On the other hand, it was generally identified that irrespective of the crystallographic plane, the FWHM of most WC planes in the samples increased from 0 °C (as-printed sample) to 400 °C, decreased from 400 °C to 600 °C and increased from 600 °C to 1000 °C as shown in Figure 4-11(b).

4.2 Mechanical Properties After 3D Printing and Heat Treatment

4.2.1 Microhardness, Fracture Toughness and Wear Properties

Figure 4-12 shows the average hardness and fracture toughness of the as printed and heat-treated samples. Generally, the heat-treated samples have relatively higher hardness when compared to the as-printed sample as shown in Figure 4-12(a). Thus, the heat treatment can be used to increase the hardness of the as-printed WC-Co alloy. From the graph, there is an increase in hardness when the temperature rises to 600 °C and then a steady decline up to 1000 °C. There was approximately 36% increase in hardness when the as-printed specimen was compared with the sample heat treated at 600 °C. Also, there was approximately 8% increase in hardness when the as-printed sample was heat-treated at 1000 °C. The increase in hardness at 600°C was coupled with the highest fracture toughness (8.37 MPa√m), representing a 34% increase in fracture toughness, when the sample was compared with the as-printed sample (6.23 MPa√m) as shown on Figure 4-12(b). Even though the

approximate hardness of the sample heat-treated at 1000 °C was relatively higher than the as-printed sample, the as-printed sample had better fracture toughness (approximately 9% higher) than the sample heat-treated at 1000 °C.

In addition, Table 4 and Figure 4-13 show the mass loss and coefficient of friction of the as-printed and heat-treated WC-Co samples compared with the standard EOS MSI 3D printed Maraging steel. The mass loss of each of the samples was calculated after wear tests and used to characterize the wear rate of the samples. After heat treatment of the as-printed sample at 400 °C, there was approximately 54% decrease in mass loss when compared with the as-printed sample. There was a continuous increase in mass loss of the samples heat treated between 600 °C and 1000 °C. Nevertheless, the EOS MSI Maraging steel had the highest mass loss when compared to all the WC-Co samples with an approximate 238% increase in mass loss when the EOS MS1 was compared with the as-printed WC-Co alloy as shown in Figure 4-13.

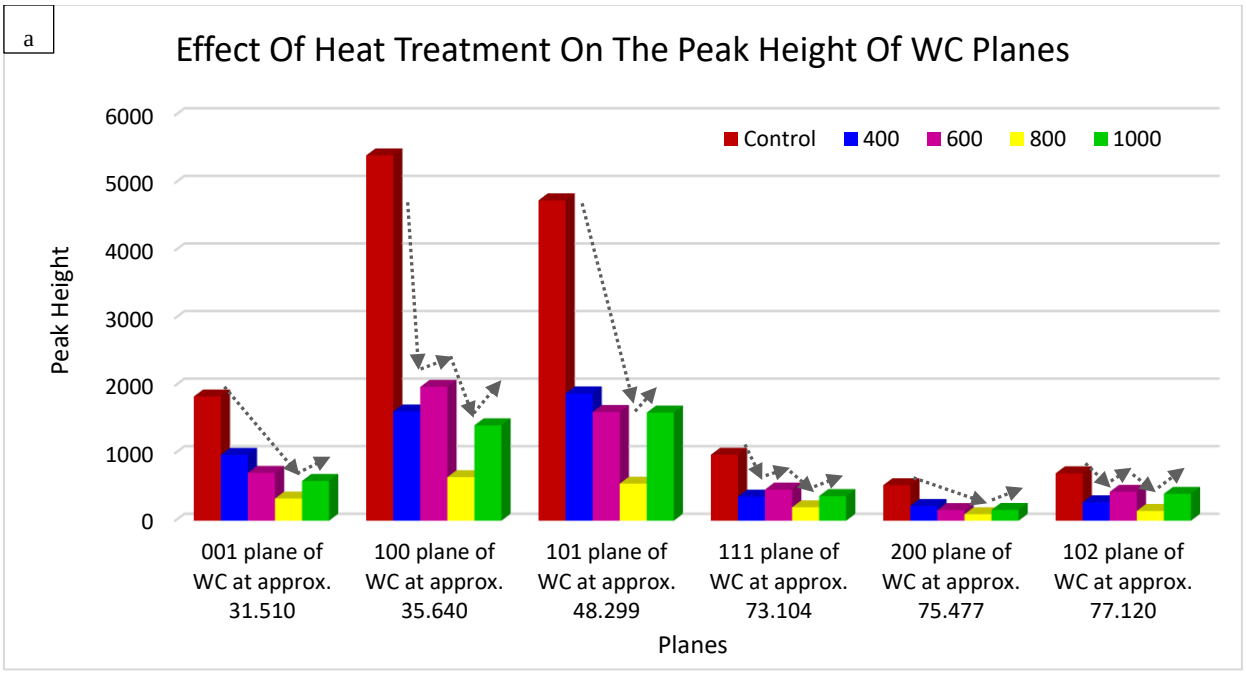

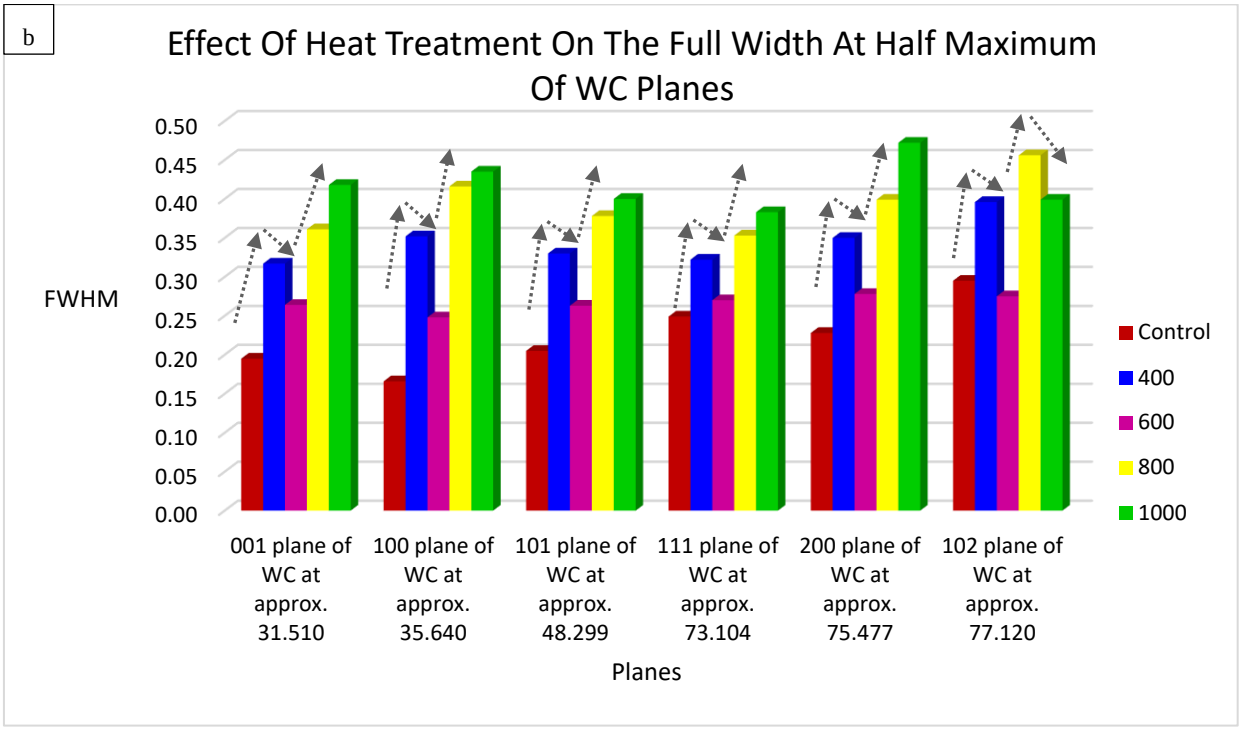

Figure 4-11 : (a) A graph of Peak height of the various WC planes identified compared against each sample labelled as control(as-printed), 400 (400°C), 600 (600°C), 800 (800°C) and 1000 (1000°C). (b): A graph of FWHM of the various WC planes identified compared against each sample labelled as control (as printed), 400 (400°C), 600 (600°C), 800 (800°C) and 1000 (1000°C).

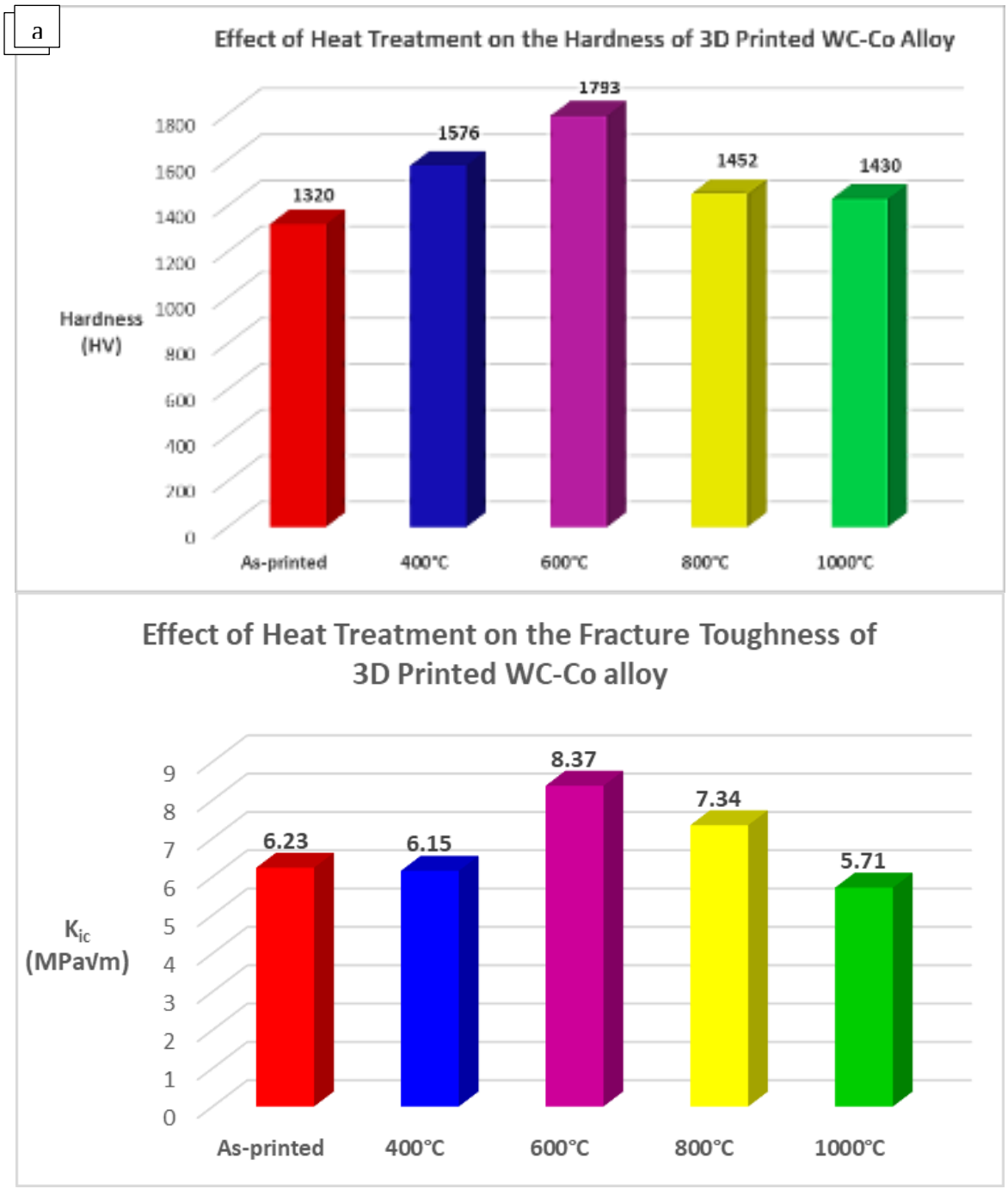

Figure 4-12 : Effect of heat treatment on the (a) hardness (HV) (b) fracture toughness of 3D printed WC-Co alloy

Table 4 : Wear test results for the as printed and heat-treated WC-17Co samples at various temperatures

Sample	**Mass of sample before wear (g)**	**Mass of sample after wear (g)**	**Mass loss (10^{-4})**	**Coefficient of Friction (COF)**
As printed	11.2144	11.2118	26	0.2
400°*C*	14.3001	14.2989	12	0.2
600°*C*	11.7721	11.7691	30	0.2
800°*C*	10.2155	10.2115	40	0.2
1000°*C*	15.0243	15.0194	49	0.3
Maraging Steel (MS1)	10.1200	10.1112	88	0.6

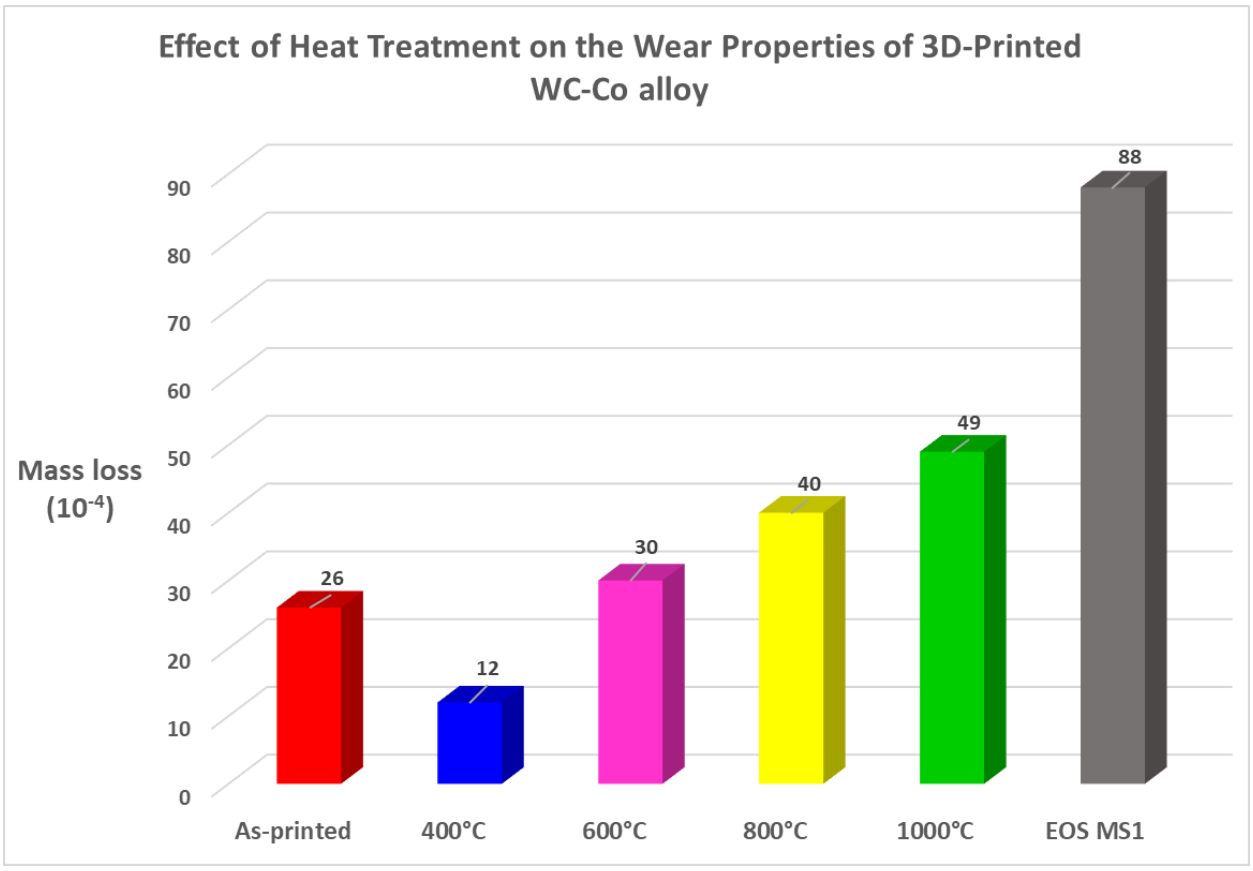

Figure 4-13 : Effect of heat treatment on the wear properties of 3D printed WC-Co alloy

4.3 Microstructural Evolution After 3D Printing and Heat Treatment Of WC-Co-hBN Alloys

4.3.1 Microstructural Evolution of the As-Printed WC-Co-hBN Sample

Figure 4-14 shows scanning electron micrographs describing the microstructural features and structure of the as-printed WC-Co-hBN sample. Generally, a similar structure just like the as printed WC-Co sample was observed. This included the polyangular chips (irregular and regular), "foggy" (shapeless) regions and dark background regions. Dendritic structures that were observed on WC-Co were however not present on this sample. Figure 4-14(a) shows the polyangular chips observed on the as-printed sample. The sizes of the chips were relatively smaller as compared to the WC-Co as printed sample. On an average count, the regular polyangular chips were more than the irregular ones. Most of the chips also did not have strips or stringers on them. In Figure 4-14(b), regions occupied by the foggy regions have been shown. The foggy regions were very distinct and were very well defined. The foggy region occupied just about 30% in terms of area fraction over analysed samples. Just between these foggy regions and polyangular chips was a thin dark layer which we are calling the dark background regions (Figure 4-14(c)). Some of these layers could be only as thick as 4um. Furthermore, some regions of the sample had agglomerations of tiny chips as shown in Figure 4-14(d). These agglomerations of tiny chips were usually observed to be mixed with the "foggy" regions. A lot of these agglomerated regions were not identified in the sample. However, the ones identified were very distinct and occupied regions that were about 60um wide. A lot of pores were also observed inn the whole sample. Most of the pores were observed on the polyangular chips whereas few occupied the foggy regions. However, in the WC-Co as printed sample, we observed that the pores were prevalent in the foggy regions rather.

Figure 4-15 shows results from EDS analysis and X-Ray diffraction for the WC-Co-hBN as-printed sample. Doing this aided in the understanding of the distribution of the chemical elements qualitatively and identify the various structures and regions observed in the sample by the elemental analysis. The elemental mapping showed that the polyangular chips were still composed of primarily W and C as the dominant elements as shown in Figure 4-15(a) to (e). We therefore still wish to name the polyangular chips in this material as WC chips. The other structures followed the same chemical composition as observed in the WC-Co samples. However, the mapping also revealed no specific information of the distribution of B and N (Figure 4-15(a)-(g)) The X-ray

Diffraction (XRD) analysis, as shown in Figure 4-15 (g), showed that the as-printed specimen was made up of W_3Co_3C, W_3Co_3N, $W_9Co_3C_4$, CoWB, $Co_{5.47}N$ and the hexagonal WC phases.

4.3.2 Microstructural Evolution of the Heat-Treated Sample (B400 °C)

Figure 4-16 depicts scanning electron micrographs that describe the evolution of the microstructure of the printed WC-Co-hBN sample after heat-treatment at 400 °C for 3 hrs. Generally, the same microstructural features observed in the as-printed sample, namely irregular and regular polyangular WC chips, "foggy" (shapeless) regions and Co rich background regions, were observed in this sample. However, they size of these structures varied as compared to as-printed sample. The regular and irregular polyangular WC chips appeared to be smaller than the as-printed sample as shown in Figure 4-16(a). However, bigger chips were also observed which were not in the as printed sample. They had fleshed themselves with other WC chips forming a WC-WC chip interface which has no Co layer or foggy region between (Figure 4-16(b)). Additionally, the regions which had the Co rich regions had a form of precipitate forming out of it. It looked like a honeycomb structure and it was much evident in Co rich regions which were identified in the sample. In other areas, two form of foggy areas were observed. One region looked rough on the surface and had globules captured in them (Figure 4-16(c)) Other foggy regions had a smooth surface with no globules in them (Figure 4-16(d)). There were more smooth foggy regions on the sample than the rough ones. Also, fewer stringers were observed on the WC chips. Pores were observed on the relatively large WC chips with some micro cracks. However, the foggy regions had little or no pores or cracks in them.

The EDS maps from the sample showed that the distinct polyangular chips were rich in W and C while the dendritic structures were rich in both W, C and Co (Figure 4-17(a)-(e)). The dark background was predominantly Co. From Figure 4-17(f), which depicts the X-ray diffraction patterns of the heat-treated sample at 400 °C, there is no new phase seen in the sample with respect to the as-printed sample. However, two distinct peaks which were identified as W_3Co_3N were not present in this sample. In addition, there were significant reductions in the peak heights of the $W_9Co_3C_4$, CoWB, $Co_{5.47}N$ and WC phases as compared to the as-printed sample.

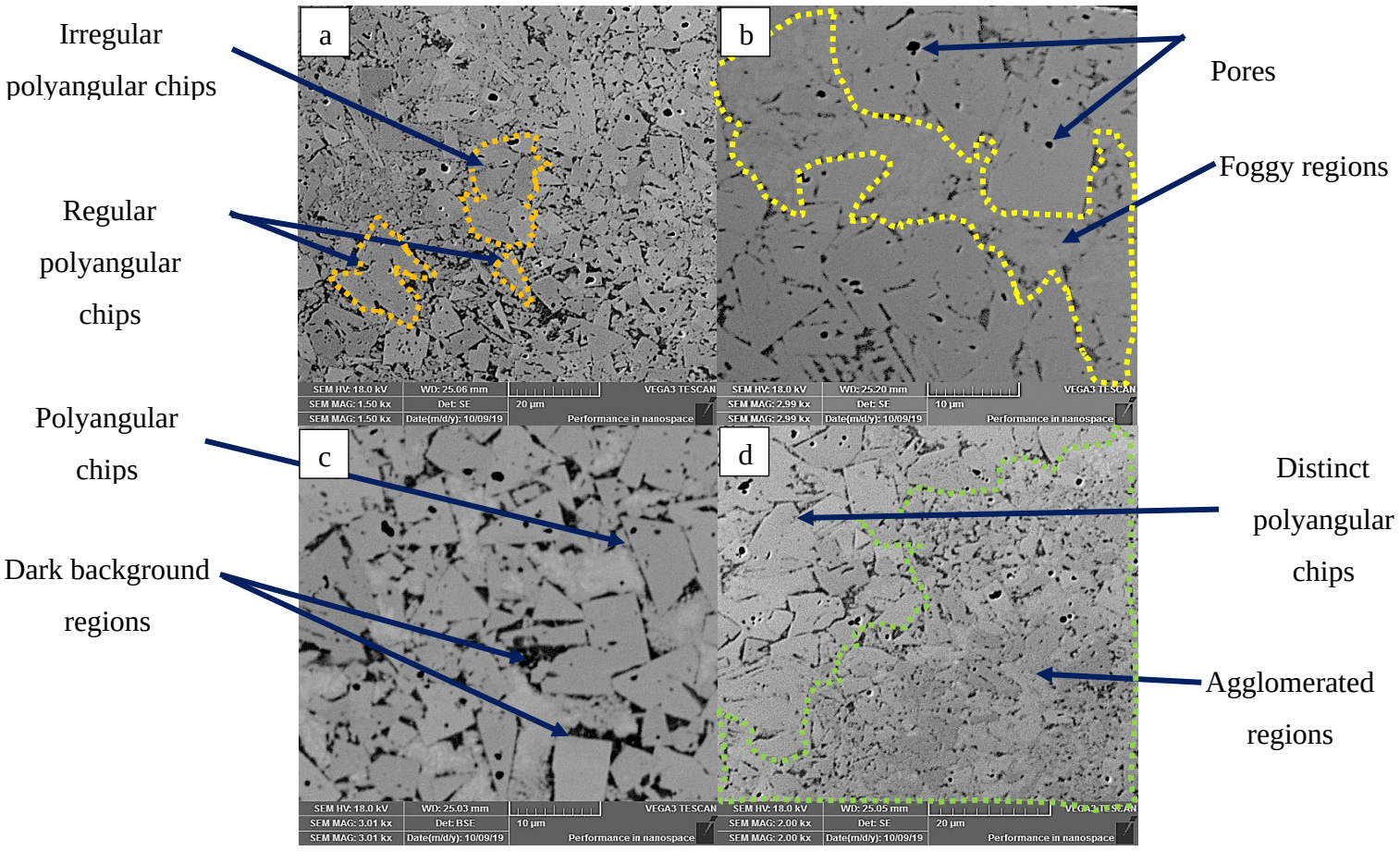

Figure 4-14 : SEM Micrographs of unetched as-printed WC-Co-hBN sample

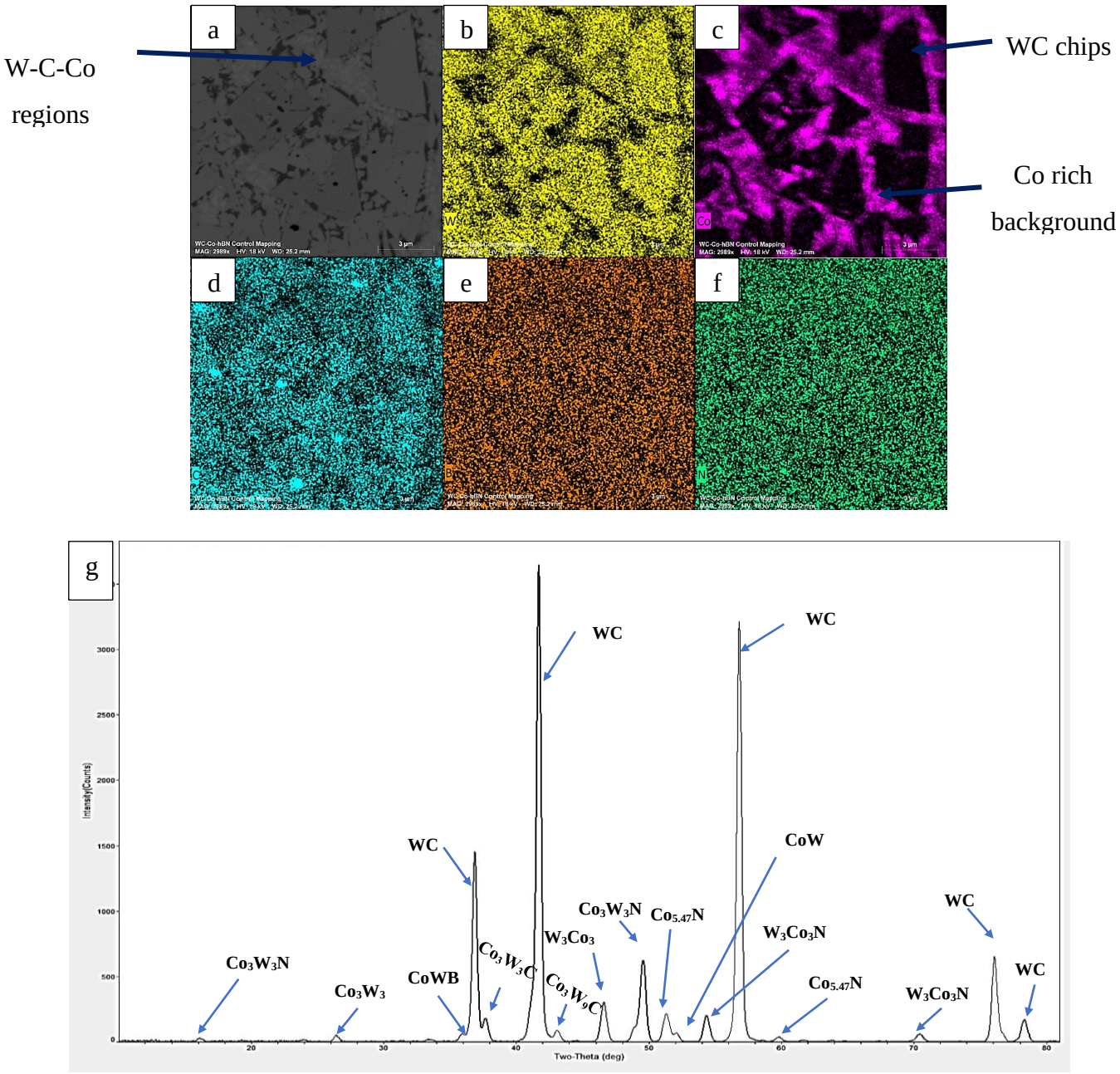

Figure 26 : EDS mapping (a to e) and X-ray diffraction pattern (f) of as-printed WC-Co-hBN sample showing W_3Co_3C, W_3Co_3N, $W_9Co_3C_4$, CoWB, $Co_{5.47}N$ and the hexagonal WC phases.

4.3.3 Microstructural Evolution of the Heat-Treated Sample (B600 °C)

Figure 4-18 shows the microstructure of the as-printed WC-Co-hBN sample after heat treatment at 600 °C for 3 hrs. Again, a similar microstructure is observed on this sample with some variations in the morphology, size and spatial distribution of these structures. The WC chips seem to be well developed and a relatively a smaller size compared to the as-printed sample WC-Co-hBN sample. Some of the regular polyangular WC chips seemed to be embedded in the foggy regions (Figure 4-18(a & b)). In Figure 4-18(b), precipitates in the Co rich regions have become much bigger and looked globular taking the form of the rough foggy regions observed in the 400°C sample. Thicker foggy regions with smooth surfaces were observed on this sample with a high-volume fraction present. In some portions, the foggy regions and the small WC chips were not distinct. They looked liked they have merged. Most agglomerated regions were now distinct, and fewer Co rich regions could be seen in them (Figure 4-18 (c) and (d)). A few regions had the pores especially the WC chips.

However, the foggy regions had little or no pores in them.

The reduced sized WC chips, depleted Co rich regions and the two distinct foggy regions were captured on the on the EDS maps as shown in Figure 4-19 (a) – (e). Surprisingly, in Figure 4-19 (f), the diffraction pattern revealed just one W_3Co_3N phase whiles a lot of W_3Co_3C phases which were not there came were now present. The intensities of the WC phase had reduced drastically as compared to the as printed WC-Co-hBN sample.

4.3.4 Microstructural Evolution of the Heat-Treated Sample (B800 °C)

Figure 4-20 shows the microstructures of the as-printed WC-Co-hBN sample after heat treatment at 800 °C for 3 hrs. Generally, there was drastic depletion in the Co rich regions, and most WC chips were very big and had come together with other WC chips. In Figure 4-20(a), big WC chips have been identified. The chips are closely packed together leaving no gaps between them. There were more stringers in the sample as a result of the compaction. However, there were still precipitates growing from the Co rich regions elsewhere as shown in Figure 4-20(b). Additionally, a few of these Co rich regions that were as big as 10um were identified. The volume fraction of the foggy regions which had a rough surface had increased. They also had few pores in them which

were identified as cobalt stringers. In Figure 4-20(d), it is observed that, the foggy regions which had a smooth surface had become embedded in the microstructure. It was therefore very difficult to distinguish between the WC and foggy regions with the smooth surface.

As shown in Figure 4-21, the EDS maps confirmed that the few co rich regions as well as the stringers as mainly made up of cobalt. The XRD showed higher peak heights for the W-C-Co phases as shown in Figure 4-21(f) including the new W_3Co_3C phases that had been observed in the previous sample. The intensities of the W-C-Co phases were primarily larger than that o the ones in the as printed sample.

4.3.5 Microstructural Evolution of the Heat-Treated Sample (B1000 °C)

The microstructure of the as-printed sample heat-treated at 1000 °C for 3 hours is shown in Figure 4-22. The relative sizes of the WC chips were smaller in this sample. In Figure 4-22(a), smaller regular WC chips were scattered across the sample. Fewer agglomerated regions were also present. However, most of these agglomerated regions had distinct small WC chips in them. The embedded foggy regions were also present at high volume fractions. The WC chips in these regions were very small and it was difficult to identify them (Fig 4-22) Little or no Co rich regions were present in the sample. Additionally, the present co rich regions had precipitates in them. In Figure 4-22(d), acicular WC structures were also identified in the sample. The occupied areas where foggy areas were present. There was a high-volume fraction of these acicular WC chips on the sample. They had small sizes and a skewed aspect ration making them long and thin.

The developed structures as well as the embedded foggy regions could be having their elemental composition shown on the EDS maps shown in Figure 4-23. The XRD analysis showed a decrease in the peak heights of some of the WC planes when compared to the WC planes in the 800 °C sample as shown in Figure 4-23(f). A new phase called the BN was seen on this sample. The phase had an appreciable intensity even though this was the first time it is being seen in the sample.

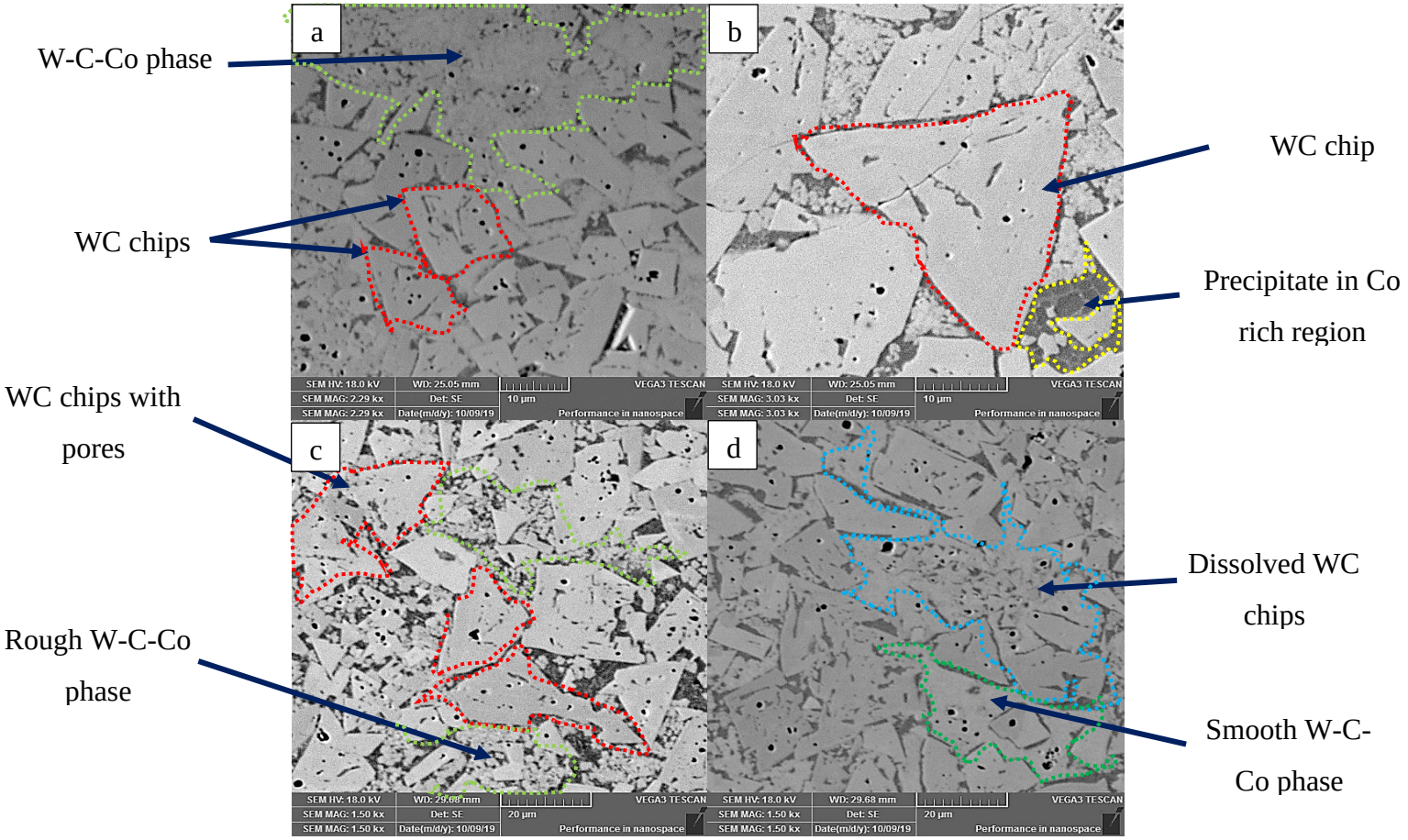

Figure 27 : SEM Micrographs of unetched as-printed WC-Co-hBN sample heat treated at 400°C.

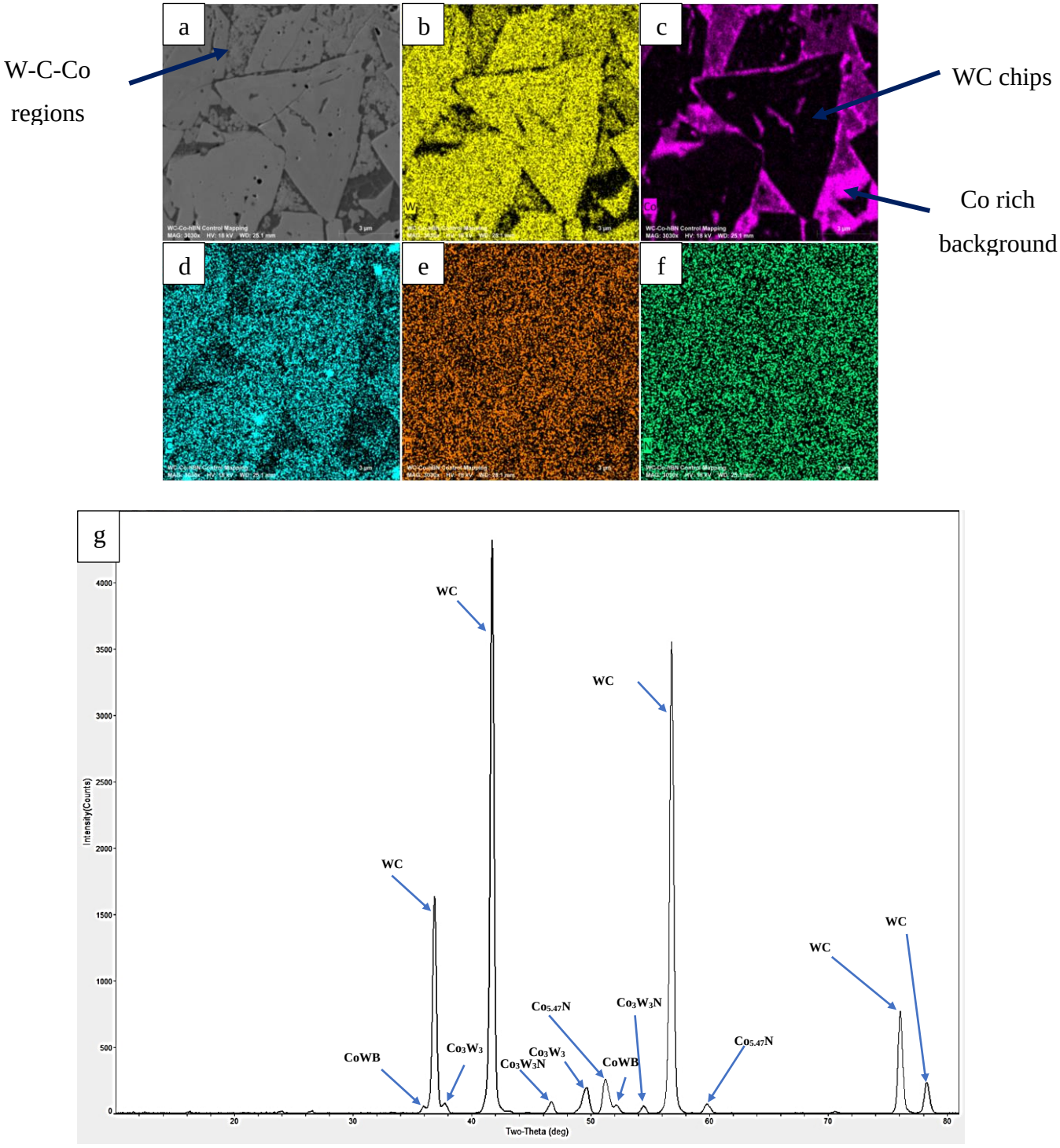

Figure 28 : EDS mapping (a to e) and X-ray diffraction pattern (f) of WC-Co-hBN sample heat treated at 400°C showing the $W_9Co_3C_4$, CoWB, $Co_{5.47}N$ and WC *phases.*

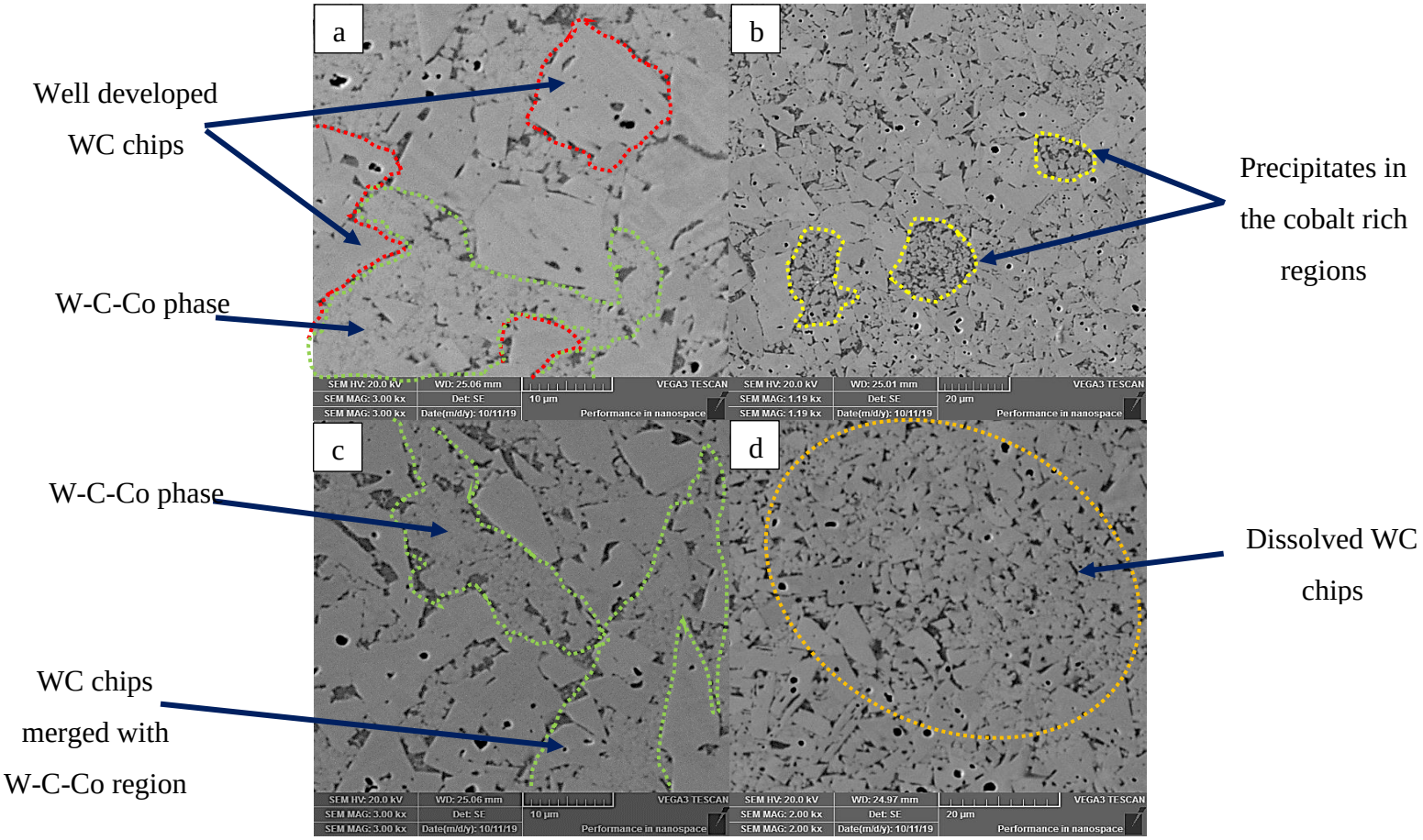

Figure 29 : SEM Micrographs of unetched as-printed WC-Co-hBN sample heat treated at 600°C.

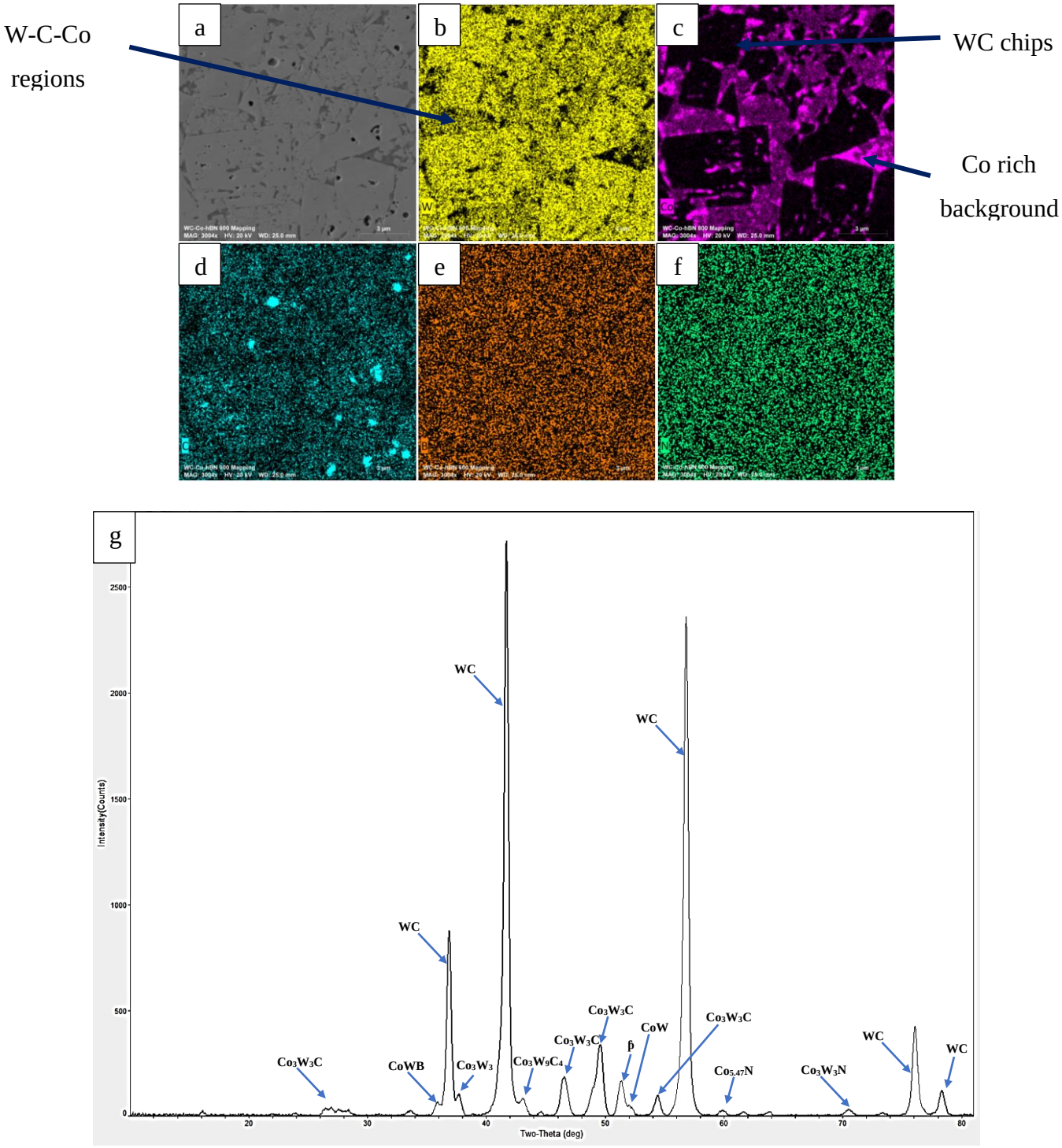

Figure 30 : EDS mapping (a to e) and X-ray diffraction pattern (f) of WC-Co-hBN sample heat treated at 600°C showing the CoWB, $Co_{5.47}N$ and WC *phases with new* $W_3Co_3C_3$, phase. *surface*

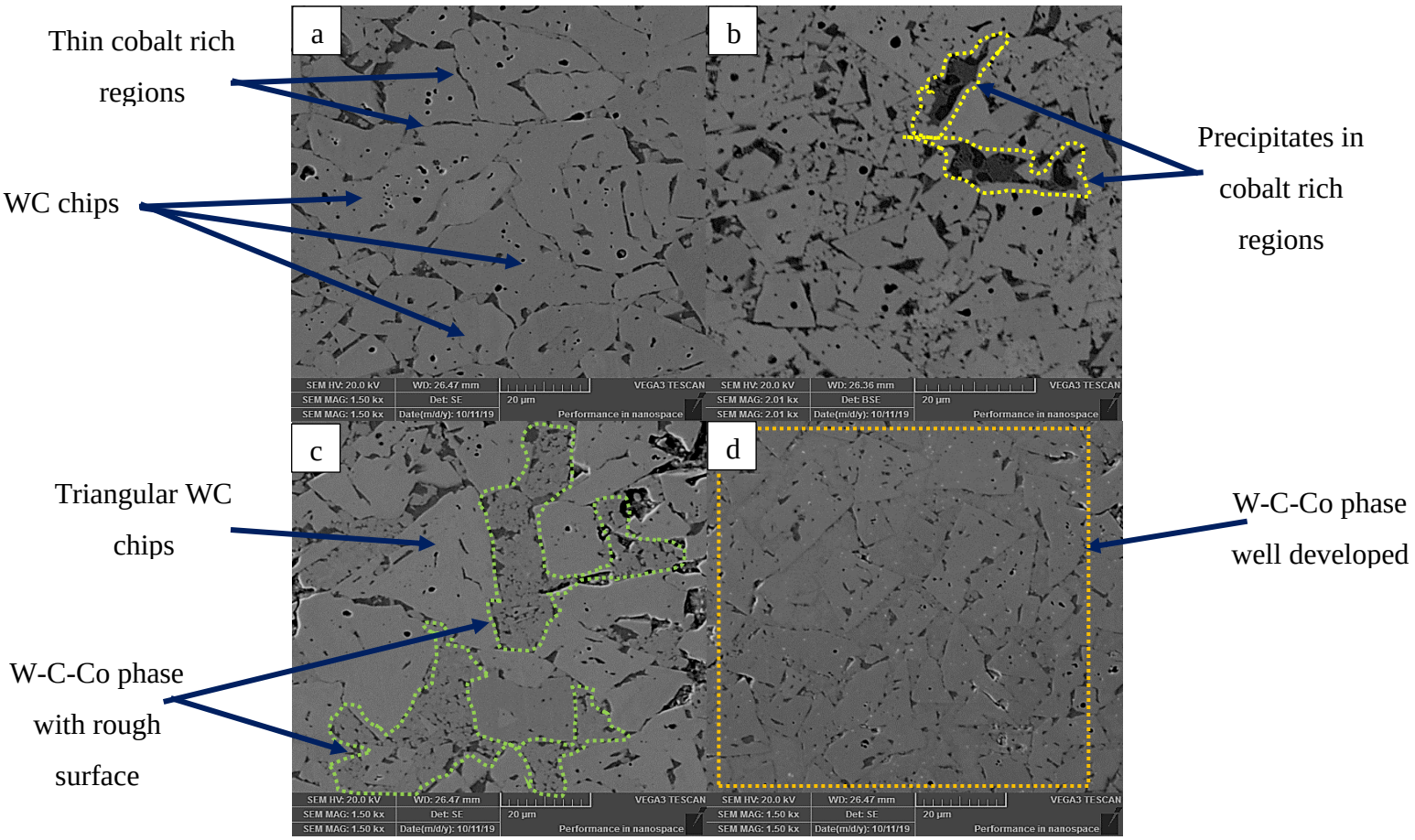

Figure 31 : SEM Micrographs of unetched as-printed WC-Co-hBN sample heat treated at 800°C.

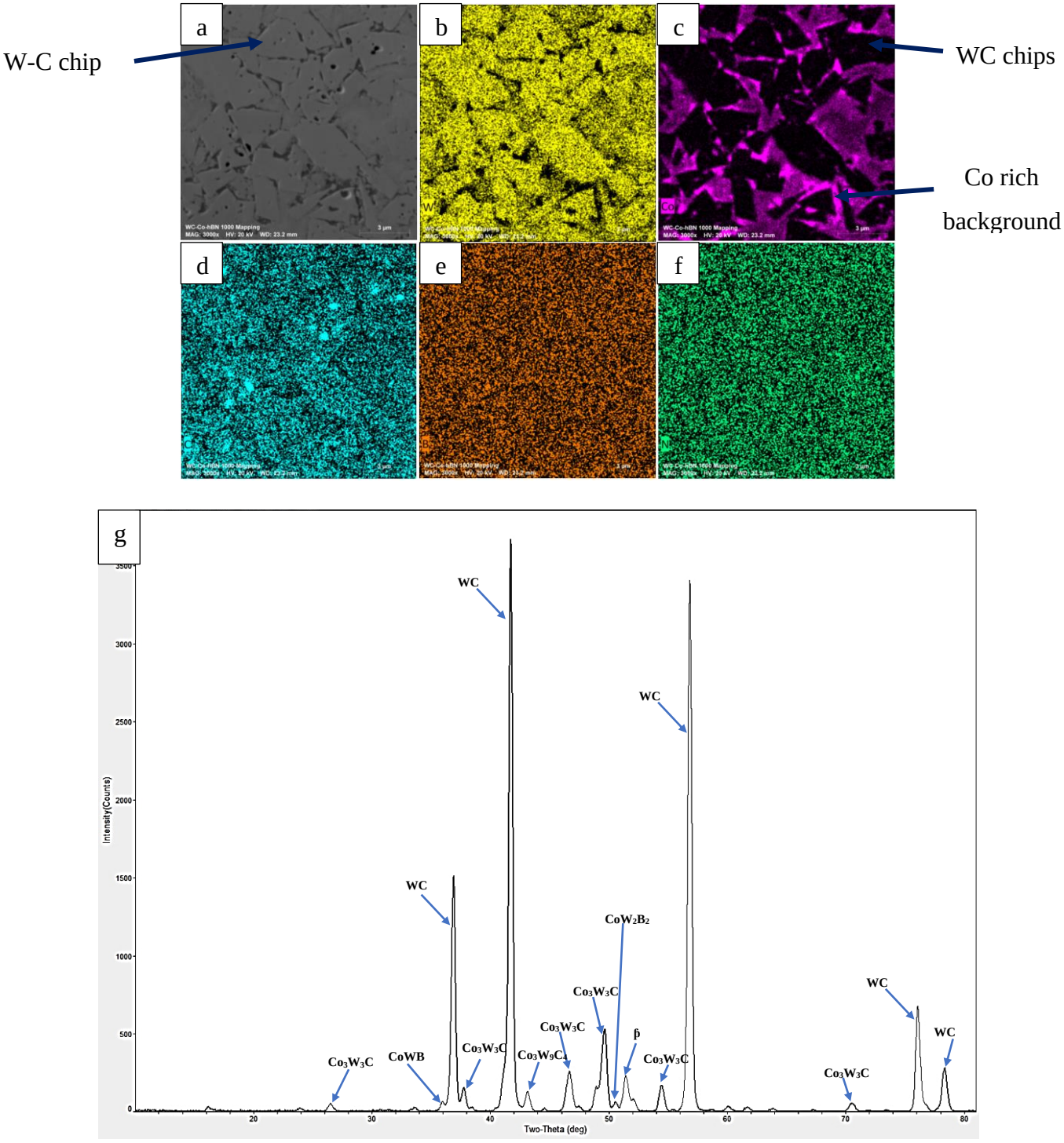

Figure 32 : EDS mapping (a to e) and X-ray diffraction pattern (f) of WC-Co-hBN sample heat treated at 600°C showing the $W_3Co_3C_3$, CoWB, $Co_{5.47}N$ and WC *phases.*

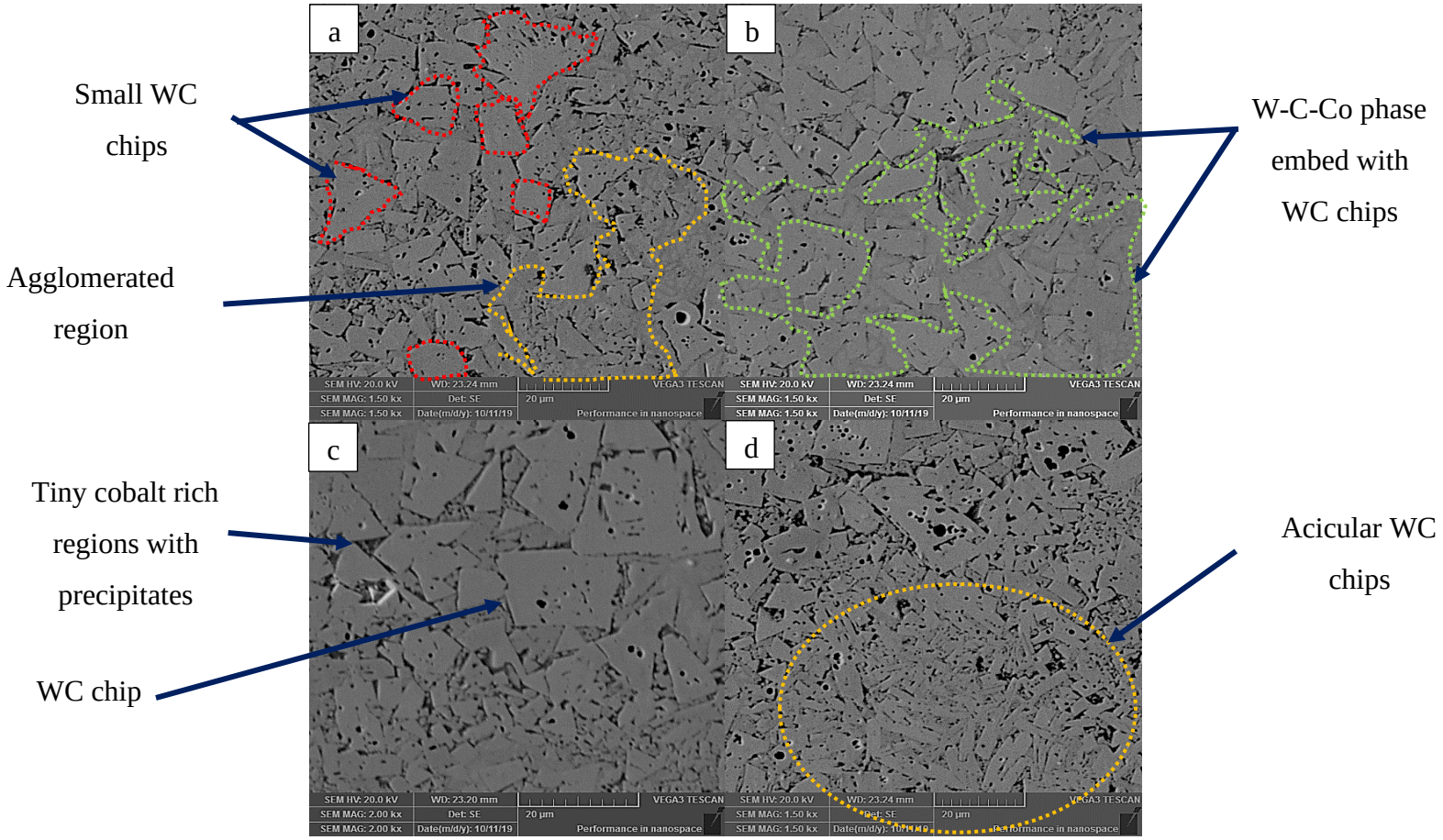

Figure 4-22 : SEM Micrographs of unetched as-printed WC-Co-hBN sample heat treated at 1000°C.

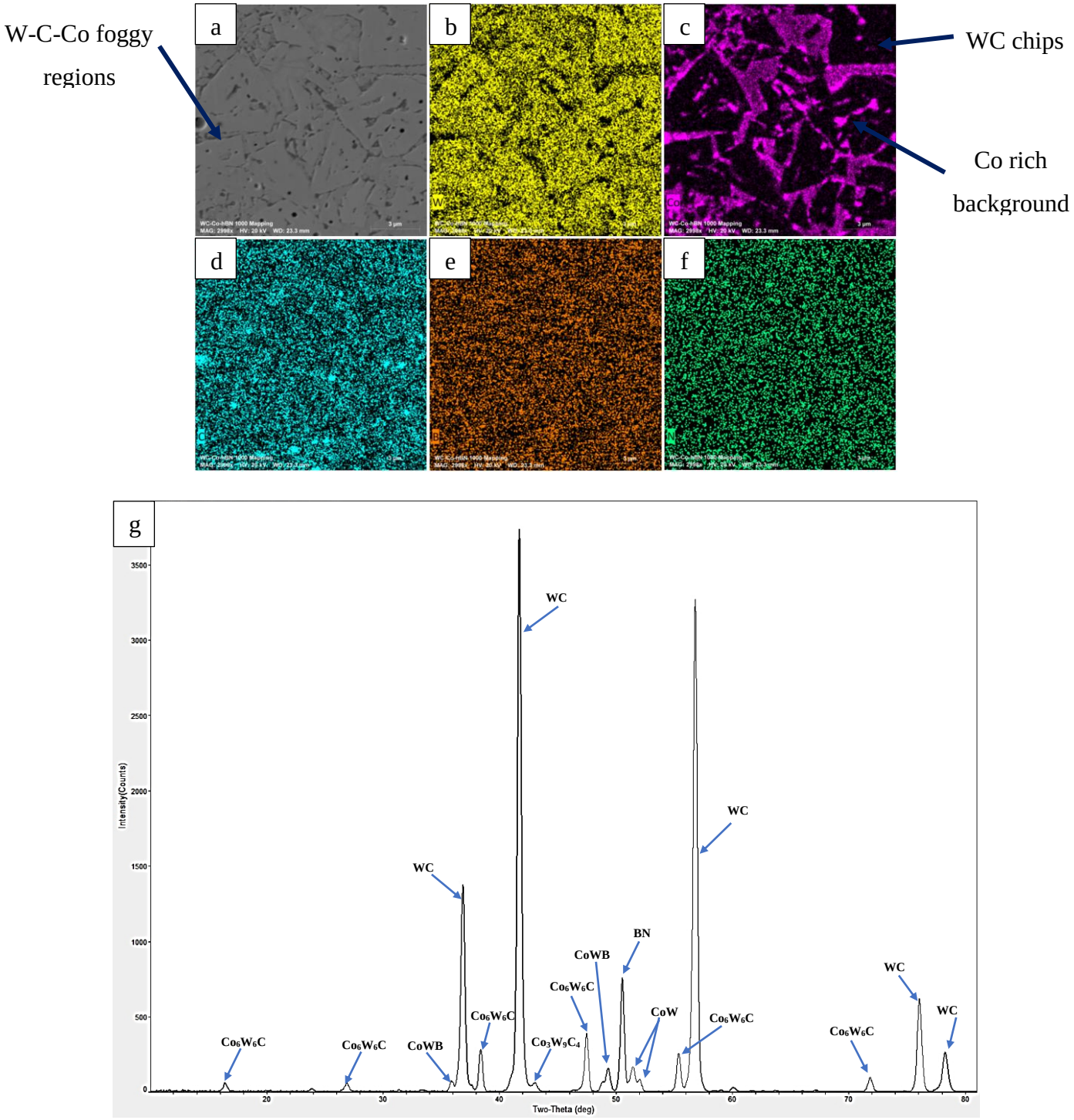

Figure 4-23 : EDS mapping (a to e) and X-ray diffraction pattern (f) of WC-Co-hBN sample heat treated at 1000°C showing the, WC, W-C-Co phases and a new phase as BN.

4.3.6 Effect of Heat Treatment on X-ray Diffraction Patterns of WC-Co-hBN alloy

Using the WC phases which were found in all the samples, the peak heights and the Full Width at Half Maximum (FWHM) of these WC phases in all the samples were compared to understand the effect of heat treatment on this phase as shown in Figure 4-24 (a) and (b). On the peak height graph, (Figure 4-24(a)), the peak height increased from as-printed sample to 400 °C, dropped steeply from 400 °C to 600 °C, and a high increase in peak height was observed from 600 °C to 800 °C and also increased just a little more from 800 °C to 1000 °C. This was consistent in all the different WC planes analysed.

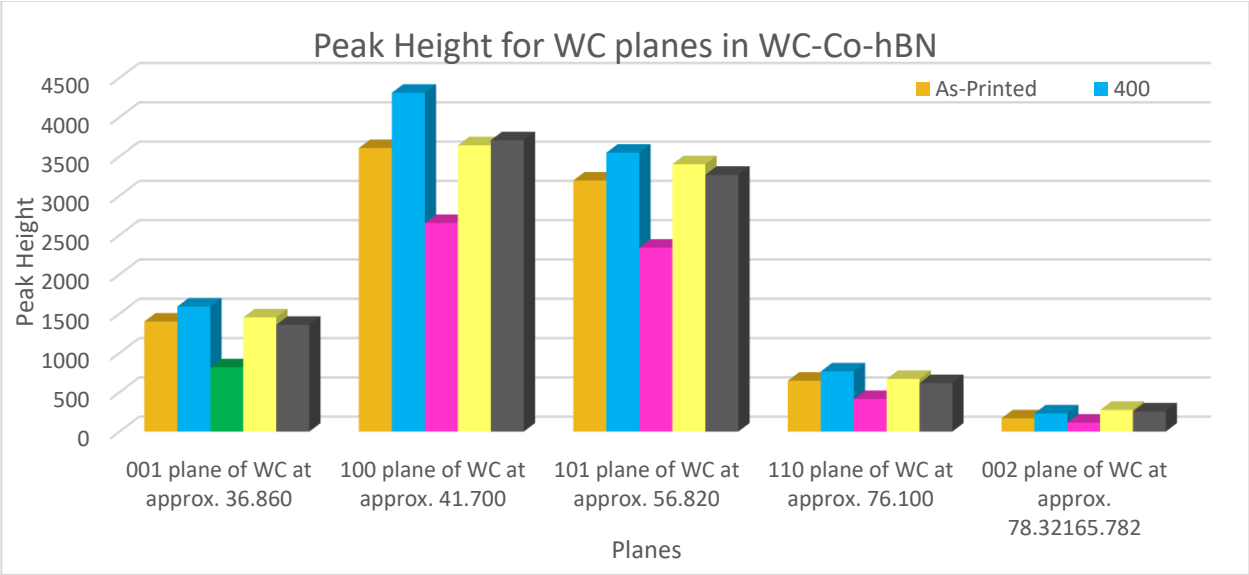

Figure 4-24 : (a) A graph of Peak height of the various WC planes identified compared against each sample labelled as control(as-printed), 400 (B400°C), 600 (B600°C), 800 (B800°C) and 1000 (B1000°C).

4.4 Mechanical Properties After 3D Printing and Heat Treatment Of WC-Co-hBN Alloys

4.4.1 Microhardness, Fracture Toughness and Wear Properties

Figure 4-25 shows the average hardness and fracture toughness of the as printed and heat-treated WC-Co-hBN samples. Generally, the heat-treated samples have relatively lower hardness when compared to the as-printed sample as shown in Figure 4-25(a). This clearly shows that, the hardness of the sample could not be increased using the heat treatment. However, the values recorded for the samples were higher than the hardness values of the WC-Co samples. The as-printed WC-Co-hBN samples was 350% higher than the as-printed sample of the WC-Co sample. The sample with the least hardness was recorded on the sample heat treated at 800°C. However, it was approximately three times higher than the hardness of the as-printed WC-Co sample heat treated at 800°C. Coupling this to the fracture toughness, the as-printed had the highest fracture toughness. The heat-treated samples had relatively lower fracture toughness values but the B800 saw a highest value among the heat-treated value. However, it was 11.5% lower than the as-printed sample. The WC-Co-hBN samples had better fracture toughness values even though they were still below the conventional manufactured cemented carbides.

In addition, Table 4 and Figure 4-26 show the mass loss and coefficient of friction of the as-printed and heat-treated WC-Co-hBN samples. The mass loss of each of the samples was calculated after wear tests and used to characterize the wear rate of the samples. After heat treatment of the as printed sample at 400 °C, there was approximately 54% decrease in mass loss when compared with the as-printed sample. There was a continuous increase in mass loss of the samples heat treated at and between 600 °C and 1000 °C. Nevertheless, the WC-17Co samples had the highest mass loss when compared to all the WC-Co-hBN samples. This is shown in a graph depicted in Figure 4.27. The comparison was possible because both materials were tested for wear properties using the same conditions. It can be seen that the sample with the lowest wear rate was the WC-Co-hBN sample heat treated at 1000 °C. The commercial 3D printed Maraging steel (MS1) still remained the sample with the worst wear properties as compared to both the WC-17Co and WcCo0hBN materials. Additionally, the wear rate of the WC-17Co sample heat treated at 400°C had the same wear properties as its WC-Co-hBN counterpart.

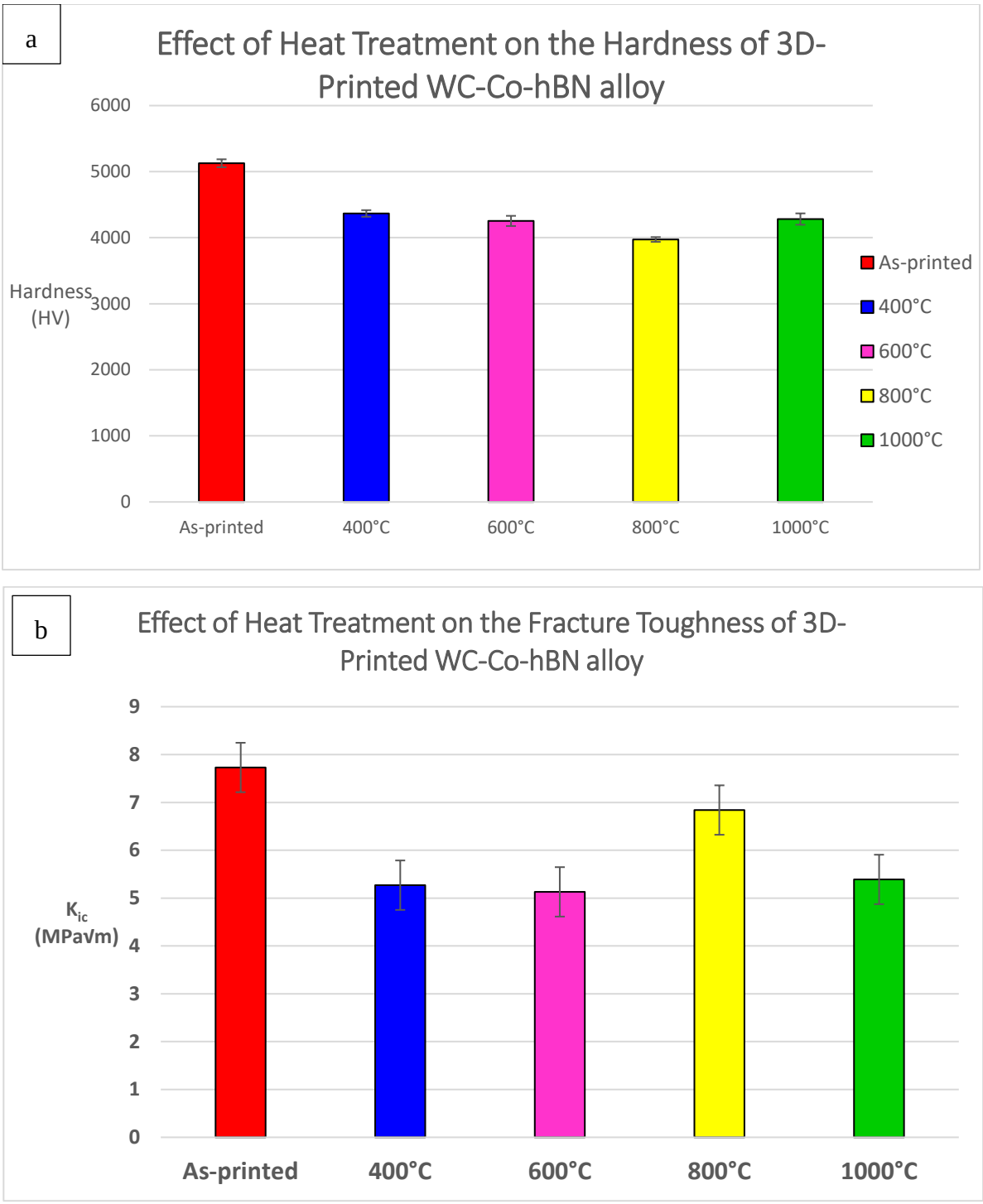

Figure 4-25 : Effect of heat treatment on the (a) hardness (HV) (b) fracture toughness of 3D printed WC-Co-hBN alloy

Table 5 : Wear test results for the as printed and heat-treated WC-Co-hBN samples at various temperatures

Sample	**Mass of sample before wear (g)**	**Mass of sample after wear (g)**	**Mass loss (10^{-4})**	**Coefficient of Friction (COF)**
As printed	21.5264	21.5246	18	0.2
400°*C*	19.2845	19.2833	12	0.2
600°*C*	21.8777	21.8764	13	0.2
800°*C*	25.4813	25.4723	9	0.2
1000°*C*	16.9958	16.9955	3	0.3

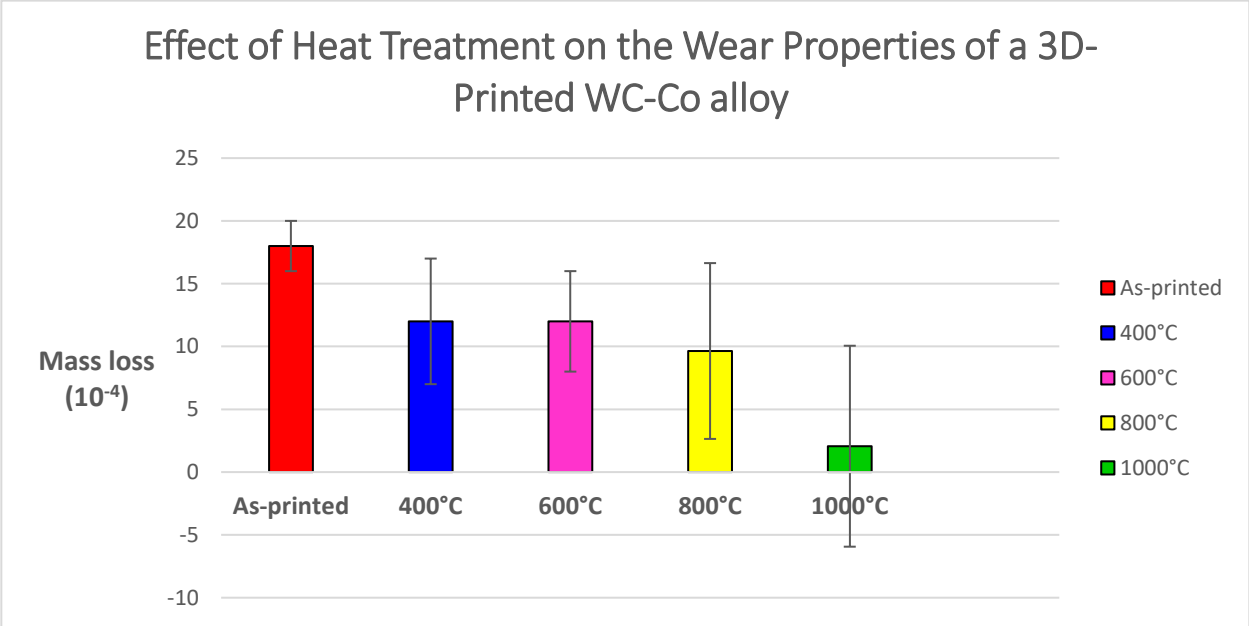

Figure 4-26 : *Effect of heat treatment on the wear properties of 3D printed WC-Co-hBN alloy*

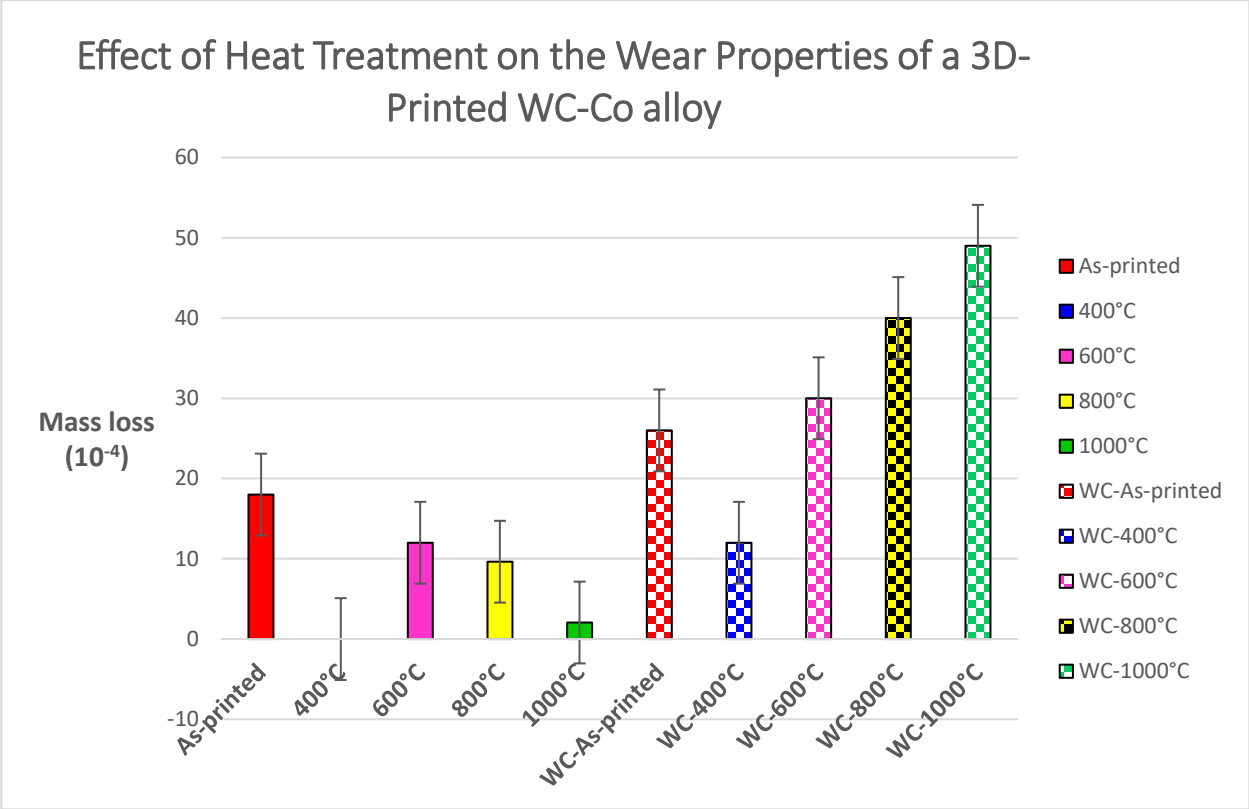

Figure 4-27 : Comparison of the WC-Co-hBN, Maraging Steel (MS1) and WC-17Co samples' wear rates

5.0 DISCUSSION OF RESULTS

5.1 Effect of Processing and Post Processing Heat Treatment on The Microstructure of The Material.

Materials processed using metal-based Additive Manufacturing (AM) processes have complex non-equilibrium physical and chemical nature, which is material- and process-dependant. The complex non-equilibrium microstructure of the processed materials occurs as a result of solid-state phase transformations, evolution of non-equilibrium phases, refined microstructures and precipitation of non-equilibrium second-phase particles during manufacturing. Thus, this complex non-equilibrium microstructure, that occurs as a result of multiple modes of heat, mass, and momentum transfers induced by repeated localized laser scanning, dictate the microstructural integrity and properties of manufactured parts [115]. However, the properties of the manufactured parts can be tailored or improved using heat treatment techniques. In this discussion, the results of two materials are being considered (WC-Co &WC-Co-hBN). In both the WC-Co and WC-Co-hBN samples, it was observed that their as-printed samples had a complex microstructure including non-equilibrium phases. For example, the WC-Co material recorded the W_2C phase on the XRD pattern which is a high temperature phase [140][29]. In the WC-Co-hBN sample, BN is a stable phase but that was not identified using the X-ray analysis. However, other compounds such as CoWB were rather identified in the sample. On the microstructure, the predominant polyangular chips in these as-printed samples began to breakdown during heat treatment between 0 °C and 600 °C. This breakdown is as a result of the conversion of the non-equilibrium phases to more stable phases as was shown in the X-ray diffraction analysis. In the WC-Co samples, the W_2C polymorphs are stable at relatively high temperatures (>1250 °C) which accounts for the high-volume fraction of W_2C phases in the as-printed samples. It is inferred that the decomposition of the polyangular chips during heat treatment between 0 °C and 600 °C is as a result of the conversion of the high-temperature phase (W_2C phase) to a more stable WC phase including the evolution of other stable W-C-Co phases. Heat-treating the samples at and above 600 °C, results in the coalescence of the disintegrated polyangular chips resulting in coarser chips and grains. However, the evolved dendritic structures after 3D printing become coarser and more globular when heat-treated between 0 °C and 1000 °C due to the associated high temperatures. With

regards, to the WC-Co-hBN samples, the carbide grain sizes were much smaller than the grains in the WC-Co samples. The heat treatment affected the size and distribution of the carbide grains. The smaller grain sizes in the WC-Co-hBN samples have been attributed to the addition of the hBN material. This is because, the printing parameters and alloy composition percentages of the WC-Co-hBN material was the same as the WC-Co material. The only difference changing between the samples was the addition of the hBN sample. After heat treatment, the grain sizes of the WC chips disintegrated up to the 600°C temperature whereas during 800°C and 1000°C, coalescence of the grains was observed. It is therefore asserted that, both materials experience the same mechanism after heat treatment was applied to the microstructure. Conclusively, this manufacturing technique created a complex microstructure which had non-stable phases present. The heat treatment got rid of these phases as well as creation of stable phases. The carbide grains sizes of the WC-Co-hBN samples were smaller than the WC-Co samples.

5.2 Effect of Processing and Post Processing Heat Treatment on the Hardness Properties of the Material.

It has been shown that residual stresses build up during metal-based additive manufacturing of parts which can, in turn, degrade the microstructural integrity and properties of the manufactured part. In the WC-Co sample, the observed cracks are attributed to the build-up of high residual stresses in the parts during processing. The repeated heating and cooling during processing creates a temperature gradient within the samples resulting in the build-up of compressive and tensile stresses in the parts, especially between the layers of the build. This generates residual stresses in the part [128, 130]. However, the WC-Co-hBN sample had less microcracks in the sample and this was attributed to the addition of the hBN which is known to have high thermal shock resistance. During heat treatment of the as-printed WC-Co samples, there was a significant increase in hardness irrespective of the temperature of heat treatment. Typically, heat-treating as printed samples reduce the residual stresses which results in a decrease in the hardness of the samples. However, coupled with the breakdown of the polyangular chips during heat treatment, there was a significant reduction in the phase and grain sizes which ultimately resulted in the increase in hardness. The high hardness of the as-printed samples that was heat-treated at 600 °C is attributed to the breakdown of the polyangular chips and the increase in volume fraction and spatial

distribution of the observed W-C-Co phase. There exist different polymorphs of this "foggy" brittle regions which includes primarily W_2Co_4C, W_3Co_3C, and W_6Co_6C. The W_2Co_4C and W_3Co_3C are considered to be the most brittle phases [140]. The same attribution was made by Asl who reported better hardness for an ST37 mild steel substrate with a WC-Co coating after heat treatment. He attributed the hardness properties to the formation of hard eta phases(W-C-Co) [141]. The decrease in hardness for the samples heat-treated between 800 °C and 1000 °C is as a result of the coalescence of the polyangular chips, grain growth and the presence of W_6Co_6C phases which has relatively low hardness when compared with the other W-C/W-C-Co phases [128]. With regards to the WC-Co-hBN sample, there was a reduction the hardness. This was solely attributed to the relief of the residual stresses in the material. Additionally, comparing both materials, the high hardness values of the WC-Co-hBN material as compared to the WC-Co material was attributed to the smaller carbide grain sizes.

5.3 Effect of Processing and Post Processing Heat Treatment on the Fracture Toughness Properties of the Material.

The hardness properties of the 3D printed cemented carbides makes the adoption of the additive manufacturing method attractive and promising. Even though the relative hardness of the heat-treated specimens were usually higher than the as-printed samples, the general fracture toughness of the samples were significantly lower when compared to the fracture toughness of conventionally sintered WC-Co alloys [142–144]. However, the current values obtained for the fracture toughness of the as-printed and heat-treated WC-Co samples are relatively comparable to values reported in the literature for WC-Co coatings [145, 146]. Park reported similar values of fracture toughness for WC-Co alloy heat-treated at 800 °C using the indentation method [145]. Higher values were recorded for the WC-Co-hBN samples. Thus, the addition of the hBN also improves the fracture toughness of the samples. However, the lower fracture toughness values of both materials are attributed to the high volumes of porosity and micro-cracks in the as-printed samples. Fundamentally, Co phases in cemented carbides are responsible for imparting ductility to the material [147, 148]. However, the evolved phases, volume fraction, size and spatial distribution of the phases in addition to the level of porosity and micro-cracks determine the fracture properties of the 3D printed specimens. Improved fracture toughness in WC-Co alloy has also been attributed

to some ductile W-C-Co phases such as W_6Co_6C phase that evolve in the alloy during processing and heat treatment [145, 146]. Yao attributed the relatively high fracture toughness properties of a WC-Co alloy when heat-treated at 950 °C to the less brittle W_6Co_6C phase that evolved in the microstructure during heat treatment [146]. In the WC-Co material, the high fracture toughness recorded in the 600 °C sample is also attributed to the W_6Co_6C phases. This is because, the XRD pattern for the sample heat treated at 600 °C in Figure 8f showed two peaks of W_6Co_6C phase. These are probably the determining phases in the material contributing major percentage of ductility as compared to the pure cobalt rich regions which have decreased in volume fraction as the temperature of heat treatment increased.

5.4 Effect of Processing and Post Processing Heat Treatment on The Wear Properties of The Material.

Generally, the high wear resistance of WC-Co alloy systems has been attributed to the size and volume fraction of the WC monocarbide phases in the material [149–153]. This implies that having a high-volume fraction of the WC mono-carbide phase is desirable for high wear resistance. In the current study, the low wear rate of the sample heat-treated at 400 °C is attributed to the decomposition of the non-equilibrium W_2C phase to a more stable WC monocarbide phase [154], [155] as well as the bigger grain sizes of the WC monocarbide phases. The reduction in wear resistance of the samples heat treated between 400 °C and 1000 °C is attributed to the decrease in the volume fraction of the WC mono-carbide phase, coarsening and evolution of the W-C-Co phases within the samples. In the WC-Co-hBN samples, better wear properties were accounted which is attributed to the addition of the self lubricative material. All the WC-Co-hBN samples experienced a drastic increase in wear resistance. The WC-Co-hBN sample heat treated at 1000°C had the highest wear resistance. This is attributed to formation of the hexagonal BN phase captured in the XRD analysis of that sample. However, the other samples had W-C-Co, W-Co-N and CoWB phases rather forming. A summative assessment is carefully made that indeed the addition of the hBN increases the wear resistance of the material.

5.5 Applications: The Current Results in Adopting Metal-Additive Manufacturing for Cemented Carbides

Metal-Additive manufacturing is rising as the new era of manufacturing for products. There is no doubt that in the next two decades, all materials would be pushed t metal-additive manufacturing. One of the important materials that need to be considered is the cemented carbides because of its importance and application in high temperature applications and micro machining of other materials. Thus, products made from cemented carbides have intricate shapes which is very difficult and stressful to fabricate using the conventional manufacturing methods (Powder metallurgy). With this study, the printing, characterisation and post processing of the WC-Co cemented carbides was accomplished using WC-Co. Even though the cemented carbides presented unwanted mechanical properties after printing, the adoption of a one-step post processing treatment improved the mechanical properties of the material. This was attributed to the relief of residual stresses and the removal of non equilibrium phases and the tailoring of microstructure to have desired phases depending on the application of the material. The current study showed that the manufacturing method also presented defects such as porosity and micro cracks. This is already a problem with the manufacturing technique. Changing the processing parameters can only help reduce the frequency and size of pores that can be generated. Observations made from this study shows that the mechanical properties including wear and hardness which are very important for industrial applications are not specifically affected by the pores. However, for applications which require high fracture toughness qualities, it would not be advisable to opt for an additively manufactured cemented carbide. These results for WC-Co cemented carbides can be projected to other cemented carbide grades and ceramics which are yet to be adopted on the metal additive manufacturing stream. Thus, the results from the current study provide the knowledge and understanding to model and design materials that can be printed using metal additive manufacturing techniques as well as improve their mechanical properties by adopting a one step heat treatment process. Similarly, although the current results are specific to WC-17Co cemented carbide grades, a common experimental procedure can be employed to tailor microstructures of new materials and alloys that are lightweight.

Additionally, the current numerical models only tackle the modes of heat transfer and thermal conductivities. However, the data being used for these materials do not predict phases

transformations that can be used to predict the mechanical properties. The knowledge and understanding from this study can be used to develop theoretical and numerical models which consider these complex microstructures and better depict the microstructures of materials used for structural applications.

6 : CONCLUSION & FUTURE WORK

6.1 : Conclusions

Processing materials such as cemented carbides (WC-Co) processed using M-AM presents many challenges due to the material and complex mechanisms that occur during processing. Powder composition, processing parameters and post-processing treatments dictates the microstructural integrity and mechanical properties of the processed parts. In this study, Cemented carbides were processed using Selective Laser Sintering (SLS) and heat treated at 400 °C, 600 °C, 800 °C and 1000 °C for 3 hours to understand the effect of processing and post-processing heat treatment on the structure and properties of the WC-Co cemented carbide. A further analysis was made and a novel alloy composition bearing self lubricative properties was introduced. The same processing and post-processing heat treatment was adopted for this sample. It was revealed that the as-printed versions of both alloys had a microstructure with non-equilibrium phases which has been attributed to the repeated thermal cycles, large temperature gradients and relatively high cooling rates during solidification. A summary of the findings in the current study are as follows:

1. In the WC-17Co as-printed sample, four distinct microstructural features which included regular and irregular WC polyangular chips, W-C-Co phase dendritic structures, W-C-Co "foggy" (shapeless) regions and cobalt-rich background regions were observed. This was attributed to the repeated thermal cycles, large temperature gradients and relatively high cooling rates during solidification. The X-ray diffraction analysis showed that the as-printed specimen was made up of W_3Co_3C, W_2Co_4C, W_2C and the hexagonal WC phases.

2. After heat treatment of the as-printed WC-17Co sample at 400 °C, the regular and irregular polyangular W-C chips appeared to be well-developed and distinct when compared with those observed in the as-printed sample. Furthermore, there was an increase in the number of regular polyangular chips with reduced size as a result of decomposition of the unstable W_2C phase chips to the more stable WC chips. The X-ray diffraction analysis identified no new phase in addition to the existing phases found in the as-printed sample. However, the W_2Co_4C that was found in the as-printed sample was not present in this heat-treated sample.

3. After heat treatment of the as-printed WC-17Co sample at 600 °C, the general sizes of the regular and irregular chips had become smaller as a result of continues decomposition of the unstable W_2C phase chips to the more stable WC chips. Well-developed coarser and round dendritic structures were observed in this sample with a significant reduction in the volume fraction of the W-C-Co phase W-C-Co phase. The XRD diffraction patterns revealed a new WC-Co (W_6Co_6C) phase which was not observed in the other specimens.

4. After heat treatment of the as-printed WC-17Co sample at 800 °C, the volume fraction of the irregular polyangular WC chips was significantly higher than was observed in the other samples. There were agglomerations of globular precipitates within the darker cobalt-rich regions in addition to platelet WC chips. The XRD showed higher peak heights for the W-C-Co phases and a new $WC_{0.5}$ phase.

5. After heat treatment of the as-printed WC-17Co sample at 1000 °C, high temperature W-C and W-C-Co phases evolved in the sample. The relative sizes of the regular polyangular chips were smaller and well-developed with a higher volume fraction of pores within the W-C-Co phase. The XRD analysis showed a high reduction in the peak heights of some of the W-C phases when compared to the other samples. A new W-C-Co ($W_{10}Co_3C_4$) was identified in addition to a significant reduction in the peak intensity of the $WC_{0.5}$ phase.

6. The heat-treated WC-17Co samples had relatively higher hardness when compared to the as printed sample with the sample heat treated at 600 °C having the highest hardness as a result of the continued decomposition of the unstable W_2C phase chips to the more stable WC chips. In addition, this sample had the highest fracture toughness (8.37 MPa√m), representing a 34% increase in fracture toughness, when the sample was compared with the as-printed sample (6.23 MPa√m). The relatively high fracture toughness was attributed to the evolution of the ductile W_6Co_6C phase in the sample after heat treatment. It is concluded that post-processing heat treatment of SLS printed WC-

Co alloy at 600 °C can be used to improve the structure and mechanical properties of the alloy.

7. In the as-printed WC-Co-hBN sample, a similar structure just like the as-printed WC-Co sample was observed. This included the polyangular chips (irregular and regular), "foggy" (shapeless) regions and dark background regions. Additionally, the grain sizes of the WC-Co-hBN samples were smaller than the WC-17Co samples. However, dendritic structures that were observed on WC-17Co were however not present on this sample. The structures were still identified as WC chips, W-C-Co "foggy" (shapeless) regions and cobalt-rich background regions from the EDS analysis. The observation of B and N was difficult due to the low volume fraction of material added however, the EDS mapping shown an even distribution of the B and N across the sample. This complex microstructure was also attributed to the repeated thermal cycles, large temperature gradients and relatively high cooling rates during solidification. The X-ray diffraction analysis showed that the as-printed specimen was made up of W_3Co_3C, W_3Co_3N, $W_9Co_3C_4$, CoWB, $Co_{5.47}N$ and the hexagonal WC phases. W_2C was not identified in the XRD pattern of this sample and this can be attributed to the added hBN which possess a high resistance to thermal shock. Thus, during printing, it is presumed that, this repeated and irregular thermal gradient creates thermal shock and the hBN material available in the WC-Co absorbed the thermal shock and the rapid cooling and solidification could not occur which and thus unstable W_2C phase could not be formed.

8. After heat treatment of the as-printed WC-Co-hBN sample at 400 °C, no new structures were observed in the sample however, the already existing structures had undergone a few changes. The sizes of these structures varied as compared to as-printed sample. The regular and irregular polyangular WC chips appeared to be smaller than the as-printed sample. Even though bigger chips were also observed which were not in the as printed sample, the volume fraction of the smaller WC chips was higher than the volume fraction of the WC chips with bigger sizes. The X-ray diffraction analysis identified no new phase in addition to the existing phases found in the as printed sample. But, the peak intensities of the WC phases had reduced.

9. After heat treatment of the as-printed WC-Co-hBN sample at 600 °C, the general sizes of the regular and irregular chips had become smaller and the bigger WC chips were broken down. A few of these bigger chips could be found on this sample. The foggy regions in this material had become well developed. The XRD diffraction pattern revealed just one W_3Co_3N phase whiles a lot of W_3Co_3C phases which were not there were now present. The intensities of the WC phase had reduced drastically as compared to the as printed WC-Co-hBN sample.

10. After heat treatment of the as-printed WC-Co-hBN sample at 800 °C, there was drastic depletion in the Co rich regions, and most WC chips were very big and are coalescing with other WC chips. the volume fraction of the irregular polyangular WC chips was significantly higher than was observed in the other samples. The XRD showed higher peak heights for the W-C-Co phases including the new W_3Co_3C phases that had been observed in the previous sample. The intensities of the W-C-Co phases were primarily larger than that of the ones in the as-printed sample.

11. After heat treatment of the as-printed WC-Co-hBN sample at 1000 °C, high temperature W-C and W-C-Co phases evolved in the sample. The relative sizes of the regular polyangular chips were very big with few Co rich regions. The foggy regions seem to have become well developed and had WC chips embedded in them. The XRD analysis showed a high reduction in the peak heights of some of the W-C phases when compared to the other samples. A new phase which is the hexagonal BN was identified in addition to a significant reduction in the peak intensity of the WC phase.

12. The heat-treated WC-Co-hBN samples had relatively higher hardness when compared to the as-printed WC-17Co samples. The hardness value of the as-printed WC-Co-hBN was 3 times higher than the WC-17Co as-printed sample. However, the heat treatment process applied to the WC-Co-hBN samples decreased the hardness of the material. The reduction was attributed to the heat treatment relieving residual stresses and eliminating non-equilibrium phases and therefore softens the microstructure of the

material. In addition, this as-printed sample had the highest fracture toughness (7.82 MPa√m), which was also higher than the fracture toughness of most of the WC-17Co samples. The was not any peculiar trend in the effect of the heat treatment on the fracture toughness of the material. However, the low values as compared to the conventional manufactured samples where attributed to the unescapable porosity induced in the M-AM samples. It is concluded that post-processing heat treatment of SLS printed WC-Co-hBN alloys provide good mechanical properties and this heat treatment at 1000 °C can be used to improve the structure and mechanical properties of the alloy.

13. The wear properties of the WC-Co-hBN samples were observed to be better as compared to the WC-17Co samples. The best wear properties were identified in the WC-Co-hBN sample heat treated at 1000°C. This was attributed to the formation of the hexagonal BN phase captured on the XRD pattern. hBN is known to possess self lubricative properties and this is what made the sample more resistant to wear than all the samples.

6.2. Future Work

There are still lots of work that should be done to increase the mechanical properties and microstructural integrity of the 3D printed parts. There are already some limitations in this research work which should be eliminated in the future research to produce more accurate mechanical strength prediction and failure mechanism results for 3D printed parts. For example, the fracture toughness was gotten using indentation method, however, 3-point bend test samples can be printed to undertake fracture toughness test using single edge notched beam test. The results from that experiment can be trusted much more for the fracture toughness than using indentation method. This research mostly focused on creating the base work to continue the research in the field, so a select range of processing parameters were used to print samples as well as tested and analyzed. However, selecting a wide variety of different parameters which has effect on the strength and failure conditions observed during the research will help to deduce more strong conclusions.

Advanced microscopic techniques which will include Transmission Electron Microscopy (TEM) can de adopted to understand the crystallographic properties of the material and how they are affected by the processing and post-processing treatments. Hence, the outcomes of the result can be broadened. Also, there are few other areas where the research has left untouched. The effect of the processing on other load bearing characteristics such as tensile, compressive and dynamic properties of the material. Even though, standard procedures have not been outlines or established. An acceptable and novel technique can be created and used to make such experiments possible for analysis of 3D printed materials. It sounds challenging, but more research and attempt can produce positive results. There is never an end to the research work in any field, and this is just the beginning and small part of the research in strength and failure mechanism for 3D printed parts. The author is hopeful that the outcome of this research will provide as the base work for the future studies.

7. REFERENCES

[1] D. Apelian, “Particulate Processing (Powder Metallurgy),” K. H. J. Buschow, R. W. Cahn, M. C. Flemings, B. Ilschner, E. J. Kramer, S. Mahajan, and P. B. T.-E. of M. S. and T. Veyssière, Eds. Oxford: Elsevier, 2001, pp. 6761–6768.

[2] F. Wakai, G. Okuma, and N. Nishiyama, “Sintering mechanics of ceramics: a short review,” Mater. Today Proc., vol. 16, pp. 4–13, 2019.

[3] K. Sanjay, “Optimization of parameters for SLS of WC-Co,” Rapid Prototyping Journal, vol. 23, no. 6, pp. 1202–1211, Jan. 2017.

[4] Victoria, “Proceedings of the 26th Canadian Congress of Applied Mechanics,” vol. 2, on. June 2017.

[5] S. A. M. Tofail, E. P. Koumoulos, A. Bandyopadhyay, S. Bose, L. O’Donoghue, and C. Charitidis, “Additive manufacturing: scientific and technological challenges, market uptake and opportunities,” Mater. Today, vol. 21, no. 1, pp. 22–37, 2018.

[6] H. Sahasrabudhe, S. Bose, and A. Bandyopadhyay, “Chapter 17 - Laser-Based Additive Manufacturing Processes,” in Woodhead Publishing Series in Welding and Other Joining Technologies, J. B. T.-A. in L. M. P. (Second E. Lawrence, Ed. Woodhead Publishing, 2018, pp. 507–539.

[7] ASTM INTERNATIONAL, “ASTM F2792-12a,” Rapid Manuf. Assoc., pp. 1–3, 2013.

[8] K. Bartkowiak, S. Ullrich, T. Frick, and M. Schmidt, “New developments of laser processing aluminium alloys via additive manufacturing technique,” Phys. Procedia, vol. 12, no. PART 1, pp. 393–401, 2011.

[9] S. Shimizu, H. T. Fujii, Y. S. Sato, H. Kokawa, M. R. Sriraman, and S. S. Babu, “Mechanism of weld formation during very-high-power ultrasonic additive manufacturing of Al alloy 6061,” Acta Mater., vol. 74, pp. 234–243, 2014.

[10] K. Schmidtke, F. Palm, A. Hawkins, and C. Emmelmann, “Process and mechanical properties: Applicability of a scandium modified Al-alloy for laser additive manufacturing,” Phys. Procedia, vol. 12, no. PART 1, pp. 369–374, 2011.

[11] R. Chou, J. Milligan, M. Paliwal, and M. Brochu, “Additive Manufacturing of Al-12Si Alloy Via Pulsed Selective Laser Melting,” J.O.M., vol. 67, no. 3, pp. 590–596, 2015.

[12] M. Drahansky et al., “We are Intech Open , the world ’ s leading publisher of Open Access books Built by scientists , for scientists TOP 1 %,” Intech, vol. i, no. tourism, p. 13, 2016.

[13] E. Uhlmann, R. Kersting, T. B. Klein, M. F. Cruz, and A. V. Borille, “Additive Manufacturing of Titanium Alloy for Aircraft Components,” Procedia CIRP, vol. 35, pp. 55–60, 2015.

[14] Y. Zhu, X. Tian, J. Li, and H. Wang, “The anisotropy of laser melting deposition additive manufacturing Ti–6.5Al–3.5Mo–1.5Zr–0.3Si titanium alloy,” Mater. Des., vol. 67, pp. 538–542, 2015.

[15] Y. Zhu, J. Li, X. Tian, H. Wang, and D. Liu, “Microstructure and mechanical properties of hybrid fabricated Ti–6.5Al–3.5Mo–1.5Zr–0.3Si titanium alloy by laser additive manufacturing,” Mater. Sci. Eng. A, vol. 607, pp. 427–434, 2014.

[16] B. Dutta and F. H. Froes, “Chapter 1 - The Additive Manufacturing of Titanium Alloys,” B. Dutta and F. H. B. T.-A. M. of T. A. Froes, Eds. Butterworth-Heinemann, 2016, pp. 1–10.

[17] T. Wang, Y. Y. Zhu, S. Q. Zhang, H. B. Tang, and H. M. Wang, “Grain morphology evolution behavior of titanium alloy components during laser melting deposition additive manufacturing,” J. Alloys Compd., vol. 632, pp. 505–513, 2015.

[18] S. Gorsse, C. Hutchinson, M. Gouné, and R. Banerjee, “Additive manufacturing of metals: a brief review of the characteristic microstructures and properties of steels, Ti-6Al-4V and high-entropy alloys,” Sci. Technol. Adv. Mater., vol. 18, no. 1, pp. 584–610, 2017.

[19] Z. Wang, T. A. Palmer, and A. M. Beese, “Effect of processing parameters on microstructure and tensile properties of austenitic stainless steel 304L made by directed energy deposition additive manufacturing,” Acta Mater., vol. 110, pp. 226–235, 2016.

[20] A. Zadi-Maad, R. Rohib, and A. Irawan, “Additive manufacturing for steels: A review,” IOP Conf. Ser. Mater. Sci. Eng., vol. 285, no. 1, 2018.

[21] J.-P. Järvinen et al., “Characterization of Effect of Support Structures in Laser Additive Manufacturing of Stainless Steel,” Phys. Procedia, vol. 56, pp. 72–81, 2014.

[22] A. S. Wu, D. W. Brown, M. Kumar, G. F. Gallegos, and W. E. King, “An Experimental Investigation into Additive Manufacturing-Induced Residual Stresses in 316L Stainless Steel,” Metall. Mater. Trans. A, vol. 45, no. 13, pp. 6260–6270, 2014.

[23] A. Zocca, P. Colombo, C. M. Gomes, and J. Günster, “Additive Manufacturing of Ceramics: Issues, Potentialities, and Opportunities,” J. Am. Ceram. Soc., vol. 98, no. 7, pp. 1983–2001, 2015.

[24] V. Ocelík, N. Janssen, S. N. Smith, and J. T. M. De Hosson, "Additive Manufacturing of High-Entropy Alloys by Laser Processing," Jom, vol. 68, no. 7, pp. 1810–1818, 2016.

[25] S. Das, M. Wohlert, J. J. J. Beaman, and D. L. L. Bourell, "Processing of titanium net shapes by SLS/HIP," Mater. Des., vol. 20, no. 2–3, pp. 115–121, 1999.

[26] S. Das, M. Wohlert, J. J. Beaman, and D. L. Bourell, "Producing metal parts with selective laser sintering/hot isostatic pressing," JOM, vol. 50, no. 12, pp. 17–20, 1998.

[27] R. Wauthle et al., "Additively manufactured porous tantalum implants," Acta Biomater., vol. 14, pp. 217–225, 2015.

[28] M. Kanazawa, M. Iwaki, S. Minakuchi, and N. Nomura, "Fabrication of titanium alloy frameworks for complete dentures by selective laser melting," J. Prosthet. Dent., vol. 112, no. 6, pp. 1441–1447, 2014.

[29] T. Hayashi, K. Maekawa, M. Tamura, and K. Hanyu, "Selective laser sintering method using titanium powder sheet toward fabrication of porous bone substitutes," JSME Int. Journal, Ser. A Solid Mech. Mater. Eng., vol. 48, no. 4, pp. 369–375, 2006.

[30] M. A. Stoodley, J. R. Abbott, and D. A. Simpson, "Titanium cranioplasty using 3-D computer modelling of skull defects," J. Clin. Neurosci., vol. 3, no. 2, pp. 149–155, 1996.

[31] E. O. Olakanmi, R. F. Cochrane, and K. W. Dalgarno, "A review on selective laser sintering/melting (SLS/SLM) of aluminium alloy powders," Prog. Mater. Sci., vol. 74, pp. 401–477, 2015.

[32] L. E. Murr et al., "Metal Fabrication by Additive Manufacturing Using Laser and Electron Beam Melting Technologies," J. Mater. Sci. Technol., vol. 28, no. 1, pp. 1–14, 2012.

[33] T. Mahale, D. Cormier, O. Harrysson, and K. Ervin, "Advances In electron beam melting of aluminum alloys," 18th Solid Free. Fabr. Symp. SFF 2007, pp. 312–323, 2007.

[34] F. Khodabakhshi and A. P. Gerlich, "Potentials and strategies of solid-state additive friction-stir manufacturing technology: A critical review," J. Manuf. Process., vol. 36, pp. 77–92, 2018.

[35] W. J. Sames, F. A. List, S. Pannala, R. R. Dehoff, and S. S. Babu, "The metallurgy and processing science of metal additive manufacturing," Int. Mater. Rev., vol. 61, no. 5, pp. 315–360, Jul. 2016.

[36] R. P. Mudge and N. R. Wald, "Laser engineered net shaping advances additive manufacturing and repair," Weld. J. (Miami, Fla), vol. 86, no. 1, pp. 44–48, 2007.

[37] S. W. Williams, F. Martina, A. C. Addison, J. Ding, G. Pardal, and P. Colegrove, "Wire + Arc Additive Manufacturing," Mater. Sci. Technol., vol. 32, no. 7, pp. 641–647, May 2016.

[38] P. Åkerfeldt, R. Pederson, and M.-L. Antti, “A fractographic study exploring the relationship between the low cycle fatigue and metallurgical properties of laser metal wire deposited Ti–6Al–4V,” Int. J. Fatigue, vol. 87, pp. 245–256, 2016.

[39] F. Khodabakhshi, M. H. Farshidianfar, S. Bakhshivash, A. P. Gerlich, and A. Khajepour, “Dissimilar metals deposition by directed energy based on powder-fed laser additive manufacturing,” J. Manuf. Process., vol. 43, pp. 83–97, 2019.

[40] S. Wolff, T. Lee, E. Faierson, K. Ehmann, and J. Cao, “Anisotropic properties of directed energy deposition (DED)-processed Ti–6Al–4V,” J. Manuf. Process., vol. 24, pp. 397– 405, 2016.

[41] S. Shao, M. J. Mahtabi, N. Shamsaei, and S. M. Thompson, “Solubility of argon in laser additive manufactured α-titanium under hot isostatic pressing condition,” Comput. Mater. Sci., vol. 131, pp. 209–219, 2017.

[42] S. Tammas-Williams, P. J. Withers, I. Todd, and P. B. Prangnell, “Porosity regrowth during heat treatment of hot isostatically pressed additively manufactured titanium components,” Scr. Mater., vol. 122, pp. 72–76, 2016.

[43] M. Seifi, A. A. Salem, D. P. Satko, U. Ackelid, S. L. Semiatin, and J. J. Lewandowski, “Effects of HIP on microstructural heterogeneity, defect distribution and mechanical properties of additively manufactured EBM Ti-48Al-2Cr-2Nb,” J. Alloys Compd., vol. 729, pp. 1118–1135, 2017.

[44] P. Shakor, S. Nejadi, G. Paul, and S. Malek, “Review of emerging additive manufacturing technologies in 3d printing of cementitious materials in the construction industry,” Front. Built Environ., vol. 4, no. January 2019.

[45] A. International, “ASTM C1161 - Standard Test Method for Flexural Strength of Advanced Ceramics at Ambient Temperature,” ASTM Int., pp. 1–19, 2013.

[46] T. Himmer, A. Techel, S. Nowotny, and E. Beyer, “Recent developments in Metal Laminated Tooling,” 24th Int. Congr. Appl. Lasers Electro-Optics, ICALEO 2005 - Congr. Proc., pp. 304–309, 2005.

[47] S. Yi, F. Liu, J. Zhang, and S. Xiong, “Study of the key technologies of LOM for functional metal parts,” J. Mater. Process. Technol., vol. 150, no. 1, pp. 175–181, 2004.

[48] T. Himmer, T. Nakagawa, and M. Anzai, “Lamination of metal sheets,” Comput. Ind., vol. 39, no. 1, pp. 27–33, 1999.

[49] S. Pop, “3D Printing Starts Using Metal in European Space Agency Project,” 2013. [Online]. Available: https://news.softpedia.com/news/3D-Printing-Starts-Using-Metal-inEuropean-Space-Agency-Project-391603.shtml. [Accessed: 19-Nov-2019].

[50] “3D printed metal part.”. Accessed online

[51] C. Li, Z. Y. Liu, X. Y. Fang, and Y. B. Guo, “Residual Stress in Metal Additive Manufacturing,” Procedia CIRP, vol. 71, pp. 348–353, 2018.

[52] G. N. Levy, R. Schindel, and J. P. Kruth, “Rapid Manufacturing and Rapid Tooling with Layer Manufacturing (Lm) Technologies, State of The Art and Future Perspectives,” CIRP Ann., vol. 52, no. 2, pp. 589–609, 2003.

[53] J. P. Kruth, J. Deckers, E. Yasa, and R. Wauthlé, “Assessing and comparing influencing factors of residual stresses in selective laser melting using a novel analysis method,” Proc. Inst. Mech. Eng. Part B J. Eng. Manuf., vol. 226, no. 6, pp. 980–991, 2012.

[54] I. Yadroitsev and I. Yadroitsava, “Evaluation of residual stress in stainless steel 316L and Ti6Al4V samples produced by selective laser melting,” Virtual Phys. Prototyp., vol. 10, no. 2, pp. 67–76, Apr. 2015.

[55] T. Mishurova et al., “An assessment of subsurface residual stress analysis in SLM Ti-6Al4V,” Materials (Basel)., vol. 10, no. 4, 2017.

[56] S. D. Bagg, L. M. Sochalski-Kolbus, and J. R. Bunn, “The effect of laser scan strategy on distortion and residual stresses of arches made with selective laser melting,” Proc. - ASPE/euspen 2016 Summer Top. Meet. Dimens. Accuracy Surf. Finish Addit. Manuf., pp. 133–138, 2016.

[57] G. Todd, “First Surface Oberflächentechnik GmbH: EOS and BESTinCLASS Found Joint Venture for the German-speaking Market,” 2011. [Online]. Available: https://www.engineering.com/3DPrinting/3DPrintingArticles/ArticleID/4042/FirstSurface Oberflachentechnik-GmbH-EOS-and-BESTinCLASS-Found-Joint-Venture-forthe-German-speaking-Market.aspx.

[58] P. E. R. Carlsson, Surface-engeneering-in-sheet-metal-forming. 2005.

[59] H. P. Tang, M. Qian, N. Liu, X. Z. Zhang, G. Y. Yang, and J. Wang, “Effect of Powder Reuse Times on Additive Manufacturing of Ti-6Al-4V by Selective Electron Beam Melting,” Jom, vol. 67, no. 3, pp. 555–563, 2015.

[60] J. P. J. De Jong and E. De Bruijn, “Innovation Lessons From 3-D Printing,” MIT Sloan Manag. Rev., vol. 52, no. 2, pp. 43–52, 2013.

[61] L. Chen, Y. He, Y. Yang, S. Niu, and H. Ren, “The research status and development trend of additive manufacturing technology,” Int. J. Adv. Manuf. Technol., vol. 89, no. 9–12, pp. 3651–3660, 2017.

[62] G. F. King W. E. , Barth H. D., Castillo V. M. and K. C. R. A. M. Gibbs J. W., HahnD. E., “Observation of keyhole-mode laser melting in laser powder-bed fusion additive manufacturing,” J. Mater. Process. Technol., vol. 214, pp. 2915–2925, 2014.

[63] W. E. Frazier, “Metal additive manufacturing: A review,” J. Mater. Eng. Perform., vol. 23, no. 6, pp. 1917–1928, 2014.

[64] T. Vilaro, C. Colin, and J. D. Bartout, “As-fabricated and heat-treated microstructures of the Ti-6Al-4V alloy processed by selective laser melting,” Metall. Mater. Trans. A Phys. Metall. Mater. Sci., vol. 42, no. 10, pp. 3190–3199, 2011.

[65] P. A. Kobryn, E. H. Moore, and S. L. Semiatin, “The effect of laser power and traverse speed on microstructure, porosity, and build height in laser-deposited Ti-6Al-4V,” Scr. Mater., vol. 43, no. 4, pp. 299–305, 2000.

[66] L. N. Carter, M. M. Attallah, and R. C. Reed, “Laser powder bed fabrication of nickelbase superalloys: influence of parameters; characterisation, quantification and mitigation of cracking,” Superalloys 2012, pp. 577–586, 2012.

[67] What is hot cracking (solidification cracking)? 2015. .

[68] W. J. Sames, F. Medina, W. H. Peter, S. S. Babu, and R. R. Dehoff, “Effect of Process Control and Powder Quality on Inconel 718 Produced Using Electron Beam Melting,” 8th International Symposium on Superalloy 718 and Derivatives. pp. 409–423, 11-Nov-2014.

[69] Locker Anatol, “Warp: Finally, there’s a Way to Measure it,” Warp-Index White Paper, 2018. [Online]. Available: https://all3dp.com/warp-finally-theres-way-measure/.

[70] J. V. H. L. Thijs, K. Kempen, J. P. Kruth, “Fine-structured aluminium products with controllable texture by SLM of pre-alloyed AlSi10Mg powder,” Acta Mater., vol. 61, no. 1809–1819, 2013.

[71] B. Wysocki, P. Maj, R. Sitek, J. Buhagiar, J. K. Kurzydłowski, and W. Święszkowski, Laser and Electron Beam Additive Manufacturing Methods of Fabricating Titanium Bone Implants,” Applied Sciences , vol. 7, no. 7. 2017.

[72] V. S. Sufiyarov and E. V Borisov, “Effect of Heat Treatment Modes on the Structure and Properties of Alloy VT6 After Selective Laser Melting,” Met. Sci. Heat Treat., vol. 60, no. 11, pp. 745–748, 2019.

[73] P. Prabhakar, W. J. Sames, R. Dehoff, and S. S. Babu, “Computational modeling of residual stress formation during the electron beam melting process for Inconel 718,” Addit. Manuf., vol. 7, pp. 83–91, 2015.

[74] N. Ku, J. J. Pittari, S. Kilczewski, and A. Kudzal, “Additive Manufacturing of Cemented Tungsten Carbide with a Cobalt-Free Alloy Binder by Selective Laser Melting for HighHardness Applications,” Jom, vol. 71, no. 4, pp. 1535–1542, 2019.

[75] Z. Ke et al., “Microstructure and mechanical properties of dual-grain structured WC-Co cemented carbides,” Ceram. Int., vol. 45, no. 17, Part A, pp. 21528–21533, 2019.

[76] N. Al-Aqeeli, N. Saheb, T. Laoui, and K. Mohammad, “The synthesis of nanostructured WC-based hardmetals using mechanical alloying and their direct consolidation,” J. Nanomater., vol. 2014, 2014.

[77] J. García, V. Collado Ciprés, A. Blomqvist, and B. Kaplan, “Cemented carbide microstructures: a review,” Int. J. Refract. Met. Hard Mater., vol. 80, no. August 2018, pp. 40–68, 2019.

[78] S. Lay, C. H. Allibert, M. Christensen, and G. Wahnstroem, “Morphology of WC grains in WC-Co alloys,” Mater. Sci. Eng. A, Struct. Mater. Prop. Microstruct. Process., vol. 486, no. 1–2, pp. 253–261.

[79] B. Roebuck and E. A. Almond, “Deformation and fracture processes and the physical metallurgy of WC–Co hardmetals,” Int. Mater. Rev., vol. 33, no. 1, pp. 90–112, Jan. 1988.

[80] A. S. Kurlov and A. I. Gusev, “Tungsten carbides and W-C phase diagram,” Inorg. Mater., vol. 42, no. 2, pp. 121–127, 2006.

[81] Z. B. Butorina, L. N., Piskner, “Kristallografya of Cemented Carbides,” Kristallografya, vol. 5, p. 585, 1960.

[82] C. B. Pollock and H. H. Stadelmaier, “The eta carbides in the Fe-W-C and Co-W-C systems, Metall. Trans., vol. 1, no. 4, pp. 767–770, 1970.

[83] F. Kellner, “Korrosionsverhalten und – mechanismen von Hartmetallen mit unterschiedlicher mikrostruktureller Längenskala,” pp. 1–176, 2010.

[84] B. Kaplan, Experimental and theoretical study of carbides in the Co-Cr-C system. 2014.

[85] A. T. Santhanam, “Metallography of Cemented Carbides,” Metallography and Microstructures, vol. 9. ASM International, p. 0, 01-Dec-2004.

[86] Kara, A., Nishikawa, T., and Nishimoto, T.,” Powder Metall., vol. 16, p. 310, 1970.

[87] Rudiger, O., and Exner, H. E.,” Powder Metall. Int., vol. 8, p. 7, 1976.

[88] J. of R. Lisovsky, A. F., Tkachenko, N. Y., and Kebko, V. and p. 33 (1991) Metals and Hard Materials, Vol. 10,

[89] Zhengi, T., Int. J. of Refractory Metals and Hard Materials, Vol. 9 and (1990),

[90] S. of H. Hellsing, M., Henjered, A., Norden, H., and Andren, H. O., E. . Materals, (R. K. Viswanadham, D. J. Rowcliffe, and J. Gurland, and p. 93 (1983) Plenum Prss, New York,

[91] (1978) Johansson, T., Uhrenius, B., Met. ScL, Vol. 12,

[92] H. E. Freytag, J., and Exner, "WC-Co Cermets Microstructures," in Mod. Dev. Powd. Met., Proc. Int. Powd. Met. Conf,Vol. 10, p. 511, 1977.

[93] "Hoffmann, A., and Mohs, R., Metall, Vol. 28, p. 661 (1974)."

[94] "Johnsson, H., Powd. Met, Vol. 15, No. 29, p. 1 (1972."

[95] "Lai, Ho-Yi and Jinhui, Y., Proc. llth Int. Plansee Sem., (H. Bildstein, and H. M. Ortner, eds.), Metallwerk Plansee, Reutte, Austria, Vol. 2, p. 679 (1985)."

[96] "Paltov, A. B., Hard Alloys, Sb. Tr. Nauchn. Issled. Inst. Tverd, Splav., Vol. 2, Metallurgizdt, Moscow, p. 82 (1960)."

[97] "Kreimer, G. S., Tumanov, V. L, Damenskaya, D. S., and Pavlova, Z. L, Fiz. Metal, i. Metalloved, Vol. 17, No. 4, p. 572 (1964)."

[98] "Gurland, J., and Bradzil, P., Trans. Met. Soc. AIME, Vol., 203, p. 311 (1955)."

[99] "Chatfield, C., Powd. Met. Int., Vol. 17, No. 3, p. 113 (1985)."

[100] "Lee, M. Y., Met. Trans. A, Vol. 14A, p. 1625 (1983)."

[101] "Dusja, J., Parilak, L., and Slesar, M., Ceramic International, Vol. 13,No. 3, p. 133 (1987)."

[102] "Warren, R., and Johanesson, B., Sintered Metal Ceramic Composites, Proc. 3rd Int. School on Sintered Mat., (Upadhyaya, G. S., eds.), Elsevier, Amsterdam, p. 365 (1984)."

[103] Novikov, N. V., Majstrenko, A. L., Konovalenko,N. K., and Uljanenko,A. P., Proc. Int. Powd. Met. Conf., Florence, Italian Metallurgical Soc., Milan, p. 685 (1982)."

[104] "Larsen-Basse, J., /. of Met., Vol.35, p. 133 (1983)."

[105] "Larsen-Basse, J., and Koyanagi, E. T., Trans. ASME, Vol. 101, p. 208 (1979)."

[106] "Larsen-Basse, J., Science of Hard Mat. (R. K. Viswanadham, DJ. Rowcliffe, and J. Gurland, eds.), Plenum Press, N.Y.,p. 797 (1983)."

[107] "Peters, C. T., and Brabyn, S. M., ibid, p. 877."

[108] "Reznik, L. A., Proc. World Conference on Powder Metallurgy PM '9O, Vol. 3, Institute of Materials, London, p. 272 (1990)."

[109] “Some Plain Talk about Carbides, Adamas Carbide Corporation, American Machinist, (May 1978.”

[110] U. Scheithauer et al., “Droplet-based additive manufacturing of hard metal components by thermoplastic 3D Printing (T3DP),” J. Ceram. Sci. Technol., vol. 8, no. 1, pp. 155–160, 2017.

[111] F. H. Kim and S. P. Moylan, “Literature Review of Metal Additive Manufacturing Defects,” NIST Adv. Manuf. Ser., pp. 100–116, 2018.

[112] O. F. Science, “(12) Patent Application Publication (10) Pub . No .: US 2016 / 0271610 A1 Patent Application Publication,” vol. 1, no. 19, 2016.

[113] F. Breu, S. Guggenbichler, and J. Wollmann, “Three-Dimensional Printing of Tungsten Carbide-Cobalt using a Cobalt Oxide Precursor,” Solid Free. Fabr. Symp., vol. 13, pp. 616–631, 2003.

[114] A. V. Khmyrov, R. S., Safronov, V. A., Gusarov, “Obtaining crack-free WC-Co alloys by selective laser melting,” Phys. Procedia, vol. 83, pp. 874–881, 2016.

[115] D. T. Zuback J. S., “The Hardness of Additively Manufactured Alloys,” Materials (Basel)., pp. 1–41, 2018.

[116] W. Gu, D., Meiners, “Microstructure characteristics and formation mechanisms of in situ WC cemented carbide based hard-metals prepared by selective laser melting,” Mater. Sci. Eng. A, vol. 527, pp. 7585–7592, 2010.

[117] Y. Gu, D., Shen, “Direct laser sintered WC-10Cu/Co nanocomposites,” Appl. Surf. Sci., vol. 254, pp. 3971–3978, 2008.

[118] Y. Gu, D., Shen, Y., Zhao, L., Xiao, J., Wu, P., Zhu, “Effect of rare earth oxide addition on microstructures of ultra-fine WC-Co particulate reinforced Cu matrix composites prepared by direct laser sintering,” Mater. Sci. Eng. A, vol. 445–446, pp. 316–322, 2007.

[119] Y. Gu, D., Shen, “WC-Co particulate reinforcing Cu matrix composites prepared by direct laser sintering,” Mater. Lett., vol. 60, pp. 3664–3668, 2006.

[120] M. C. Gu, D., Shen, Y., Dai, P., Yang, “Microstructure and property of sub-micro WC10%Co particulate reinforced Cu matrix composites prepared by selective laser sintering,” Trans. Nonferrous Met. Soc. China, vol. 16, pp. 357–362, 2006.

[121] K. Sanjay, “Manufacturing of WC-Co moulds using SLS machine,” J. Mater. Process. Technol., vol. 209, pp. 3840–3848, 2009.

[122] E. Uhlmann, A. Bergmann, and W. Gridin, “Investigation on Additive Manufacturing of Tungsten Carbide-cobalt by Selective Laser Melting,” Procedia CIRP, vol. 35, pp. 8–15, 2015.

[123] A. Kumar, S., Czekanski, “Development of WC-Co tool by additive manufacturing,” in Canadian Congress of Applied Mechanics (CANCAM).

[124] A. M. R. Fernandes, C. M., Senos, “Cemented carbide phase diagrams: A review,” Int. J. Refract. Met. Hard Mater., vol. 29, pp. 405–418, 2011.

[125] “V.F. Funke, A. N. Shurshakov, et al., Fiz. Metal and Metal alloyed., Vol. 10_2207 (1960).”

[126] “Tumanov V. I., Funke V. F., Trukhanova Z. S., Novikova T. A., Kuznetsova K. F., ‘The Heat Treatment of Tungsten Carbide-Cobalt Alloys’, All-Union Scientific Research Institute of Hard Alloys, No. 2(20), pp. 57-60.”

[127] “S. K. Asl, M. H. Sohi, K. Hokamoto and M. Uemura: ‘Effect of heat treatment on wear behavior of HVOF thermally sprayed WC-Co coatings’, Wear, 260, (11–12), 1203–1208.”

[128] “D.A. Stewart, P.H. Shipway, and D.G. McCartney,’Influence of heat treatment on the abrasive wear behaviour of HVOF sprayed WC-Co coatings’, Surface and Coatings Technology, Vol. 105, (1998), pp. 13-24.”

[129] “Zafar, S., Sharma, A. K., ‘Microstructure and wear performance of heat-treated WC-12 Co microwave clad’, Vacuum, Vol. 131, (2016), pp. 213-222.”

[130] “Wang, Q., Li, L., Yang, G., Zhao, X., Ding, Z., ‘Influence of heat treatment on the microstructure and performance of high-velocity oxyfuel sprayed WC-12Co coatings’, Surface & Coatings Technology, Vol. 206, (2012), pp. 4000-4010.”

[131] Zheng Y. T., Li H. B., Zhou T.,’Microstructure and mechanical properties of h_BN-SiC ceramic composites prepared by in situ combustion synthesis’, Material Science and Engineering A, (2012), Vol: 540, pp. 102-106.”

[132] B. Yaman and H. Mandal, “Wear performance of spark plasma sintered Co/WC and cBN/Co/WC composites,” Int. J. Refract. Met. Hard Mater., vol. 42, no. January, pp. 9– 16, 2014.

[133] “Rong HY, Peng ZJ, Ren XY, Wang CB, Fu ZQ, Qi LH, Miao HZ (2011) Microstructure and mechanical properties of ultrafine WC-Ni-VC-TaC-cBN cemented carbides fabricated by spark plasma sintering. Int J Refract Met Hard Mater 29:733–738.”

[134] J. Wachowicz, T. Truszkowski, M. Rosiński, M. Ossowski, G. Skrabalak, and M. Cyrankowski, “Tribological properties of WCCO/CBN composites produced by pulse plasma sintering,” Arch. Metall. Mater., vol. 63, no. 4, pp. 1763–1768, 2018.

[135] "Jonke, M., Klunsner, T. et al., 'Strength of WC-Co hard metals as a function of the effectively loaded volume.', International Journal of Refractory Metals and Hard Materials, Vol. 64, (2017), pp. 219-224."

[136] "Sergejev, F., Antonov, M., 'Comparative study on indentation fracture toughness measurements of cemented carbides', Proceedings of Estonian Academic Science Engineering, Vol. 12(4), (2006), pp. 388-398."

[137] "https://www.eos.info/material-m."

[138] "Shetty, D. K., 'Indentation fracture of WC-Co cermets', Journal of Materials Science, Vol. 20, pp. 1873-1882."

[139] "Spiegler, R et al. 1990, 'Fracture toughness evaluation of WC-Co alloys by indentation testing', Journal of Hard Materials, Vol. 1(3), (1985), pp. 147-158."

[140] "Fernandes C. M., Senos A., 'Cemented carbide phase diagrams: A review', Int. Journal of Refractory Metals and Hard Materials, Vol. 29 (2011), pp. 405-418."

[141] "Asl K., Sohi M. H., Hokamoto K., Uemura M., 'Effect of Heat treatment on wear behaviour of HVOF thermally sprayed WC-Co coatings', Wear, Vol. 260, (2006), pp. 1203-1208."

[142] "Bouaouadja N. et al, 'Fracture toughness of WC-Co cemented carbides at room temperature', Journal of Materials Science Letters, Vol. 13 (1994), pp.17-19."

[143] "N. V. NOVIKOV, et al. Inst. of Superhard Mater., Academy of Sci. 55R, Kiev (1982)."

[144] "F. OSTERSTOCK, Th~se de Docteur-ingdnieur, Universite de CAEN, France (1973)."

[145] "Park S. Y., Kim M. C., Park C. G., 'Mechanical Properties and microstructure evolution of the nano WC-Co coatings fabricated by detonation gun spraying with post heat treatment.' Material Science and Engineering A, Vol. 449-451, (2007), pp. 894 – 897."

[146] "Yao Z. G., Stiglich J. J., Surdashan T. S., 'Nano-grained Tungsten Carbide-Cobalt (WC/Co), Working paper. Fairfax: Material Modification, Print."

[147] "Kim H., Shon I., Yoon J., Doh J., 'Consolidation of ultrafine WC and WC−Co hard materials by pulsed current activated sintering and its mechanical properties', International Journal of Refractory Metals and Hard Materials, Vol. 25, (2007), pp. 46−52."

[148] "Su W. et al, 'Effects of TaC on microstructure and mechanical properties of coarsegrained WC-9Co cemented carbides', Transactions of Nonferrous Metals Society of China, Vol. 25 (2015), pp. 1194−1199."

[149] “Zak Fang Z, Wang Xu, Ryu Taegong, Hwang Kyu Sup, Sohn HY. Synthesis, sintering, and mechanical properties of nanocrystalline cemented tungsten carbide–A review. Int J Refract Metals Hard Mater Vol. 27 (2009), pp. 288–99.”

[150] “Saito H., Iwabuchi A., Shimizu T., ‘Effects of Co content and WC grain size on the wear of WC cemented carbide’, Wear Vol. 26 (2006), pp. 126–32.”

[151] “Okamoto S, Nakazono Y, Otsuka K, Shimoitani Y, Takada J., ‘Mechanical properties of WC/Co cemented carbide with larger WC grain size’, Materials Characterisation, Vol. 55 (2005), pp. 281–287.”

[152] “Schmid HG, Mari D, Benoit W, Bonjour C., ‘The mechanical behaviour of cemented carbides at high temperatures’, Mater Sci Eng A Vol. 105-106 (1988) pp. 343–51.”

[153] “Q. Yang, T. Senda, A. Hirose, ‘Sliding wear behaviour of WC–12Co coatings at elevated temperatures’, Surface & Coatings Technology 200 Vol. 14–15 (2006), pp. 4208–4212.”

[154] “Long, J., Zhang, W., Wang, Y., Zhang, J., Lu, B., Cheng, K., Peng, Y., ‘A new type of WC-Co-Ni-Al cemented carbide: grain size and morphology of Y’ strengthened composite binder phase’, Scripta Materialia, Vol. 126, (2017), pp. 33-36.”

[155] “Vashishtha N. et al, ‘Effect of heat treatment on friction and abrasive wear behaviour of WC 12Co and Cr3C2-25NiCr coatings’, Tribology International, Vol. 118 (2018) pp. 381-399.”